

X-Ray Scattering of Biomaterials

X-RAY SCATTERING OF BIOMATERIALS

BY

FEI-CHI YANG, B.Sc.

A THESIS

SUBMITTED TO THE DEPARTMENT OF PHYSICS & ASTRONOMY

AND THE SCHOOL OF GRADUATE STUDIES

OF MCMASTER UNIVERSITY

IN PARTIAL FULFILMENT OF THE REQUIREMENTS

FOR THE DEGREE OF

MASTER OF SCIENCE

© Copyright by Fei-Chi Yang, September 2014

All Rights Reserved

Master of Science (2014)
(Physics & Astronomy)

McMaster University
Hamilton, Ontario, Canada

TITLE: X-Ray Scattering of Biomaterials

AUTHOR: Fei-Chi Yang
B.Sc., (Physics)
National Taiwan University, Taipei, Taiwan

SUPERVISOR: Dr. Maikel C. Rheinstädter

NUMBER OF PAGES: xii, 97

Abstract

Molecular structures of biomaterials have close relation to their functions. We are interested in how biological building blocks assemble into the structures of native biomaterials and the hierarchy of those structures. We tackled the problem mainly with X-ray diffraction experiments and developed a thorough analysis technique to assign the X-ray signals to protein secondary structures and chitin. Three different types of biomaterials were examined: vimentin fibres, squid pens, and human hair. In vimentin fibres, we found that the secondary protein structures play an important role in the strength of the fibres. In native squid pens, we found a self-similar, hierarchical structure from millimetres down to nanometres. In human hair, we compared the signals corresponding to keratin proteins, intermediate filaments, and lipids between different subjects, and found small deviations. The structures of these three biomaterials, which encompass different orders of length scales, were described both quantitatively and graphically. We hope that this work will eventually allow us to understand how and why nature builds biomaterials this way.

Acknowledgements

These two years have been absolutely rewarding for me. It was challenging at first, but I would not have known what I am capable of if I was not challenged. Now I have a better and healthier mentality when it comes to stress and I appreciate all the difficulties because I know they help me grow faster and keep me grounded. Coming to McMaster was one of the best decisions I have made.

I would like to thank my parents, sisters and boyfriend for all the support they have provided me throughout the years. Without them, I would not be able to come so far. A big thank you to my good friends, Christina Dzieduszycki, Nehad Hirmiz, Ashkan Dehghan, Kelly Cathcart, Joey Sham, and Peter Fiee for taking excellent care of me and bearing with me sometimes. Special thanks to Joya Sushi, which has provided me with amazing food, or I would otherwise not be able to make it in Hamilton.

Thank you my lab members, Laura Topozini, Richard Alsop and Hannah Dies, and office members, Mark Ilton, Rafael Schulman, Paul Fowler, Matilda Backholm and Markus Rose for helping me not only with academic discussions, but also for relaxing and casual conversations. It was great to have you in the same room.

I would like to acknowledge all my collaborators including Dr. Robert Peters, Nicole Pinto, Dr. Atsuko Negishi, Dr. Todd Gillis, Dr. Douglas Fudge, Dr. Niels

Smeets, Emilia Bakaic, Francis Yavitt, and Dr. Todd Hoare. They have given me a chance to learn about new fields and different ways to approach problems.

Thank you for the amazing courses taught by the wonderful professors, Dr. Paul Higgs, Dr. Duncan O'Dell, Dr. An-Chang Shi, and Dr. James Britten. I would in particular like to thank my committee members, Dr. Jose Moran-Mirabal and Dr. An-Chang Shi, for giving me valuable comments on my research.

Most importantly, I would like to thank my supervisor Dr. Maikel Rheinstädter for all the things he has taught me. He is extremely dedicated to his students and research. He is always generous with his time, and always willing to help us with any questions we have. He has given us numerous opportunities to attend conferences, conduct experiments in national science facilities, which makes our research known by more people. I will carry his enthusiasm and dedications to wherever I am going.

Contents

Abstract	iii
Acknowledgements	iv
1 Introduction	1
2 Biomaterials	3
2.1 Building Blocks in Biology	4
2.1.1 Proteins	4
2.1.2 The Importance of Protein Structure	9
2.1.3 Chitin	10
2.2 Hierarchical Organization of Biomaterials	11
3 Theoretical Background of X-Ray Diffraction	13
3.1 Why is X-Ray Diffraction a Good Technique to Study Biological Systems	13
3.2 X-Ray Diffraction	14
3.2.1 Unit Cell	14
3.2.2 Reciprocal Space	14
3.2.3 Miller Indices	16

3.2.4	Bragg's Law and Laue Condition	18
3.2.5	Information from Diffracted Intensity	21
3.2.6	Broadening of Bragg Peaks	24
3.2.7	Systematic Absence	25
3.2.8	Forbidden Bragg Peaks	25
3.3	Determination of Secondary Structures by X-Ray Diffraction	27
3.3.1	The Discovery of α -Helix and Coiled-Coils	27
3.3.2	The Diffraction Pattern of β -Sheets	32
3.3.3	α and β -Chitin	32
4	Experimental Background of X-Ray Diffraction	35
4.1	Rigaku SmartLab Diffractometer	35
4.2	Experimental Procedure	39
4.2.1	X-Ray Fibre Diffraction	39
4.3	Building Two-Dimensional Reciprocal Space	42
4.4	Acquiring Information from the Data	43
5	X-Ray Diffraction of Biomaterials	46
5.1	Paper I: Self-assembly Enhances the Strength of Fibres Made from Vimentin Intermediate Filament Proteins	46
5.1.1	Preface to Paper I	46
5.2	Paper II: Hierarchical, Self-Similar Structure in Native Squid Pen	57
5.2.1	Preface to Paper II	57
5.3	Paper III: The Structure of People's Hair	67
5.3.1	Preface to Paper III	67

6	Appendix	81
6.1	Paper IV: Probing the Internal Morphology of Injectable Poly(oligoethylene glycol methacrylate) Hydrogels by Light and Small-Angle Neutron Scattering	81

List of Figures

2.1	Different levels of protein structures are introduced. [This image has been released into the Public domain by LadyofHats, via Wikimedia Commons.]	5
2.2	Amino Acid.	6
2.3	a) parallel and b) antiparallel β -sheet structures.	8
2.4	The repeating unit of chitin.	10
2.5	Illustration of different types of chitin.	11
2.6	Hierarchy of American Lobsters. [Figure From Raabe, D., Sachs, C., & Romano, P. (2005). <i>Acta Materialia</i> , 53(15), 4282.]	12
3.1	The unit cell, the three lattice vectors, and the corresponding angles.	15
3.2	The structures in real space are transformed into reciprocal space by X-ray diffraction. The diffraction pattern can be Fourier transformed back to real space structures.	16
3.3	The lattice vectors \vec{a}_1 , \vec{a}_2 , and \vec{a}_3 are shown in real space. The corresponding reciprocal lattice vectors \vec{a}_1^* , \vec{a}_2^* , and \vec{a}_3^* are shown in reciprocal space.	16
3.4	A set of planes in real space corresponds to one Bragg spot in reciprocal space.	17

3.5	a) shows an array of lattice spacing d_{hkl} , an incoming wave vector \vec{k} , an outgoing wave vector \vec{k}' , and the scattering vector \vec{q}_{hkl} . b) shows the triangle formed by \vec{k} , \vec{k}' and \vec{q}_{hkl}	19
3.6	a) shows the Fourier transform of a basis. b) shows the FT of three narrow slits . c) shows the FT of three bases.	24
3.7	Figure a) shows the 1D diffraction pattern from a single basis. b) from 3 bases. c) from N bases.	24
3.8	Within the domain, atoms have defined arrangement. However, in between the domains, atoms are loosely aligned. [Figure from Förster, S., Timmann, A., Schellbach, C., Frömsdorf, A., Kornowski, A., Weller, H., Roth, S. V., & Lindner, P. (2007). <i>Nature materials</i> , 6(11), 890.] .	26
3.9	X-ray image from Astbury and Woods in 1934. The signatures for the coiled-coils structure are the diffuse 9.8 Å equatorial peak and the 5.15 Å meridian peak. [Figure adapted from Astbury, W. T., & Woods, H. J. (1934). <i>Philosophical Transactions of the Royal Society of London. Series A, Containing Papers of a Mathematical or Physical Character</i> , 393.]	28
3.10	The α -helix proposed by Pauling and Corey with 3.7 residues per turn. [Figure From Pauling, L., Corey, R. B., & Branson, H. R. (1951). <i>Proceedings of the National Academy of Sciences</i> , 37(4), 207.]	29
3.11	Part a) shows that the pitch of the small helix and the pitch of a large helix (coiled-coil). Part b) shows the coiled-coils with different numbers of strands. [Figure From Pauling, L., & Corey, R. B. (1953). <i>Nature</i> 171, 59.]	29

3.12	The illustration and the X-ray pattern of the helix. [Part b) adapted from Sherwood, D. (1976). Crystals, X-rays and proteins, p. 578. Part c) from Franklin, R. E., & Gosling, R. G. (1953). <i>Nature</i> , 171, 740.] .	31
3.13	Two equatorial peaks at 9.7 and 4.6 Å and a meridional peak at 3.3 Å are circled. [Figure adapted from Pinto, N., Yang, F. C., Negishi, A., Rheinstadter, M. C., Gillis, T. E., & Fudge, D. S. (2014). <i>Biomacromolecules</i> , 15(2), 579.]	33
3.14	Diffraction pattern of a) α and b) β -chitin. [Figure from Rinaudo, M. (2006). <i>Progress in polymer science</i> , 31(7), 605.]	34
3.15	Crystal structures of α and β -chitin. [Figure from Rinaudo, M. (2006). <i>Progress in polymer science</i> , 31(7), 606.]	34
4.1	Interior of the Riqaku SmartLab Diffractometer.	36
4.2	The X-ray spectrum is the superposition of the continuous <i>bremsstrahlung</i> spectrum, which is the broad contribution, and the target-specific characteristic spectrum made of sharp peaks K_α and K_β	37
4.3	Illustration of the function of a Soller Collimator.	38
4.4	a) shows forceps drew from the surface of the solution into fibres. b) shows that fibres were taped horizontally on a cardboard. c) shows the setup of the X-ray experiment.	40
4.5	a) shows a complete squid. b) shows the dissected squid and the transparent squid pen in the middle. c) shows the metal apparatus to squeeze a piece of squid pen in between. d) shows the sealed container for storage. e) shows the humidity chamber mounted on BLADE.	41

4.6	a) shows how the hair is cut on the subject. b) shows how hair strands were mounted on the cardboard. c) shows the hair sample on the loading plate. d) shows the setup for X-ray experiments.	42
4.7	a) shows that detector goes from $2\chi=0$ to 30° to run the first scan. b) shows that X-ray source and the detector moves to $2\theta=0^\circ$ to 0.25° to setup for the second scan. c) shows the detector moves from $2\chi=0^\circ$ to 30° again to finish the second scan. Below is the corresponding diagram for the 2-dimensional reciprocal space data.	43
4.8	a) shows the area integrated for the $q_z/q_{ }$ vs intensity plot. b) shows q_z vs intensity plot. c) shows $q_{ }$ vs intensity plot.	44

Chapter 1

Introduction

As pointed out by Professor Rik Huikes in 2000, 'If bone is the answer, what is the question?' (1) Numerous efforts have been made to understand the structures, functions, and applications of biomaterials. It is not quite clear at this point that what the ultimate conditions for animals to adapt to and what the constraints in the development are, but hopefully all the research in the field will one day add up to answer those big questions.

The early pursuit of the structures of natural biomaterials in the X-ray diffraction field can trace back to Astbury and Woods in the 1930s. They examined numerous materials seen in daily life and tried to understand the fundamentals of molecular bonding. 1951-1953 was the prime time, where many of the seminal breakthroughs took place including the establishment of the models of protein secondary structures, such as α -helices and β -sheets by Pauling and Corey, and the structures of DNA by Watson, Crick and Franklin.

X-ray diffraction is a relatively old but well-established technique to study the structures of materials. Our experimental setup and the procedure are very simple

because our goal is to examine the structures of biomaterials in their native states. In this thesis, we investigated three different materials: vimentin fibre, squid pen and human hair. These materials do not seem to have much in common, but they surprisingly turned out to be all under the theme of protein secondary structures. Vimentin fibres have α -helical and β -sheet protein structures; the amount of β -sheet and the alignment of both structures governs the strength of the fibres. Squid pens also have α -helical protein structures, but with the presence of β -chitin, nano-fibrils made of proteins wrapping around chitin crystallites are formed. As for hair, α -helical keratins bundle into higher level structures such as intermediate filaments and microfibrils. Nature has made protein structures versatile to construct materials for various purposes.

We will introduce the background of biomaterials in Chapter 2. Theoretical and experimental X-ray diffraction will be discussed in detail in Chapter 3 and 4. We will analyse the diffraction pattern, quantify the dimensions of the structures, and comment on our findings in Chapter 5.

Chapter 2

Biomaterials

It is intriguing to observe how nature uses limited numbers of biological building blocks to come up with unlimited types of biomaterials with different properties. As proposed by Arzt (2) and modified by Meyers (3), there are five aspects essential to the design of biomaterials: (a) Multifunctionality: A single type of biomaterials is usually capable of achieving multiple functions. For example, the slime of hagfish can not only make the hagfish slippery and hard to catch, but also suffocate the marine predators by clogging their gills (4). (b) Synthesis: The condition of the synthesis of biomaterials is $T \sim 300$ K and ~ 1 atm, which is opposite to the condition of the man-made materials that tend to be under high pressure or high temperature. (c) Self-Assembly: At first glimpse, the evolution towards self-assembly and the organization of material seems to violate the second law of thermodynamics because the system would go to the direction that maximizes the entropy. However, the condition of the second law of thermodynamics is for an isolated system, but neither earth nor organisms are isolated systems. An open system can exchange energy and matter with its environment, so self-assembly does not contradict with the second law of thermodynamics. (d)

Evolution: Biomaterials have to adapt themselves accordingly to the dynamics of weather, humidity and predators throughout a million-year time span. (e) Hierarchy of structures: biomaterials are often found to have self-similar structures on all the length scales from millimetre down to nanometre.

2.1 Building Blocks in Biology

2.1.1 Proteins

As an important biomacromolecules for living organisms, proteins are in charge of various functions, such as forming protein channels that allow ions to cross the cellular membrane, acting as enzymes that catalyse the chemical reactions, operating as hormones that adjust physiological activities and antibodies that target germs for white blood cells to kill (5). Figure 2.1 shows all the protein structure levels we will discuss in the following sections.

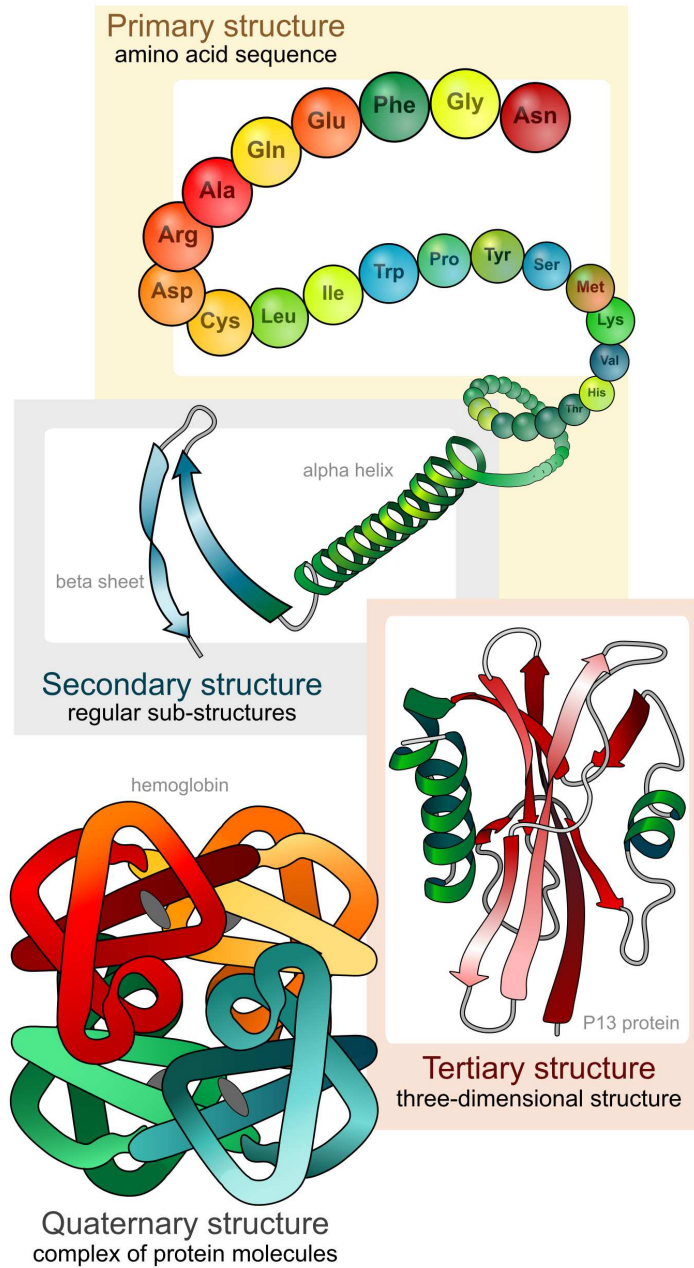


Figure 2.1: Different levels of protein structures are introduced. [This image has been released into the Public domain by LadyofHats, via Wikimedia Commons.]

Amino Acids

The basic units of proteins are amino acids. Starting from the left and following the clockwise direction, the central carbon (α -carbon) is bound to an amine group ($-\text{NH}_2$), a hydrogen, a carboxyl group ($-\text{COOH}$), and a side chain called the R-group as shown in figure 2.2.

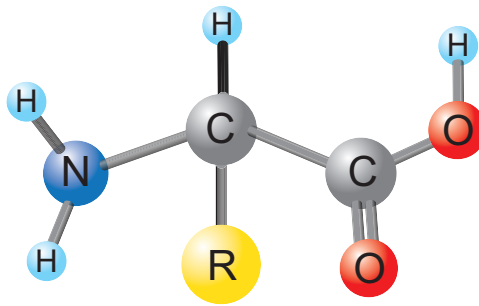


Figure 2.2: Amino Acid.

There are 20 different types of amino acids categorized by the unique R-groups. The R-group defines the properties of proteins and could be nonpolar (hydrophobic), uncharged polar (hydrophilic), acidic (negatively charged; hydrophilic), basic (positively charged; hydrophilic) (6).

Peptide Chains

Amino acids can form into peptide chains by combining the carboxyl group of the first amino acid and the amine group of the second amino acid. The condensation reaction happens such that a water (H_2O) is lost, and ($\text{C}=\text{O}$) and ($\text{N}-\text{H}$) form peptide bonds.

Note that the peptide bond is planar. The C-terminus or the N-terminus refers to the end that has the carboxyl or the amino group. By convention, the head-to-tail direction goes from the N-terminus to C-terminus. If there are less than 30 amino acids in the chains, it is called a peptide; otherwise, it is called a polypeptide.

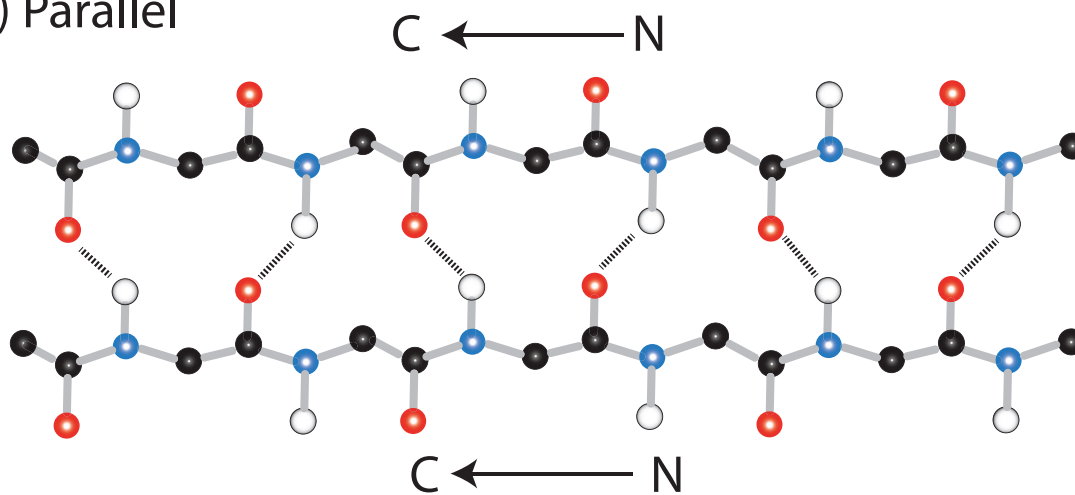
Primary Structures

Primary structures are defined by the linear amino acid sequences of the (poly)peptide which is coded in genes. The primary structure does not directly related to the function of proteins, but it affects the higher levels of structures, which eventually determine the 3-dimensional structure of protein, therefore the function (7).

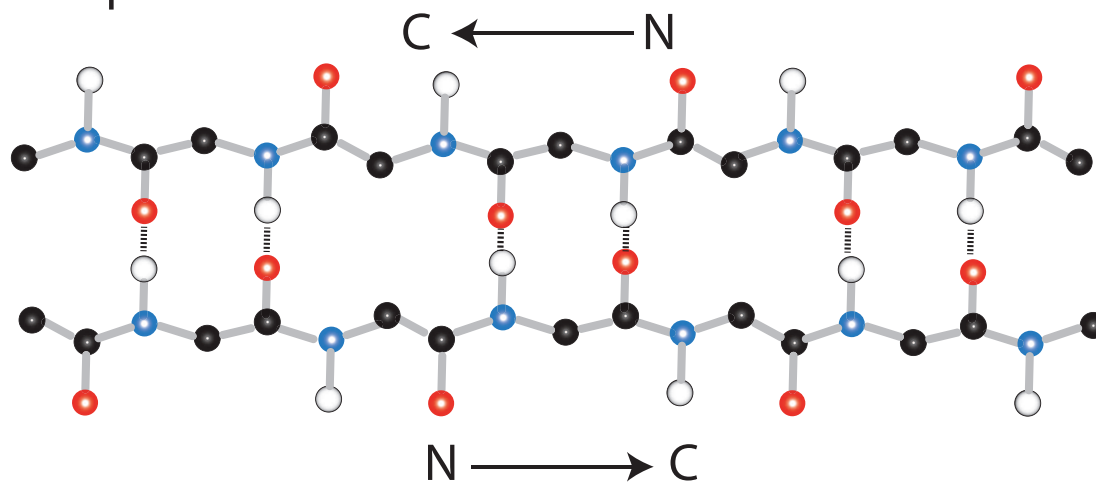
Secondary Structures

The secondary structures of proteins were solved by Pauling, Corey and Branson in 1951 (8; 9). They were the first to deduce the possible configurations of polypeptide chains based on the constraints such as inter-atomic distance and bond angles. They realized that polypeptide chains can form into secondary structures such as α -helices and β -sheets by forming hydrogen bonds between the carbonyl C=O group and the amide N-H group (8). An α -helix is right-handed and usually has 3.6 residues per turn. Each residue is translated 1.5 Å along the long helix axis, which makes the pitch of the α -helix 5.4 Å (3.6×1.5). A β -sheet has two configurations: parallel and anti-parallel as shown in figure 2.3. In the parallel β -sheet, the polypeptide chains run in the same direction from N-terminus to C-terminus whereas in the anti-parallel form, the N-terminus of one chain will be alternating with the C-terminus of the next chain. The repeating distance along the chain direction is 3.3 Å.

a) Parallel



b) Antiparallel



● Carbon ● Oxygen ● Nitrogen ○ Hydrogen

Figure 2.3: a) parallel and b) antiparallel β -sheet structures.

Tertiary Structures

Tertiary structures refer to the three dimensional spatial arrangement of the sequence of amino acids. Most often, α -helices and β -sheets linked by polypeptide segments can be seen within the tertiary structures. The shape greatly depends on the interactions between side chains. The types of side-chain interactions include hydrogen bonds, disulphide bonds, ionic bonds, and hydrophobic interactions.

Quaternary Structures

If a protein consists of more than one amino acid chain, it is regarded as quaternary structures. One famous example of quaternary structures is hemoglobin, which has four polypeptide chains.

2.1.2 The Importance of Protein Structure

Protein structures play an important role for their functions. Proteins have to fold into specific shapes, or to stay folded to function properly. Both stable and non-toxic α -helices and β -sheets can be found in healthy proteins. However, if a certain part of the protein, which is designated to be an α -helix, transforms into a β -sheet, it could expose the hydrophobic amino acids to the water environment and make it insoluble. The insoluble misfolded protein tend to aggregate because these hydrophobic segments on the outside would like to stay close to each other to shield the protein from the water (10; 11).

Protein misfolding can lead to fatal diseases. Taking prion proteins for example, it is known to be related to Creutzfeldt-Jakob disease, scrapie, and bovine spongiform encephalopathy (mad cow disease). The normal prion protein (PrP^c) has $\sim 40\%$

of α -helices and $\sim 3\%$ of β -sheets, but the misfolded scrapie prion protein (PrP^{sc}) has $\sim 30\%$ of α -helices and as high as $\sim 45\%$ of β -sheets (12). Alzheimer disease is another example, the abnormal aggregation of the β -amyloid protein ($A\beta$) in the amyloid plaques has been reported to be the onset of the disease. Therefore, it is of great interest to study the conformations of the protein to possibly help us better understand the cause of diseases.

2.1.3 Chitin

Chitin is widespread in the exoskeleton of insects and crustaceans, shells or beaks in the Mollusca phylum, or cell walls of the fungi and yeast. The basic units of chitin is β -(1-4)-acetamido-2-deoxy-D-glucose as shown in figure 2.4. Based on the crystal structures, chitin has three different formations: α , β , and γ . α -chitin has its chains arranged in the anti-parallel fashion, whereas β -chitin is in the parallel configuration, and γ -chitin has a repeating unit of the neighbouring chains in an anti-parallel way in groups of three, as illustrated in figure 2.5.

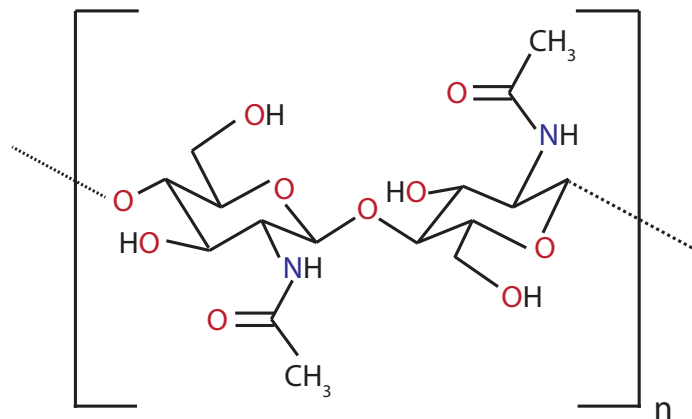


Figure 2.4: The repeating unit of chitin.

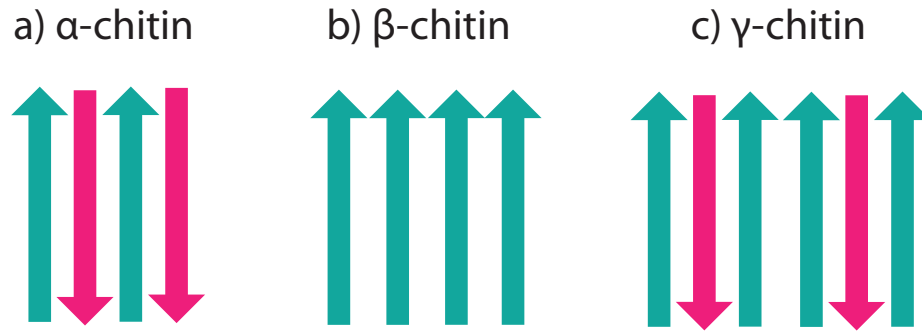


Figure 2.5: Illustration of different types of chitin.

2.2 Hierarchical Organization of Biomaterials

How does nature use limited numbers of building blocks, such as keratin proteins and chitin, but come up with all kinds of biomaterials with different properties? The key lies in the way nature assembles their building blocks, in other words, hierarchical structures. Notice that the biomaterials and the whole organism grow at the same time, and this may be the reason why nature prefers the bottom-up approach. Every molecule is used and is a part of a bigger frame. This intricate way of assembling structures on multiple levels at the same time is worth investigating.

Examples of hierarchical structures in natural materials can be found in numerous materials such as human bones (13) and hair, horns of bighorn sheep (14), claws of lobsters (15), gecko feet (16), etc. These hierarchical structures are shown to be adapting to their specific functions.

Hierarchical structures of American lobsters *Homarus americanus* have been well studied by Raabe *et al* (15; 17). The cuticle of American lobsters has three distinguishable layers: epicuticle, exocuticle, and endocuticle, as shown in figure 2.6. Epicuticle controls the diffusion to the environment while exocuticle and endocuticle are responsible for the strength and hardness. Both the epicuticle and endocuticle are

made of a twisted plywood structure (also named as Bouligand structure) in which each plywood-like plane rotates around the axis normal to the plane. These plywood-like planes are comprised of 50-300 nm diameter fibres, and these fibres are formed by 2-5 nm wide, and 300 nm long nanofibrils made of α -chitin crystallites wrapped by proteins. The advantage of twisted plywood structures is that its constant rotating angle would allow the stress to spread out isotropically and also make the stiffness of the in-plane direction higher than the normal direction (18).

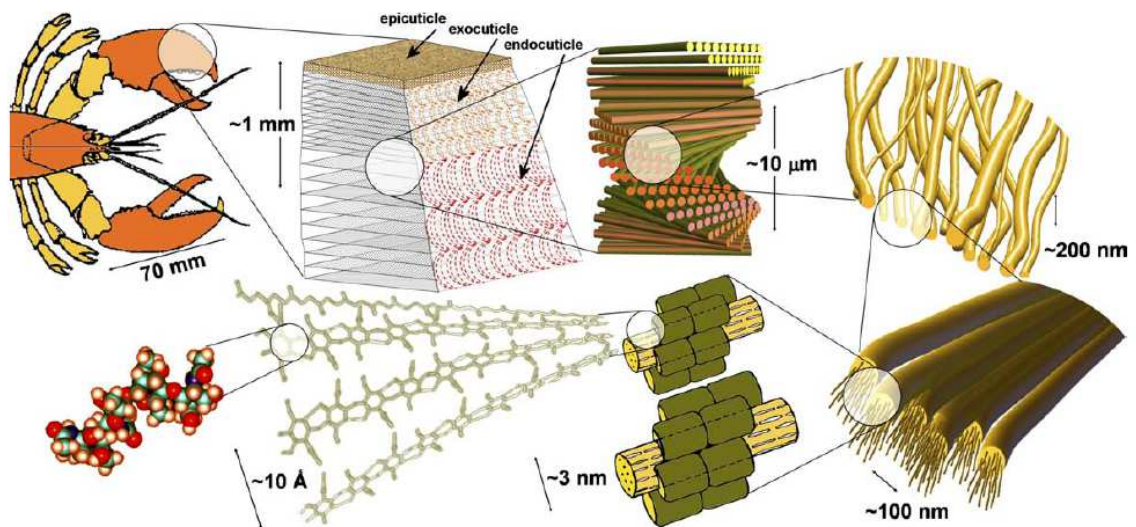


Figure 2.6: Hierarchy of American Lobsters. [Figure From Raabe, D., Sachs, C., & Romano, P. (2005). *Acta Materialia*, 53(15), 4282.]

Chapter 3

Theoretical Background of X-Ray Diffraction

3.1 Why is X-Ray Diffraction a Good Technique to Study Biological Systems

Since discovered in 1895 by Röntgen, X-ray diffraction has been a powerful technique to determine the structures of materials. X-rays are great at probing the molecular structures because their wavelength is comparable to the typical inter-molecule distances. X-rays interact with the electrons of a material, therefore materials with different electron distributions will have different interactions with X-rays. By recording the diffracted intensity at various angles, the structure of a material can be determined.

3.2 X-Ray Diffraction

3.2.1 Unit Cell

A material can have thousands of millions of molecules at different positions. However, if they have translational symmetry, we can easily break down the crystal structures to the smallest repeating unit - the unit cell. Then we just need to specify what molecules are in the unit cell and apply the translational operation to construct the whole material.

Any lattice point on the unit cell can be described as a linear combination of the three lattice vectors, \vec{a}_1 , \vec{a}_2 , and \vec{a}_3 , which span the unit cell as seen in figure 3.1:

$$\vec{R} = n_1\vec{a}_1 + n_2\vec{a}_2 + n_3\vec{a}_3, \quad (3.1)$$

where n_1 , n_2 , n_3 are integers.

The conventional way to select a unit cell is to choose the set of basis that has the smallest volume containing the minimum number of lattice points and the angles closest to the right angle. As long as we know what is comprised of the unit cell and the symmetries the crystals have, we would be able to know the crystal structures.

3.2.2 Reciprocal Space

We have talked about defining the unit cell in real space, but what would happen after X-rays interacting with the real-space structures? X-ray diffraction naturally works in Fourier space and is represented by the diffraction pattern in reciprocal space. Reciprocal space is the momentum space spanned by wave vectors. As shown

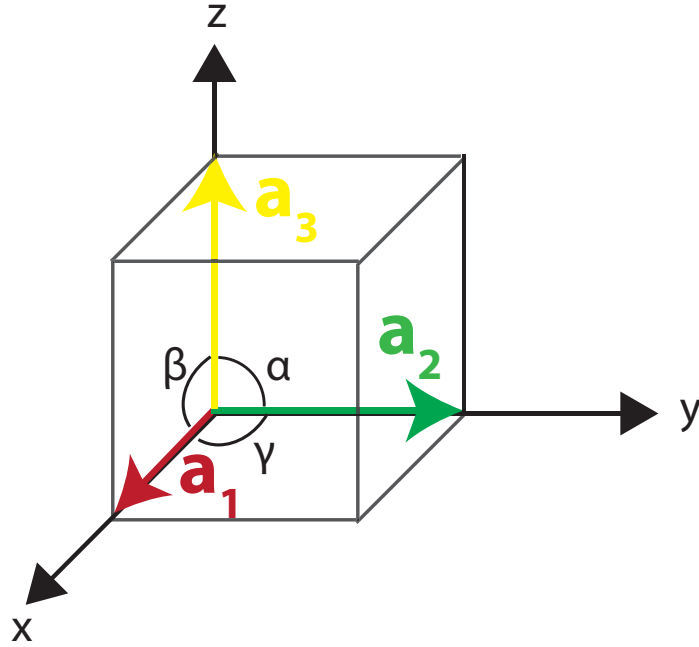


Figure 3.1: The unit cell, the three lattice vectors, and the corresponding angles.

in figure 3.2, by transforming the diffraction pattern back to the real space, we will be able to determine the real space distances, and further determine the structures.

Reciprocal lattice basis vectors \vec{a}_1^* , \vec{a}_2^* , \vec{a}_3^* can be built by the following equations, as illustrated by figure 3.3:

$$\begin{aligned}\vec{a}_1^* &= \frac{2\pi}{v}(\vec{a}_2 \times \vec{a}_3), \\ \vec{a}_2^* &= \frac{2\pi}{v}(\vec{a}_3 \times \vec{a}_1), \\ \vec{a}_3^* &= \frac{2\pi}{v}(\vec{a}_1 \times \vec{a}_2),\end{aligned}\tag{3.2}$$

where v is the volume of the unit cell.

Which will satisfy:

$$\vec{a}_i \cdot \vec{a}_j^* = 2\pi\delta_{ij}.\tag{3.3}$$

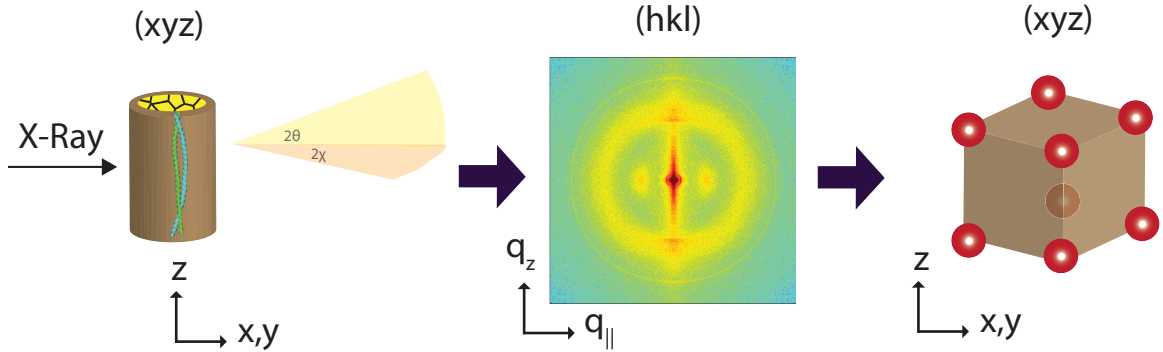


Figure 3.2: The structures in real space are transformed into reciprocal space by X-ray diffraction. The diffraction pattern can be Fourier transformed back to real space structures.

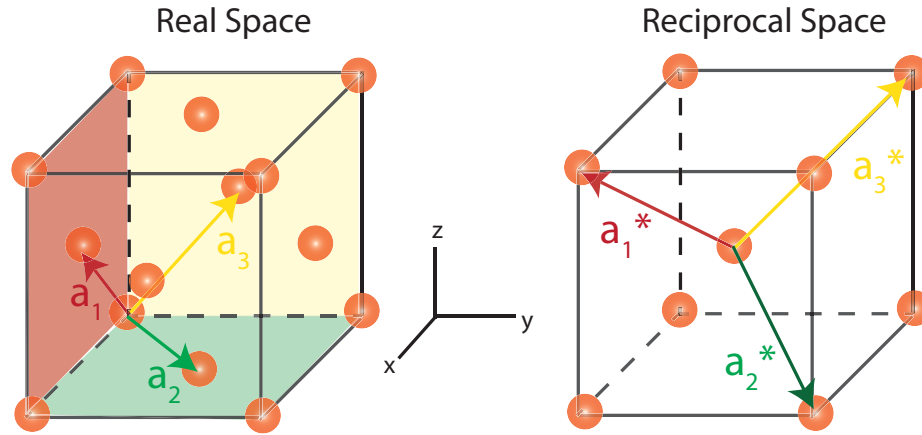


Figure 3.3: The lattice vectors \vec{a}_1 , \vec{a}_2 , and \vec{a}_3 are shown in real space. The corresponding reciprocal lattice vectors \vec{a}_1^* , \vec{a}_2^* , and \vec{a}_3^* are shown in reciprocal space.

3.2.3 Miller Indices

Miller indices (hkl) are the indices we use to label the points in reciprocal space or equivalently, the set of planes in real space. Miller indices (hkl) intercept the vector $(\vec{a}_1, \vec{a}_2, \vec{a}_3)$ at $(\frac{\vec{a}_1}{h}, \frac{\vec{a}_2}{k}, \frac{\vec{a}_3}{l})$. As shown in figure 3.4, the plane (200) in real space intercepts at $(\frac{\vec{a}_1}{2}, \infty, \infty)$ and the plane (321) intercepts at $(\frac{\vec{a}_1}{3}, \frac{\vec{a}_2}{2}, \vec{a}_3)$. In reciprocal space, (200)

and (321) correspond to two distinct Bragg peaks. Therefore, when the diffraction pattern is acquired, by comparing the location of Bragg peaks, the symmetry of the system can be determined.

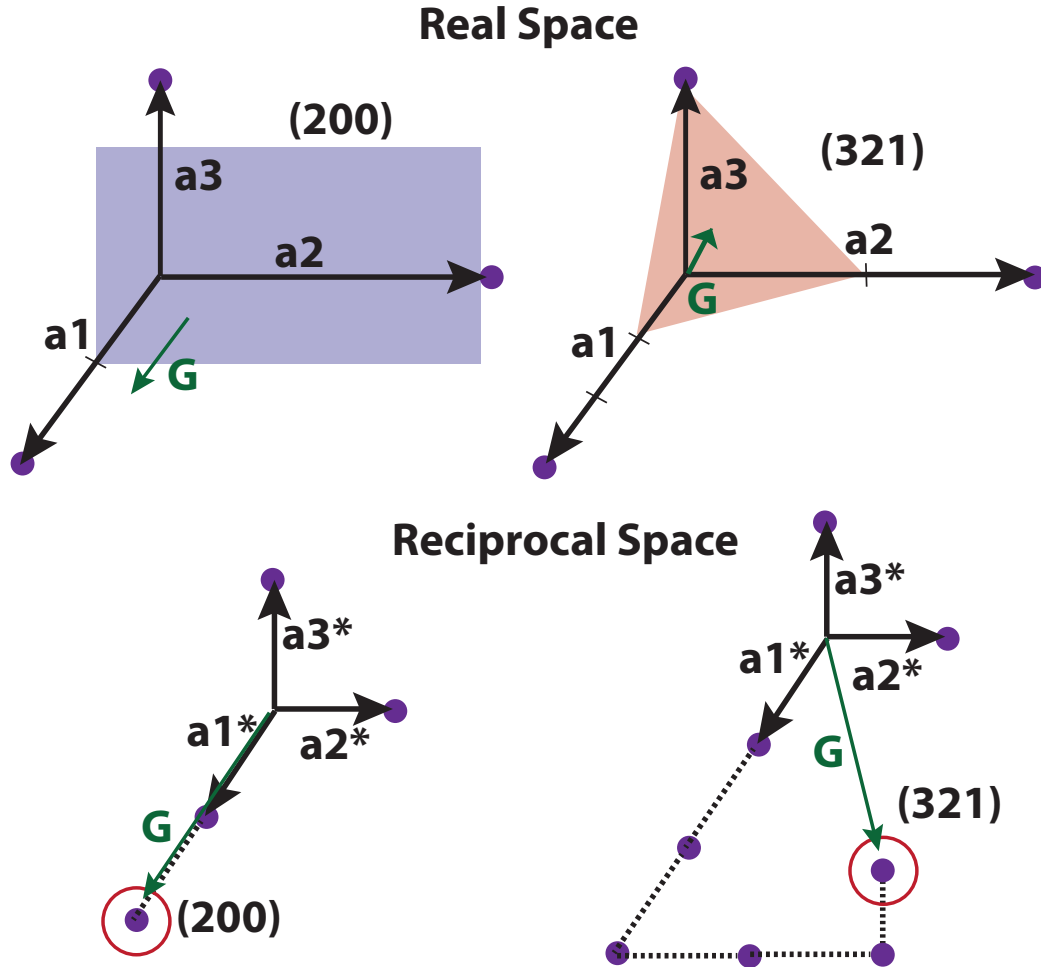


Figure 3.4: A set of planes in real space corresponds to one Bragg spot in reciprocal space.

Act as the counterpart of real space lattice vectors, the reciprocal space vectors tells us where a point in reciprocal lattice is, and is defined as

$$\vec{G} = h\vec{a}_1^* + k\vec{a}_2^* + l\vec{a}_3^*, \tag{3.4}$$

Therefore,

$$\vec{G} \cdot \vec{R} = 2\pi(hn_1 + kn_2 + ln_3), \quad (3.5)$$

will be integers of π .

3.2.4 Bragg's Law and Laue Condition

When X-rays are shined on a material, the incoming waves will diffract off different planes of the material. To have a non-vanishing intensity, the diffracted waves from all the planes with the same Miller indices need to have a specific angle θ and spacing d between parallel planes, so that all the diffracted waves will be in phase and add up. Bragg's law tells us the condition of constructive interference:

$$2d\sin\theta = n\lambda, \quad (3.6)$$

where λ is the wavelength of the incoming source, and n could be any integers determined by the order.

The scattering vector \vec{q}_{hkl} is a vector that characterizes the momentum transfer in the scattering process. To deduce the relationship between the scattering vector \vec{q}_{hkl} and the real space distance d_{hkl} , consider an incoming wave vector \vec{k} , an outgoing wave vector \vec{k}' and the distance d_{hkl} corresponding to the spacing of the planes (hkl). Since we only consider elastic scattering at this point, the magnitude of \vec{k} and \vec{k}' would be equal:

$$|\vec{k}| = |\vec{k}'| = \frac{2\pi}{\lambda}. \quad (3.7)$$

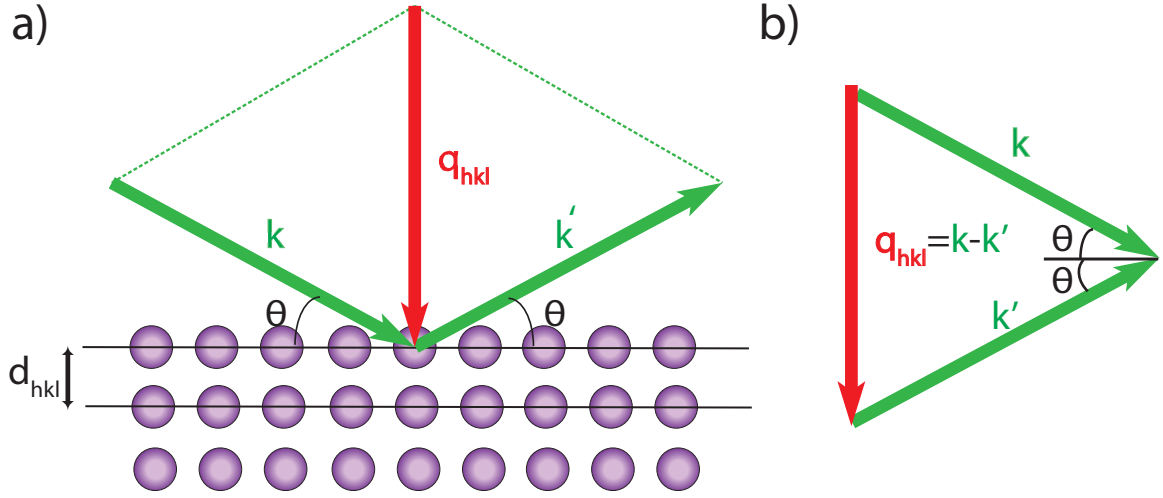


Figure 3.5: a) shows an array of lattice spacing d_{hkl} , an incoming wave vector \vec{k} , an outgoing wave vector \vec{k}' , and the scattering vector \vec{q}_{hkl} . b) shows the triangle formed by \vec{k} , \vec{k}' and \vec{q}_{hkl} .

Looking at the triangle formed by \vec{k} , \vec{k}' , and \vec{q}_{hkl} in figure 3.5, we acquire:

$$\vec{q}_{hkl} = \vec{k} - \vec{k}'. \quad (3.8)$$

The length of the scattering vector \vec{q}_{hkl} corresponding to the same set of planes (hkl) is equal to twice the length of $|\vec{k}| \sin\theta$ by

$$|\vec{q}_{hkl}| = 2 |\vec{k}| \sin\theta = \frac{4\pi \sin\theta}{\lambda}. \quad (3.9)$$

By rearranging Bragg's Law we obtain:

$$\frac{1}{\lambda} = \frac{1}{2d_{hkl} \sin\theta}. \quad (3.10)$$

Plugging $\frac{1}{\lambda}$ into equation 3.9, one obtains:

$$|\vec{q}_{hkl}| = \frac{2\pi}{d_{hkl}}. \quad (3.11)$$

The Laue conditions are equivalent to the Bragg's Law. The Laue conditions require:

$$\begin{aligned} \vec{a}_1 \cdot \vec{q}_{hkl} &= 2\pi h, \\ \vec{a}_2 \cdot \vec{q}_{hkl} &= 2\pi k, \\ \vec{a}_3 \cdot \vec{q}_{hkl} &= 2\pi l. \end{aligned} \quad (3.12)$$

The inner product of \vec{G} and the sum of lattice vectors $\vec{a}_1, \vec{a}_2, \vec{a}_3$ will be:

$$\vec{G} \cdot (\vec{a}_1 + \vec{a}_2 + \vec{a}_3) = 2\pi \cdot (h + k + l). \quad (3.13)$$

The Laue conditions will lead to:

$$\vec{q}_{hkl} \cdot (\vec{a}_1 + \vec{a}_2 + \vec{a}_3) = 2\pi \cdot (h + k + l). \quad (3.14)$$

Therefore, the reciprocal lattice vector has to equal to the scattering vector to produce a constructive interference:

$$\vec{G} = \vec{q}_{hkl}. \quad (3.15)$$

3.2.5 Information from Diffracted Intensity

Intensity of the diffraction pattern is proportional to the product of scattering amplitude $F(q)$ and its complex conjugate $F^*(q)$:

$$I(q) = F(q) \cdot F^*(q). \quad (3.16)$$

Scattering amplitude is contributed by three components: one is from an atom itself, another is from all the atoms in the unit cell, the other is from the lattice structure. In the language of X-ray crystallography, they are called the atomic form factor, the form factor and the structure factor.

Atomic Form Factor

Atomic form factor, or the atomic scattering amplitude, tells us how strongly an atom scatters. Since X-rays are interacting with the electrons, the more electrons an atom has, the stronger it scatters. Atomic form factor of an atom is defined by:

$$f(\vec{q}) = \int \rho_j(\vec{r}) e^{i\vec{q}\cdot\vec{r}} d\vec{r}, \quad (3.17)$$

with \vec{q} the scattering vector, \vec{r} the vector that specifies the positions of an electron with respect to the center of mass of the atom, and $\rho(\vec{r})$ the electron density function of the atom.

What worth noting is that atomic form factor is the Fourier transform of the electron density function. When q approaches 0, the atomic form factor will be approaching Z , which is the total number of electrons in the atom.

Break Down the Scattering Amplitude into Form Factor and Structure Factor

The most general form for the scattering amplitude of a crystal can be expressed as:

$$F(\vec{q}) = \sum_l^{\text{All atoms}} f_l(\vec{q}) e^{i\vec{q}\cdot\vec{r}_l}, \quad (3.18)$$

where f_l is the atomic form factor of the atom l^{th} , \vec{q} is the scattering vector, and \vec{r}_l is the position of the l^{th} atom.

However, we can exploit the properties of a crystal, and define the position of an atom in the crystal (\vec{r}_l) as the addition of the lattice vector (\vec{R}_n) and the position of an atom with respect to the unit cell (\vec{r}_j):

$$\vec{r}_l = \vec{R}_n + \vec{r}_j. \quad (3.19)$$

Plugging equation 3.19 into equation 3.18, one obtains:

$$\begin{aligned} F(\vec{q}) &= \sum_{\vec{R}_n + \vec{r}_j}^{\text{All atoms}} f_j(\vec{q}) e^{i\vec{q}\cdot(\vec{R}_n + \vec{r}_j)} \\ &= \sum_n e^{i\vec{q}\cdot\vec{R}_n} \sum_j f_j(\vec{q}) e^{i\vec{q}\cdot\vec{r}_j}. \end{aligned} \quad (3.20)$$

The first summation is called the structure factor, which is related to the symmetry of unit cells:

$$S(\vec{q}) = \sum_n e^{i\vec{q}\cdot\vec{R}_n}. \quad (3.21)$$

The second summation is the form factor, which indicates the scattering amplitude

of all the atoms in the unit cell:

$$F^{form}(\vec{q}) = \sum_j f_j(\vec{q}) e^{i\vec{q}\cdot\vec{r}_j}. \quad (3.22)$$

Therefore, the scattering amplitude of a crystal is defined as the convolution of the structure factor and the form factor, which will be discussed in the next section.

Convolution Theorem

The convolution theorem tells us that the Fourier transform (FT) of the convolution of two functions equals to the product of the separate Fourier transform of each function. In real space, a crystal is considered as the convolution of the lattice and the basis. Therefore in reciprocal space, the scattering amplitude, which is the Fourier transform of the convolution of a crystal, would equal to the product of the Fourier transform of a lattice and a basis, namely, the product of structure factor and form factor.

We can simulate a basis using one wide slit and lattice using three narrow slits. Figure 3.6 shows an example of the FT of one wide slit and three narrow slits simulated as three delta functions. The third figure shows the FT of three wide slits in reciprocal space is the multiplication of the FT of one wide slit and the FT of three narrow slits.

Information from Form Factor and Structure Factor

Figure 3.7 shows the simulated diffraction intensity from different numbers of bases. As number of bases increases, the relative intensity of the diffraction pattern stays unaltered. This suggests that the intensity of the Bragg peaks is defined by the form

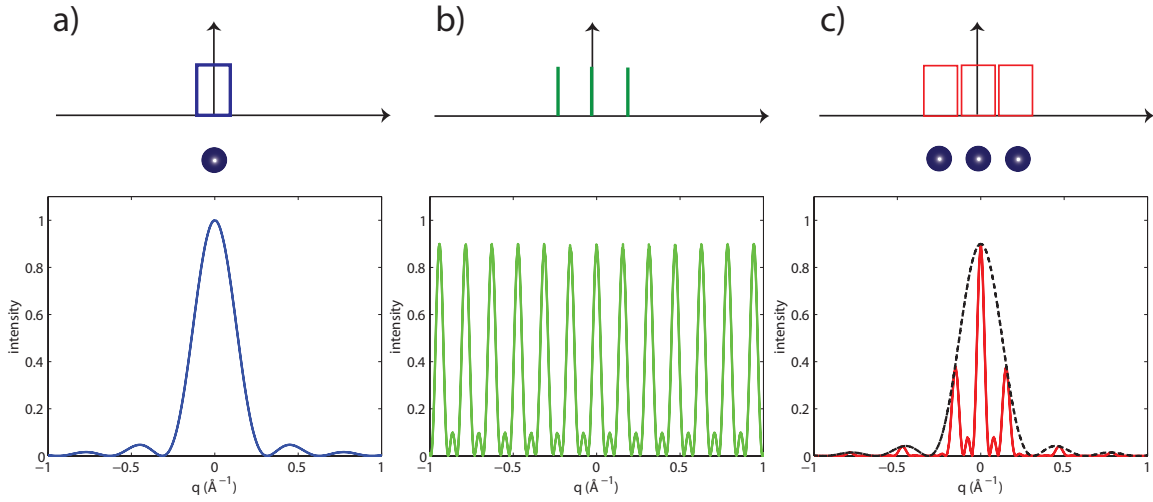


Figure 3.6: a) shows the Fourier transform of a basis. b) shows the FT of three narrow slits. c) shows the FT of three bases.

factor where the positions of the peaks depend on the structure factor.

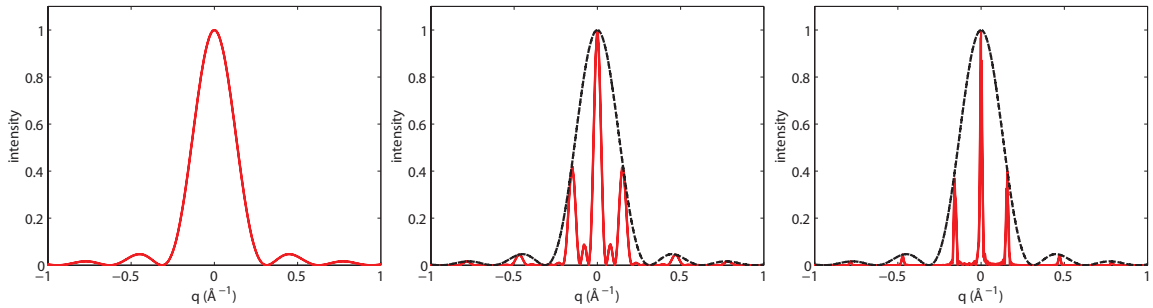


Figure 3.7: Figure a) shows the 1D diffraction pattern from a single basis. b) from 3 bases. c) from N bases.

3.2.6 Broadening of Bragg Peaks

In an ideal world where reflecting planes are perfectly lined up, and the source is monochromatic and well-aligned, all the peaks should appear sharply. However, there are several reasons that can result in the broadening of Bragg peaks. The causes can be categorized into the contributions from instruments or from samples. Instrumental

contributions include that the X-rays have a band of wavelength instead of a single wavelength, the X-ray beam from the source is divergent, or the path of X-rays is misaligned. The sample's contribution includes the effect of a finite crystallite size, inhomogeneous strain and crystal imperfections. The effect of the crystallite size is characterized by the *Scherrer* equation:

$$L = \frac{K\lambda}{B\cos\theta}, \quad (3.23)$$

where L is crystallite size, λ is wavelength, B is the full width at half maximum (FWHM) of the diffraction peaks in radians, and θ is the Bragg angle.

3.2.7 Systematic Absence

Based on the the symmetry a crystal has, there can be systematic absences in the diffraction pattern. Imagine that if a crystal has a special symmetry that the one row of the molecules along the c-axis is shifted to the next row of the molecules by $\frac{c}{2}$ translation. Now the repeating distance of the molecules becomes half of $|\vec{c}|$, which in reciprocal space, the distance would be double the $|\vec{c}^*|$ distance. Therefore, the Bragg peaks appear at $2n \cdot |\vec{c}^*|$ (n is any integer) positions. Equivalently, the diffraction pattern looks like it is missing a systematic of peaks at $(2n+1) \cdot |\vec{c}^*|$.

3.2.8 Forbidden Bragg Peaks

Opposite to what we know, it has been reported by Förster *et al* that it is possible to have Bragg peaks show up at systematic absences' positions in soft materials (19). The origins of the forbidden Bragg peaks are due to the boundaries where different

domains meet, as shown in figure 3.8. Within the domains, atoms have defined orientations, but in between the domains, there are atoms not aligning with other domains, which would shift the phases of the originally perfectly cancelled waves, and result in some intensities at forbidden positions.

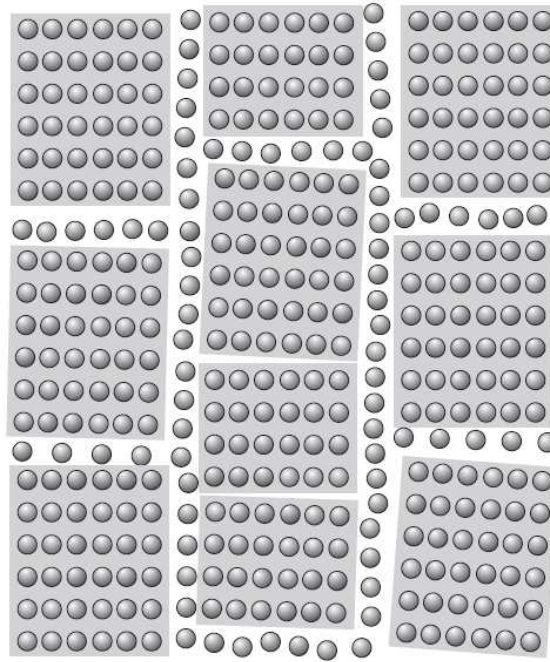


Figure 3.8: Within the domain, atoms have defined arrangement. However, in between the domains, atoms are loosely aligned. [Figure from Förster, S., Timmann, A., Schellbach, C., Frömsdorf, A., Kornowski, A., Weller, H., Roth, S. V., & Lindner, P. (2007). *Nature materials*, 6(11), 890.]

3.3 Determination of Secondary Structures by X-Ray Diffraction

3.3.1 The Discovery of α -Helix and Coiled-Coils

The structure of α -keratin had puzzled the scientist in the field for more than thirty years. The X-ray diffraction pattern of α -keratin was discovered first by Herzog and Jancke (20). In the 1930s, Astbury investigated the structures of a series of natural material such as hair, wool, silk, and muscles, etc. The X-ray photograph from their paper is shown in figure 3.9 (21). The distinct pattern shows a strong peak at 5.15 \AA at the meridian and also an equatorial peak around 10 \AA .

At that time, Pauling and Corey were trying to dig out all the possible structures of a single polypeptide chain that could be formed by hydrogen bonds (8). Considering the inter-atomic distances, bond angles, and other chemistry constraints, they proposed the α -helix model shown in figure 3.10, which has all the hydrogen bonds parallel to the long helix axis. The α -helix they proposed has 3.7 residues per turn, and the rise per residue is 1.47 \AA which makes the pitch $3.7 \times 1.47 = 5.4 \text{ \AA}$. The existence of the 1.5 \AA peak in hair and porcupine quill was later proved by Perutz (22).

In the following paper of Pauling and Corey, they used their α -helix model to calculate the structure factor for α -keratin and crystalline muscles (23). For the α -keratin structure, the calculated equatorial equation (100) assuming hexagonal packing and lattice vector $|\vec{a}| = 11 \text{ \AA}$ was at 9.5 \AA . For crystalline muscle with a triclinic dimension hypothesized, the calculated and observed intensity in the equatorial direction was in good agreement.

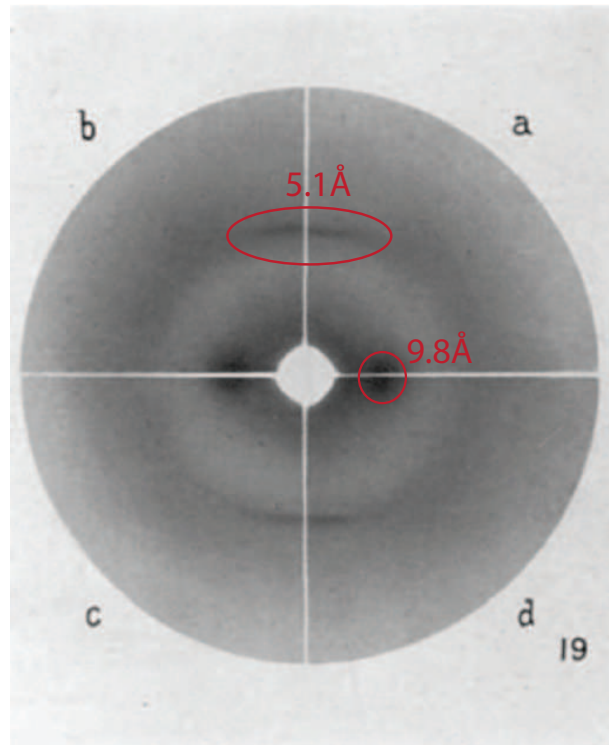


Figure 3.9: X-ray image from Astbury and Woods in 1934. The signatures for the coiled-coils structure are the diffuse 9.8 Å equatorial peak and the 5.15 Å meridian peak. [Figure adapted from Astbury, W. T., & Woods, H. J. (1934). *Philosophical Transactions of the Royal Society of London. Series A, Containing Papers of a Mathematical or Physical Character*, 393.]

The equatorial peak can approximately be explained by the α -helix structures, but what about the 5.1 Å meridian reflection? Crick and Pauling individually came to the conclusion that α -helices alone was not the whole story for α -keratin at the end of 1952 (24; 25). α -helices bundle into coiled-coils as illustrated in figure 3.11. Crick solved the mathematical function of Fourier transform of two-strand coiled-coils. He found that his coiled-coil model successfully described both the 5.1 and 1.5 Å meridional peak, and also the near 10 Å equatorial reflection. The nature of the 1.5 Å is the repeating distance on the polypeptide chain where 5.1 Å is the

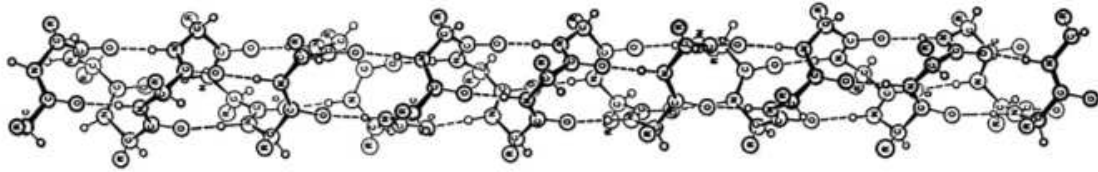


Figure 3.10: The α -helix proposed by Pauling and Corey with 3.7 residues per turn. [Figure From Pauling, L., Corey, R. B., & Branson, H. R. (1951). *Proceedings of the National Academy of Sciences*, 37(4), 207.]

repeating distance of the arrangement of the side-chains (25). Nowadays, coiled-coil structures have been widely known existing in various types of proteins that form higher levels of structures such as intermediate filaments.

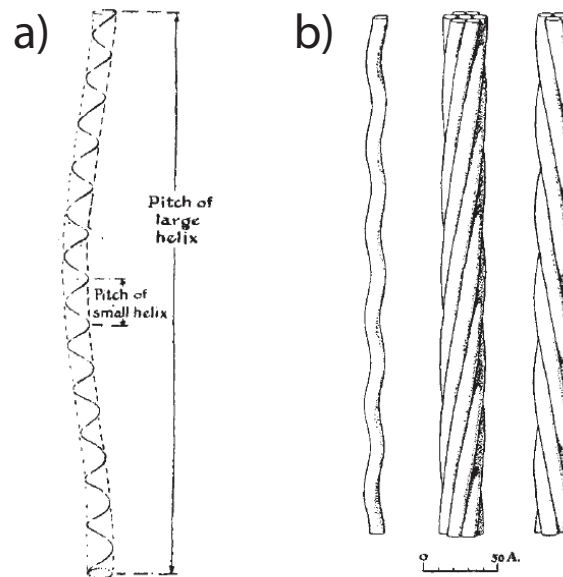
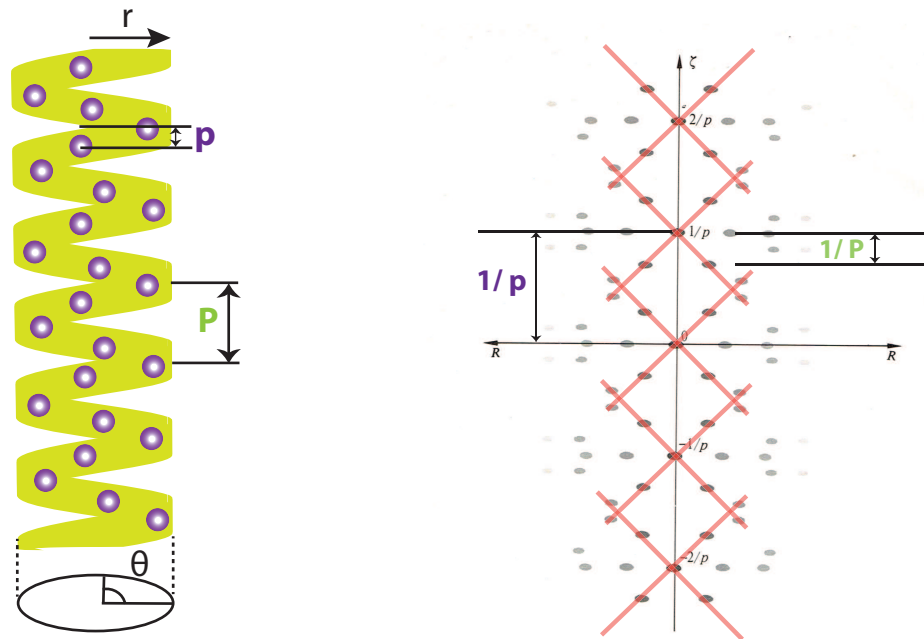


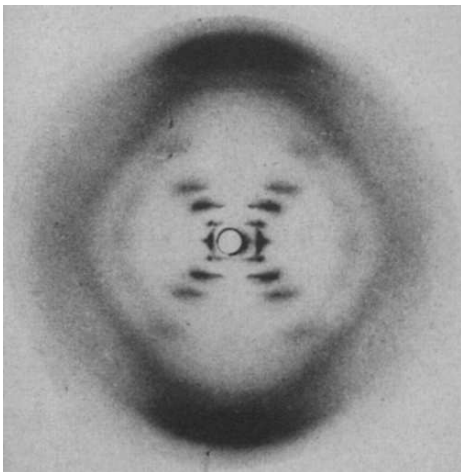
Figure 3.11: Part a) shows that the pitch of the small helix and the pitch of a large helix (coiled-coil). Part b) shows the coiled-coils with different numbers of strands. [Figure From Pauling, L., & Corey, R. B. (1953). *Nature* 171, 59.]

The Cross Pattern of α -Helix

Cochran, Crick and Vand developed a mathematical formulation for the α -helix structures brought up by Pauling and Corey in 1951 (8; 26). A continuous helix function of the radius r , helix angle θ and the pitch P can be characterized in cylindrical polar coordinates. They pictured the atoms sitting on the helix at a vertical interval p as shown in figure 3.12 a). They wrote down the discontinuous helix function by convoluting the continuous helix function with a set of points with spacing p in the fibre-axis. The Fourier transform of the whole convoluted function yields multiple crosses overlapping where the spacing between crosses scales as the inverse of the atom's spacing ($\frac{1}{p}$) and the spacing of the dots in one cross relates to the inverse of the pitch ($\frac{1}{P}$) (27), as shown in figure 3.12 b). The X-ray diffraction pattern of DNA was acquired by R. E. Franklin and R. Gosling in figure 3.12 c). Therefore, analysing the diffraction pattern can lead us back to the information related to the dimensions of the helix and the locations of the atoms in the helix.



(a) The pitch of the helix is P and the repeat of the atoms is p . The radius r and the helix angle θ is also pointed out. (b) The simulated pattern of the helix with pitch P and points spacing p .



(c) X-ray image of B form of DNA acquired by R. E. Franklin and R. Gosling. The diffraction pattern for the helix is the famous cross pattern.

Figure 3.12: The illustration and the X-ray pattern of the helix. [Part b) adapted from Sherwood, D. (1976). *Crystals, X-rays and proteins*, p. 578. Part c) from Franklin, R. E., & Gosling, R. G. (1953). *Nature*, 171, 740.]

3.3.2 The Diffraction Pattern of β -Sheets

In the 1930s, Astbury and Wood examined the X-ray diffraction pattern of stretched, wet hair and found that the hair went from the α -keratin pattern to another pattern they termed as β -keratin, which contains β -sheet structures (28). The signature diffraction pattern of β -sheets includes two equatorial peaks at 9.8 and 4.65 Å and a meridional peak at 3.3 Å as circled in figure 3.13. Astbury and Wood considered that β -sheets are formed by the β -strands which are the extended state of the polypeptide backbones and each strand in the β -sheets is connected by hydrogen bonds. Astbury and Wood had the right idea, but the structure we know nowadays was established by Pauling and Corey (9). The 3.3 Å peak originates from the rise per residue of the β -sheets (23). The 4.65 Å peak corresponds to the spacing between the strands inside the β -sheets and the 9.8 Å peak corresponds to the spacing of each β -sheet.

3.3.3 α and β -Chitin

α and β -chitin occur naturally in crystallite forms, which make it easier to obtain a well-defined X-ray diffraction pattern. Both structures have been well-studied previously. As shown in figure 3.14 and 3.15, the diffraction patterns and the crystal structures of α and β -chitin differ the most in the b^* direction. Using the lattice constant of α -chitin and β -chitin reported, as shown in table 3.1, we can simulate the diffraction pattern and compare the locations and the intensity of diffraction pattern to our data.

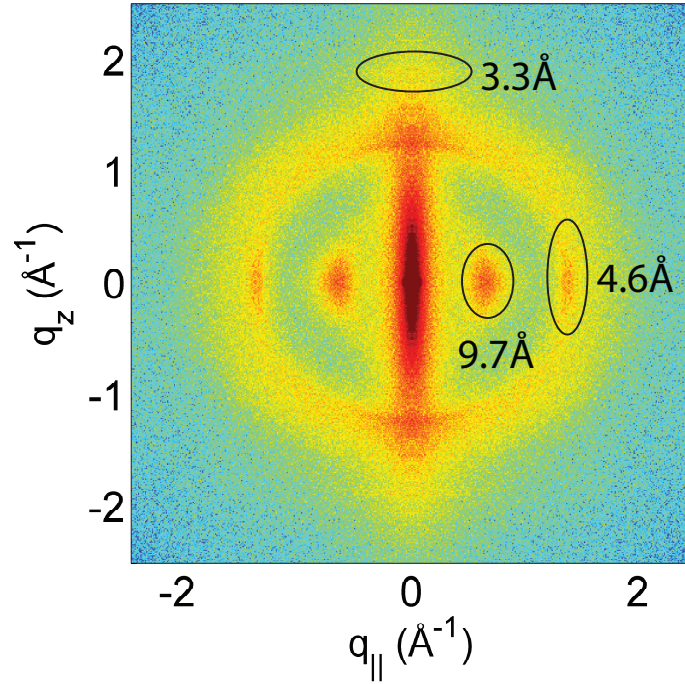


Figure 3.13: Two equatorial peaks at 9.7 and 4.6 Å and a meridional peak at 3.3 Å are circled. [Figure adapted from Pinto, N., Yang, F. C., Negishi, A., Rheinstadter, M. C., Gillis, T. E., & Fudge, D. S. (2014). *Biomacromolecules*, 15(2), 579.]

Type	a (Å)	b (Å)	c (Å)	γ (°)	space group
α -chitin	4.74	18.86	10.32	90	P 2 ₁ 2 ₁ 2 ₁
β -chitin	4.85	9.26	10.38	97.5	P 2 ₁

Table 3.1: Comparison of lattice parameters for α -chitin and β -chitin. [Table from Rinaudo, M. (2006). *Progress in polymer science*, 31(7), 606.]

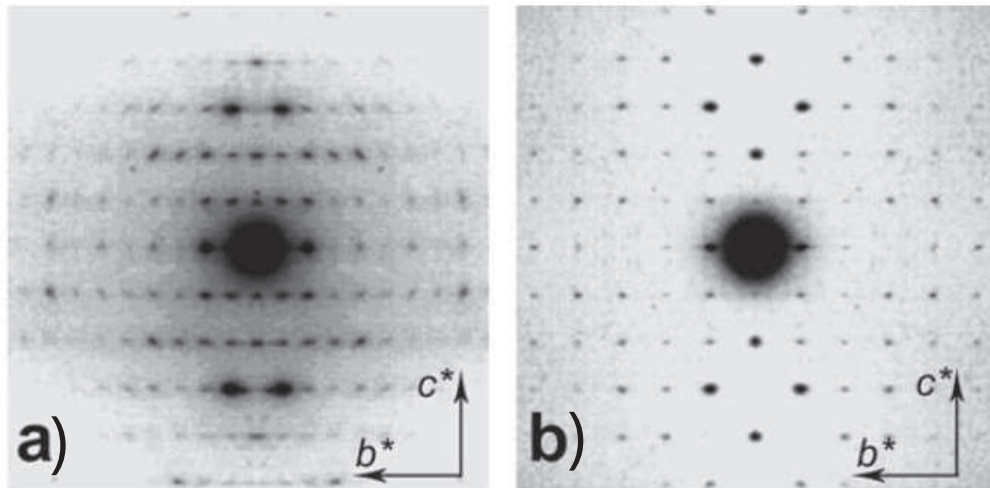


Figure 3.14: Diffraction pattern of a) α and b) β -chitin. [Figure from Rinaudo, M. (2006). *Progress in polymer science*, 31(7), 605.]

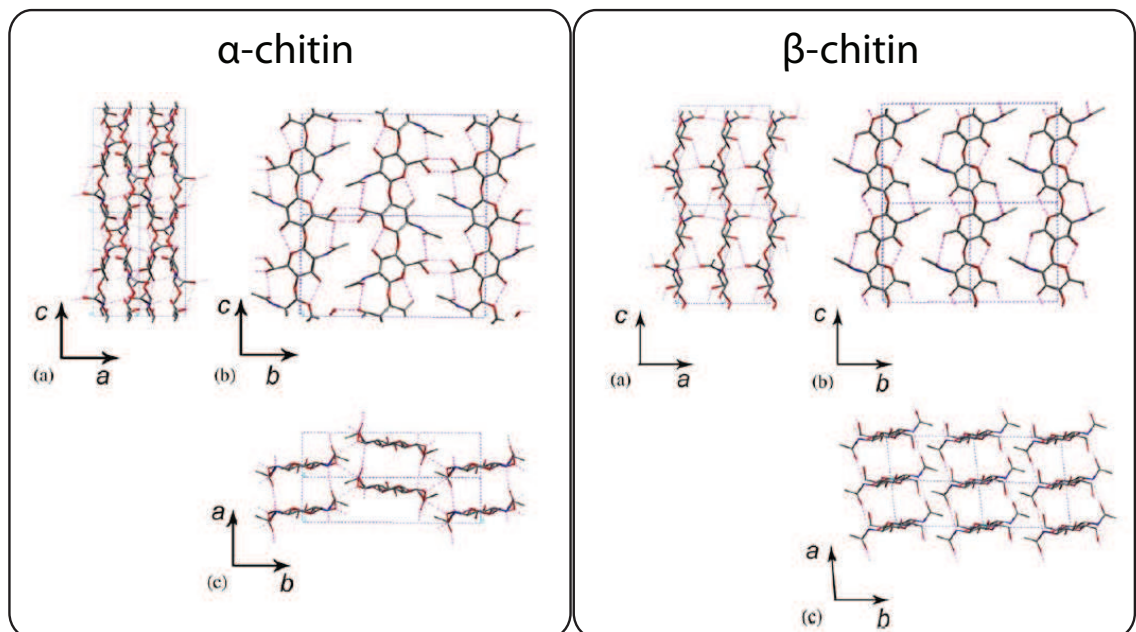


Figure 3.15: Crystal structures of α and β -chitin. [Figure from Rinaudo, M. (2006). *Progress in polymer science*, 31(7), 606.]

Chapter 4

Experimental Background of X-Ray Diffraction

4.1 Rigaku SmartLab Diffractometer

The Biological Large Angle Diffraction Experiments (BLADE) in the Laboratory for Membrane and Protein Dynamics at McMaster uses a Rigaku Smartlab diffractometer. Figure 4.1 shows the inside of BLADE. X-rays are generated at the X-ray source chamber, then passing through soller collimators and size limiting slits and onto the sample. The diffracted X-ray beam then passes through soller collimators again and arrives at the detector. We will introduce each component separately in the following sections.

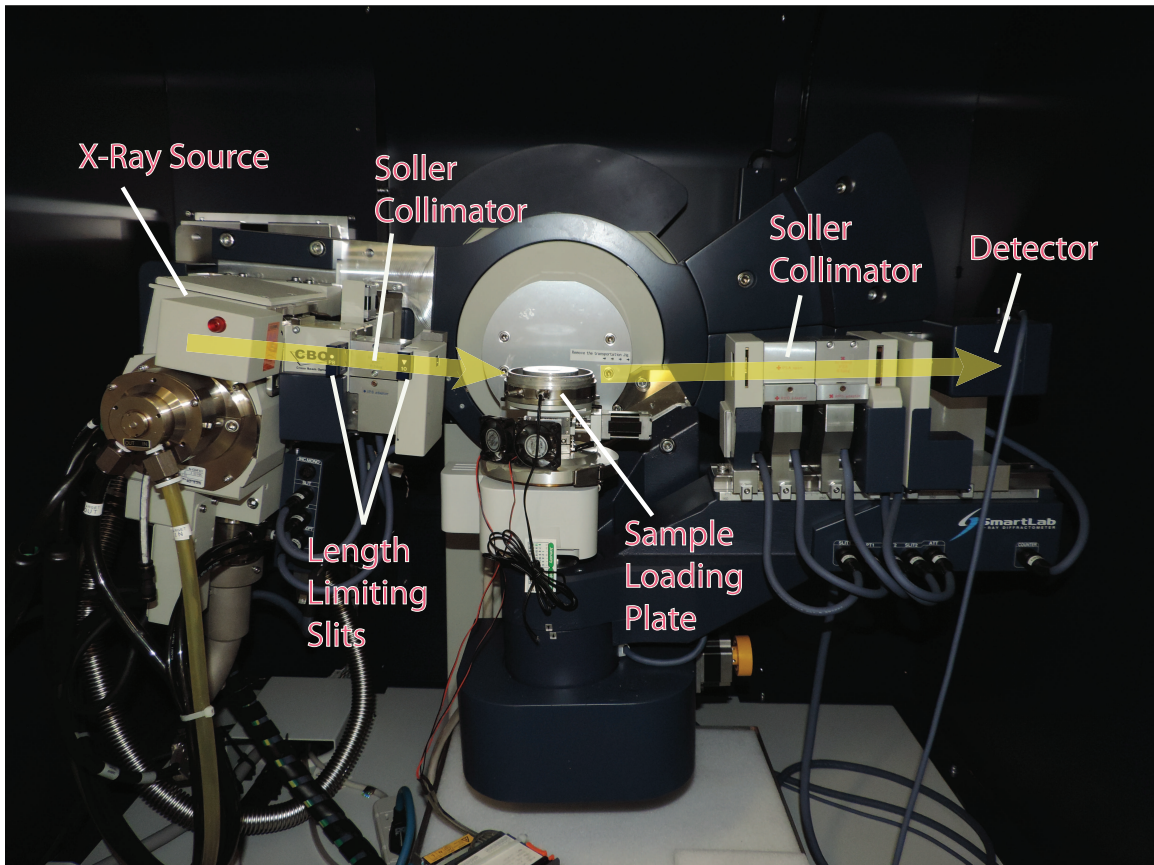


Figure 4.1: Interior of the Rigaku SmartLab Diffractometer.

Generation of X-Ray Sources

The Rigaku Smartlab diffractometer uses a rotating anode made of Copper (Cu) powered at 9 kW, which can generate up to 10^{10} photons per mm^2 per s at the sample position. X-rays are produced when the electrons emitted from the heated filament are suddenly stopped on the copper anode. This sudden de-acceleration of the electrons by the copper target produces so-called *bremstrahlung* radiation, which is the broad and continuous bottom spectrum shown in figure 4.2.

X-rays are also produced by specific electronic transitions in the electron shell of the copper target atoms. After the incident electrons kick out an electron in the

inner electron shell K of a copper atom, the electrons in the outer shells L/M will transfer to a lower energy state, thus occupying the vacancies. Two characteristic lines, K_α and K_β , correspond to the transitions between L to K shells and M to K shells, respectively, as shown in figure 4.2. All experiments presented here make use of the K_α wavelength $\lambda = 1.5418 \text{ \AA}$.

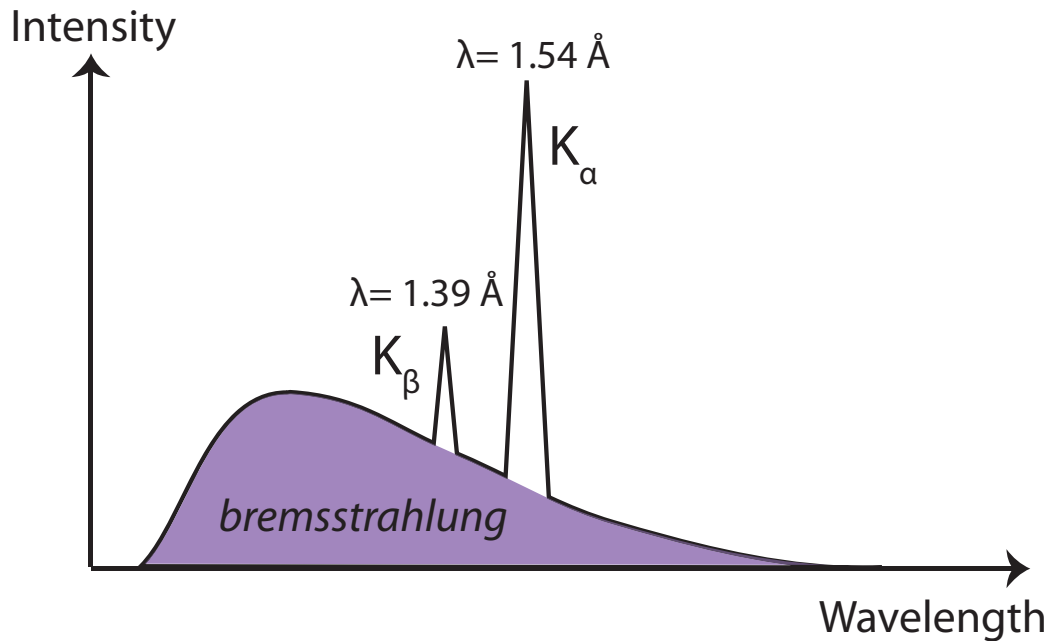


Figure 4.2: The X-ray spectrum is the superposition of the continuous *bremsstrahlung* spectrum, which is the broad contribution, and the target-specific characteristic spectrum made of sharp peaks K_α and K_β .

Soller Collimator

Soller collimators are made of parallel metal sheets spaced at few millimetres apart, as shown in figure 4.3. The function of the first soller collimator is to filter the incoming X-rays into a parallel beam. The function of the second soller collimator is to only let X-rays diffracted by the sample pass onto the detector. There are 0.5° and 5°

divergence collimators to choose from.

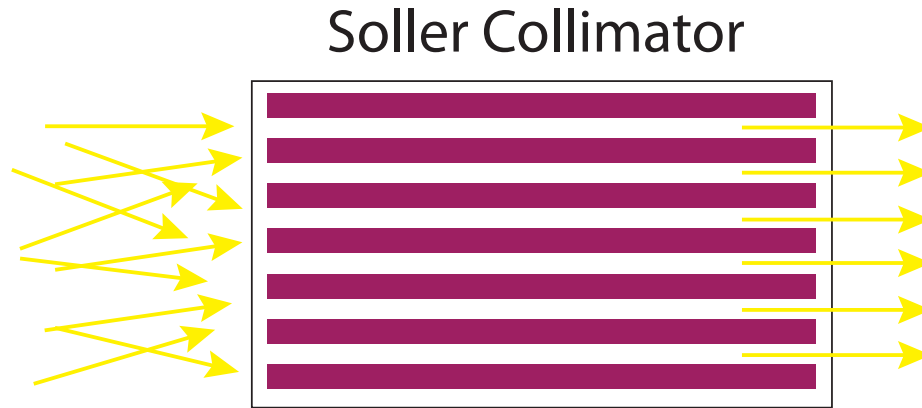


Figure 4.3: Illustration of the function of a Soller Collimator.

Size Limiting Slits

Two sets of slits are used to control the height and the width of the incident X-ray beam to maximize the resolution and the intensity. There are 2, 5, 10 mm height limiting slits and 0.5, 2, 5, 10, 15 mm width limiting slits to choose from. Additional slits are controlled by the SmartLab software, and can be adjusted to as small as 0.03 mm.

Detector

Intensity is collected by a NaI scintillation counter. The diffracted photons hit the scintillator made of a sodium iodide crystal, and the scintillator produces photons. These photons are multiplied by the photomultiplier attached behind the scintillator, and later transformed into electrical signals proportional to the original number of diffracted photons.

4.2 Experimental Procedure

4.2.1 X-Ray Fibre Diffraction

A fibre is highly anisotropic. Molecular structure is randomly oriented in the plane of the fibre, which means that if you rotate the fiber around the fibre axis, you will get exactly the same diffraction pattern.

In our fibre diffraction experiment, the fibres were mounted horizontally. A single fibre was chosen based on how strongly it scatters. Fibres are mounted horizontally to make optimal use of the horizontal beam and maximize the scattered intensity. In addition, single fibre experiments can minimize the smearing effect due to the disorientation between multiple fibres. Finally, the q_{\parallel} direction has a much higher resolution as compared to q_z . This is beneficial to probe the small angle q_{\parallel} structures, which are often related to the configuration of intermediate filaments in the plane of fibres.

Vimentin Fibre

This project is in collaboration with Nicole Pinto, Dr. Atsuko Negishi, Dr. Todd E. Gillis, and Dr. Douglas S. Fudge from the Comparative Biomaterials Lab at University of Guelph. They are leading experts in the hagfish fibre research, specializing in fibre fabrication and material property testing.

Vimentin proteins were extracted and purified from *E coli*. cells containing recombinant vimentins. For the first category of the fibres, the concentrated vimentin protein solution was deposited on to the surface of the buffer solution made of a mixture of $MgCl_2$ and HEPES solutions. A thin film was formed on the surface and

pulled by forceps into a single-drawn fibre. The second category of fibre was made by adding vimentin solutions into a NaCl solution and later centrifuged to form a film onto the tube. The film containing tangled filaments was pulled into a single-drawn fibre. For the last category, the NaCl solution was changed to Mg^{+} , but the same procedure was used. All the double-drawn fibres were made by submerging single-drawn fibres in 50% of methanol solution and pulled to approximately double the length. Fibres were carefully taped to a hard cardboard that has a rectangular cut out, and wrapped in a bubble mailer to transfer to McMaster.

Fibres were stored in Laboratory for Membrane and Protein Dynamics at room temperature. The entire cardboard was mounted on the sample loading plate as shown in figure 4.4. A single fibre with maximal intensity was selected for the X-ray experiment.



Figure 4.4: a) shows forceps drew from the surface of the solution into fibres. b) shows that fibres were taped horizontally on a cardboard. c) shows the setup of the X-ray experiment.

Squid Pen

Squid samples were purchased at local fish market in Tainan, Taiwan and Toronto, Canada. Squids were cut with surgical scissors along the centre of mantles. Squid pen was removed from the squid, then washed thoroughly using de-ionized 18.2 M

Ω -cm water produced by a Cascade LS water system. A $2 \times 1 \text{ cm}^2$ rectangle on one side of the squid pen was cut by a scissor and squeezed between two pieces of metal as shown in the figure 4.5. The metal apparatus has a cut out that allows X-ray to pass through the squid pen. Note that we purposely aligned the long axis of squid pen along the z-axis of the apparatus. The apparatus was stored in a magnesium nitrate atmosphere ($\text{Mg}(\text{NO}_3)_2$) which produces a $52.9 \pm 0.22 \%$ relative humidity (RH) before X-ray experiments. To control the humidity during the experiments, the sample was mounted in a humidity chamber with a magnesium nitrate atmosphere inside.

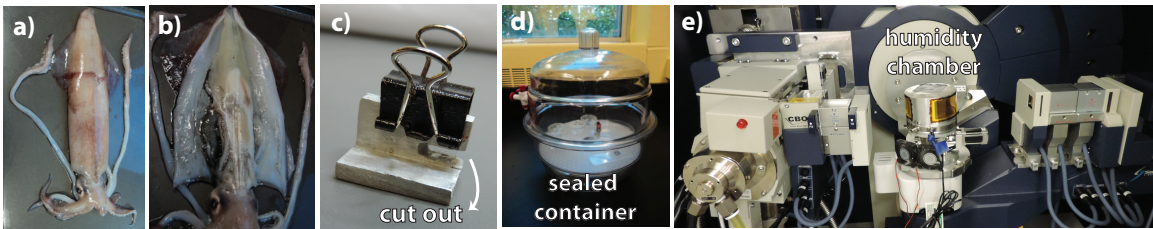


Figure 4.5: a) shows a complete squid. b) shows the dissected squid and the transparent squid pen in the middle. c) shows the metal apparatus to squeeze a piece of squid pen in between. d) shows the sealed container for storage. e) shows the humidity chamber mounted on BLADE.

Hair

The experimental process was introduced in figure 4.6. Scalp hair was gathered from 12 different subjects. Hair was collected one by one manually into a bundle of around 10 hair strands, then taped onto a cardboard with a cut out. Hair samples were stored under room temperature. X-ray diffraction was focused at a height where the intensity was maximized, which often involves a few hair strands together. Corresponding intensity was gathered for further analysis.

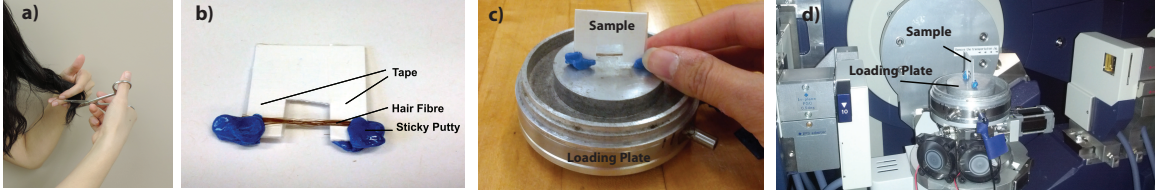


Figure 4.6: a) shows how the hair is cut on the subject. b) shows how hair strands were mounted on the cardboard. c) shows the hair sample on the loading plate. d) shows the setup for X-ray experiments.

4.3 Building Two-Dimensional Reciprocal Space

The equations used for plotting 2-dimensional intensity plot are:

$$|\vec{q}_z| = \frac{4\pi \sin(\theta)}{\lambda}, \quad (4.1)$$

$$|\vec{q}_{||}| = \frac{4\pi \sin(\chi)}{\lambda}. \quad (4.2)$$

For most experiments, the range of 2θ was chosen between 0° - 40° , and 2χ was between 0° - 30° , which corresponds to a range of q_z from 0 - 2.5 \AA^{-1} and $q_{||}$ from 0 - 2 \AA^{-1} . The scans are done in steps as illustrated in figure 4.7: a) both the X-ray sources and the detector are in a horizontal plane and the detector moves from $2\chi=0^\circ$ to 30° . b) The X-rays source and the detector angle is increased by $\Delta 2\theta=0.25^\circ$. c) The detector stays on the $2\theta=0.25^\circ$ plane, carrying out the $2\chi=0^\circ$ to 30° scan. Each scan (horizontal strip) having around 200 data points takes about 10 minutes to finish. The entire 2-dimensional data has around 200 scans, which usually takes 30-40 hours to run.

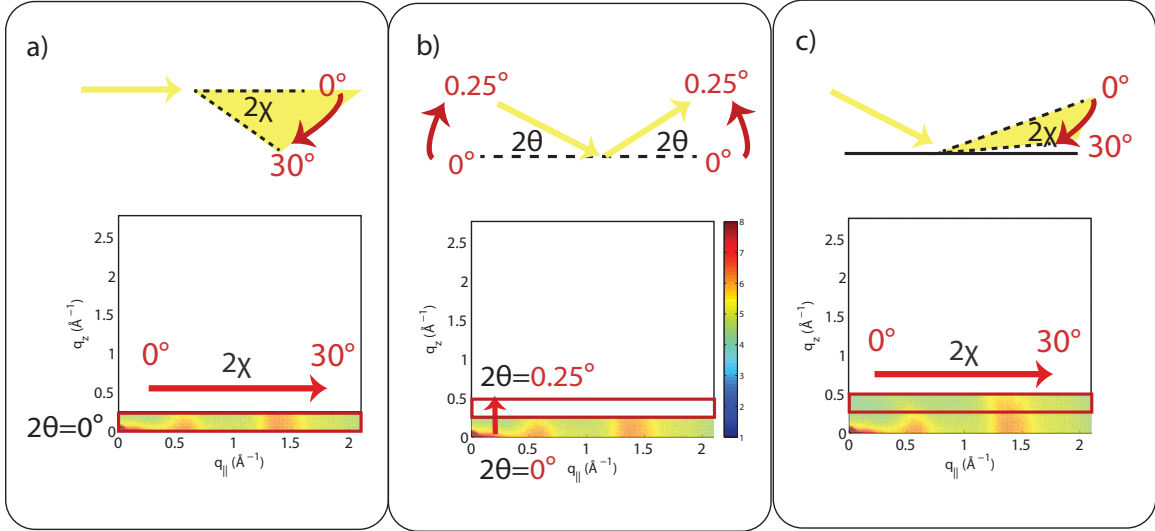


Figure 4.7: a) shows that detector goes from $2\chi=0$ to 30° to run the first scan. b) shows that X-ray source and the detector moves to $2\theta=0^\circ$ to 0.25° to setup for the second scan. c) shows the detector moves from $2\chi=0^\circ$ to 30° again to finish the second scan. Below is the corresponding diagram for the 2-dimensional reciprocal space data.

4.4 Acquiring Information from the Data

Once the 2-dimensional data is acquired, we can examine more closely at the directional structures. To acquire the $q_z/q_{||}$ vs intensity plot, we can integrate 25 degrees azimuthally from meridian/equator at every 0.15 degree spacing to include the features oriented along the $q_z/q_{||}$ direction as show in figure 4.8. The $q_z/q_{||}$ vs intensity plot will be separately fitted by Gaussian or Lorentzian peak functions.

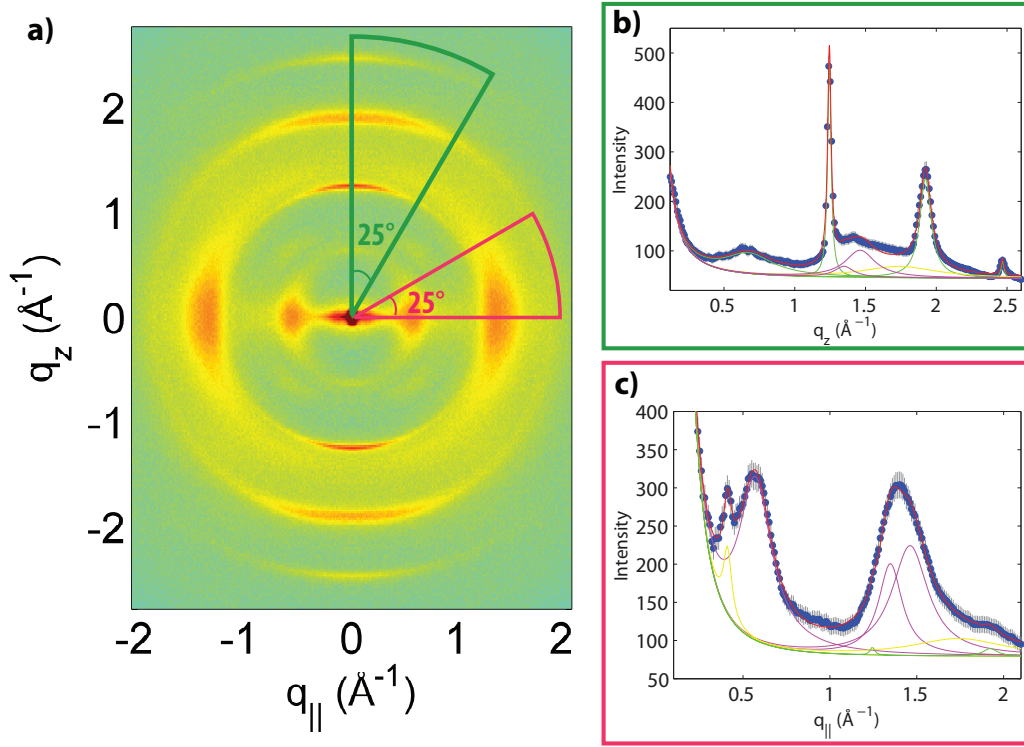


Figure 4.8: a) shows the area integrated for the $q_z/q_{||}$ vs intensity plot. b) shows q_z vs intensity plot. c) shows $q_{||}$ vs intensity plot.

Gaussian peak profiles are described by:

$$G(x) = a \exp\left(-\frac{(x-b)^2}{2\sigma^2}\right) + c. \quad (4.3)$$

a is related to the peak height of the Gaussian. b is the position of the centre of the Gaussian. σ is related to the width of the Gaussians, i.e., the standard deviation. c is the offset.

The full width at half maximum (FWHM) is related to σ by:

$$FWHM = 2\sqrt{2\ln 2} \sigma = 2.35 \sigma, \quad (4.4)$$

which is a little bit larger than the full width.

Lorentzians are of the form:

$$L(x) = a \frac{w}{w^2 + (x - b)^2} + d, \quad (4.5)$$

where a is the peak height of the Lorentzian, w is the width (HWHM), b is the position of the centre, and d is the offset with:

$$FWHM = 2w. \quad (4.6)$$

Chapter 5

X-Ray Diffraction of Biomaterials

5.1 Paper I: Self-assembly Enhances the Strength of Fibres Made from Vimentin Intermediate Filament Proteins

Nicole Pinto, Fei-Chi Yang, Atsuko Negishi, Maikel C. Rheinstädter, Todd Gillis, and Douglas Fudge. “*Self-assembly enhances the strength of fibres made from vimentin intermediate filament proteins*”, *Biomacromolecules*, 2014, 15 (2), 574–581

5.1.1 Preface to Paper I

Extensive research has been done on the fabrication of synthetic fibres. The goal is to mimic the natural fibres, such as spider silk, that have exceptional mechanical properties such as high breaking stress and high toughness.

Stress-strain curves of the viminten fibres have been tested mechanically at Comparative Biomaterials Lab at University of Guelph led by Dr. Douglas Fudge. It was found that the double-drawn viminten fibres cross-linked with magnesium have improved their breaking stress from 42 to 173 mPa compared to the single-drawn fibres. The question is then what happens exactly on the molecular level that leads to such dramatic change macroscopically. A good candidate to probe the molecular scale is X-ray diffraction.

The X-ray diffraction setup was optimized by using a single fibre and choosing a slit width that matches the diameter of the fibre to enhance the resolution. The quality of the data acquired by BLADE has significantly improved as compared to synchrotron data acquired by Dr. Fudge from previous work. For the data analysis, we built a macro to perform the integration along the azimuthal angle using given radius segment.

This experiment allowed us to study the α -helical coil-coiled in the single-drawn fibres. The β -sheet patterns and the more defined signals from the α -helical coil-coiled are also visible in the double-drawn fibres. Therefore, we confirmed the hypothesis that α -to- β transition results in the presence of more β -sheets and the better alignment of the coiled-coils and β -sheets, which enhance the mechanical performance of the fibres.

Author Contributions

- *Experiment Design:* Douglas S. Fudge, Todd E. Gillis, and Maikel C. Rheinstädter
- *Sample Fabrication:* Nicole Pinto and Atsuko Negishi

- *Experiment Performing:* Nicole Pinto, **Fei-Chi Yang**, Atsuko Negishi, Maikel C. Rheinstädter, Todd E. Gillis, and Douglas S. Fudge
- *Data Analysis:* Nicole Pinto, **Fei-Chi Yang**, and Atsuko Negishi
- *Manuscript Writing:* Nicole Pinto, **Fei-Chi Yang**, Atsuko Negishi, Maikel C. Rheinstädter, Todd Gillis, and Douglas Fudge



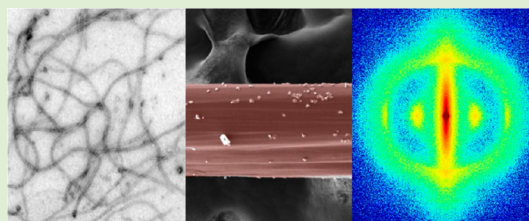
Self-Assembly Enhances the Strength of Fibers Made from Vimentin Intermediate Filament Proteins

Nicole Pinto,[†] Fei-Chi Yang,[‡] Atsuko Negishi,[†] Maikel C. Rheinstädter,[‡] Todd E. Gillis,^{*,†,§} and Douglas S. Fudge^{*,†,§}

[†]Department of Integrative Biology, University of Guelph, Guelph, Ontario N1G 2W1, Canada

[‡]Department of Physics and Astronomy, McMaster University, Hamilton, Ontario L8S 4M1, Canada

ABSTRACT: Hagfish slime threads were recently established as a promising biomimetic model for efforts to produce ecofriendly alternatives to petroleum polymers. Initial attempts to make fibers from solubilized slime thread proteins fell short of achieving the outstanding mechanics of native slime threads. Here we tested the hypothesis that the high strength and toughness of slime threads arise from the ability of constituent intermediate filaments to undergo a stress-induced α -to- β transition. To do this, we made fibers from human vimentin proteins that were first allowed to self-assemble into 10 nm intermediate filaments. Fibers made from assembled vimentin hydrogels underwent an α -to- β transition when strained and exhibited improved mechanical performance. Our data demonstrate that it is possible to make materials from intermediate filament hydrogels and that mimicking the secondary structure of native hagfish slime threads using intermediate filament self-assembly is a promising strategy for improving the mechanical performance of biomimetic protein materials.



INTRODUCTION

Since the mid-1970s, petroleum prices have entered a phase of high volatility, which has spurred investment not only in alternative energy technologies but also in alternative materials that can be made without petroleum feedstocks. Natural fibers such as spider silks demonstrate that it is possible to produce high performance materials from sustainable feedstocks (i.e., protein) using aqueous chemistry.¹ In recent years, hagfish slime threads have emerged as a new biomimetic model for the production of fibrous protein materials with high strength and toughness.² Slime threads are a promising model because they are produced in the hagfish slime gland via mechanisms that may be easier to mimic than the complex mechanisms of silk spinning in spiders. Furthermore, they are built within cells from intermediate filament (IF) proteins, which are known to be able to self-assemble *in vitro* into 10 nm diameter filaments.

When hagfish are disturbed, they produce a slime that results from the mixing of products from two cell types in the slime glands: gland thread cells (GTCs) and gland mucous cells (GMCs).^{3–5} GTCs each produce a single thread that is about 150 μm long in mature cells and 1–3 μm in diameter.^{4,6,7} The thread is assembled from IF proteins α and γ , which have been classified as “keratin-like” because they possess all of the primary and secondary structural hallmarks of IFs.^{8,9} A recent study found that draw-processed slime threads possess mechanical properties that rival spider dragline silk.² Negishi et al.¹⁰ recently described a method by which fibers could be produced from formic acid solubilized hagfish slime thread proteins. The method involves pipetting a small volume of solubilized protein onto an electrolyte buffer and then drawing

a fiber from the film that forms on the surface.¹⁰ Fibers produced using this method possess mechanical properties that are inferior to native hagfish slime threads. The performance gap between native slime threads and these reconstituted fibers may be due to differences in protein structure and alignment. Native threads are produced from aligned bundles of IFs, whose structure is dominated by α -helical coiled-coils.¹¹ When slime threads are mechanically strained in water, the α -helices are extended, allowing for the formation of β -sheets and β -sheet crystallites, which endow the thread with high strength and toughness.¹² Negishi et al.¹⁰ did not find evidence for coiled-coils or β -sheet crystallites in their fibers, nor any evidence that draw-processing of the fibers effects an $\alpha \rightarrow \beta$ transition as seen in native threads.

If native slime threads are stronger than those made from formic acid solubilized protein because of their ability to undergo an $\alpha \rightarrow \beta$ transition, we reasoned that it should be possible to boost the strength of artificial fibers by starting with proteins that possess some of the same structural characteristics within native threads. To do this, we made fibers from proteins that were first allowed to self-assemble into 10 nm diameter IFs. Our original intent was to assemble urea-solubilized hagfish slime thread proteins into IFs using a protocol published by Downing et al.¹¹ However, we (and others) have been unable to replicate filament assembly using their protocol or a number of variations on it (unpublished observations). We suspect that

Received: October 30, 2013

Revised: December 21, 2013

Published: December 23, 2013

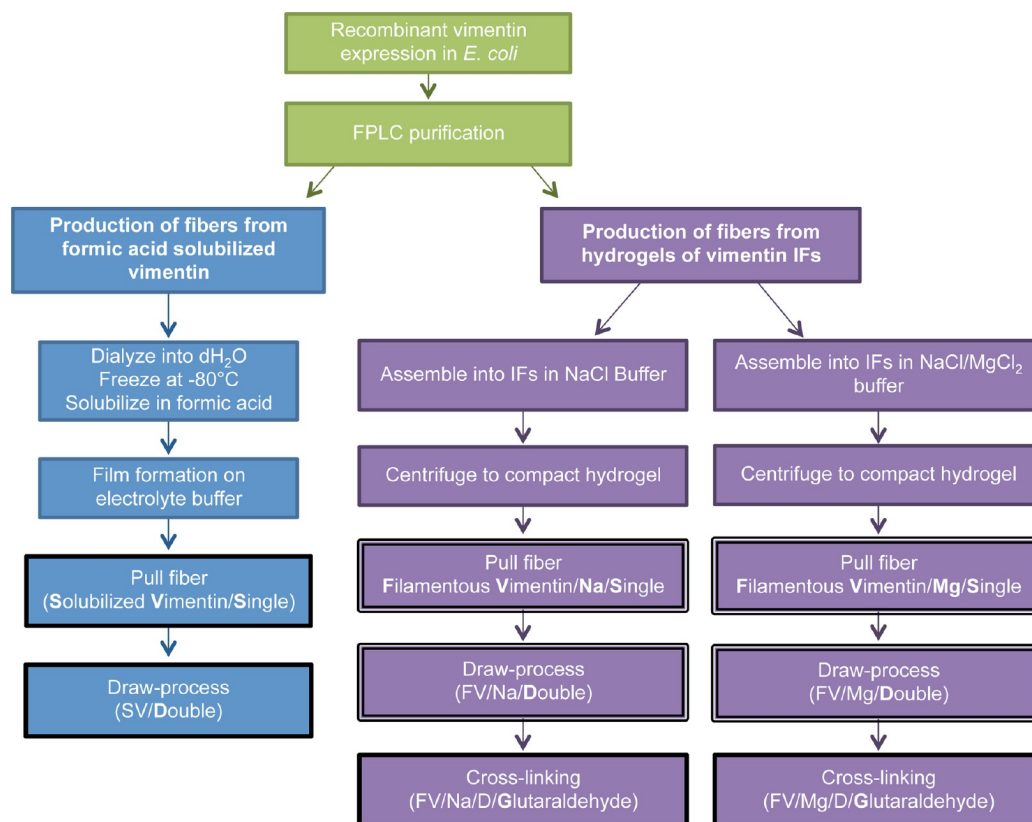


Figure 1. An overview of the two main methods used to make fibers from recombinant vimentin protein, using formic acid solubilized vimentin or hydrogels of assembled vimentin filaments. Boxes with a bold border denote the eight different fiber types that were characterized by tensile testing, and those with a double border also underwent structural analysis using wide-angle X-ray scattering (WAXS).

covalent modifications of thread proteins that occur during thread maturation¹³ hinder the self-assembly process *in vitro*.

We therefore chose to work with an IF protein that has been intensively studied, the Type III IF protein, vimentin.^{14,15} Human vimentin is a major cytoskeletal component of mesenchymal cells and is 54 kDa in size. This protein is also routinely made in research laboratories using recombinant bacteria, and detailed protocols exist for its self-assembly from urea-solubilized protein into networks of entangled high-aspect ratio IFs. Unlike hagfish slime thread IFs, which are heteropolymeric, vimentin IFs are homopolymeric, which further simplifies their production in the laboratory.

In the current study, we show that it is possible to make macroscopic materials from recombinant vimentin IFs, and we show that draw processing and Mg²⁺ cross-linking result in fibers with properties that are superior to previous attempts to make artificial materials from IF proteins. Structural data from WAXS experiments support the hypothesis that improvements in mechanical performance can be achieved by effecting an $\alpha \rightarrow \beta$ transition of IFs during draw processing.

■ MATERIALS AND METHODS

Protein expression. Recombinant vimentin was produced using a pDSS plasmid containing the nucleotide sequence of the full-length human vimentin gene (NM_003380.3).¹⁶ The plasmid was trans-

formed into NovaBlue competent *E. coli* cells (Novagen, San Diego, CA, USA) using the standard protocol provided by the manufacturer. Using the High Pure Plasmid Isolation Kit (Roche Diagnostics, Indianapolis, IN, USA), plasmid DNA was purified and then sequenced to confirm the identity of the gene.

The pDSS plasmid containing the vimentin cDNA was transformed into BL21-Gold(DE3) competent cells (Agilent Technologies, La Jolla, CA, USA) and grown on Luria-Bertani (LB) media agar containing 60 $\mu\text{g}/\text{mL}$ carbenicillin. Growth plates were incubated overnight at 37 °C and the next day 100 mL of terrific broth (TB) containing 60 $\mu\text{g}/\text{mL}$ carbenicillin was inoculated with 10 colonies from these plates. Cultures were agitated at 250 rpm at 37 °C overnight in an Excella E-25 Incubator Shaker (New Brunswick Scientific, Enfield, CT, USA).

Seven flasks containing 1 L of TB and carbenicillin (60 $\mu\text{g}/\text{mL}$) were inoculated with 10 mL of the overnight culture and shaken at 37 °C for 10 h until an optical density at 600 nm of approximately 1.8 was reached. These cells were harvested by centrifugation (6000 g) for 5 min at 4 °C. A sample from these pelleted cells was run on a 10% SDS-PAGE gel and then stained with Coomassie Brilliant blue G-250 (Bio-Rad, Hercules, CA, USA), which confirmed recombinant vimentin protein expression and accumulation in inclusion bodies. The pellet was solubilized using a series of seven buffers with sonication at each step.¹⁷ The supernatant was stored at -20 °C.

Protein purification. Vimentin protein was purified on two consecutive columns using fast protein liquid chromatography (FPLC).^{17,18} A fast flow diethylaminoethyl (FF DEAE) column was

used first, with the vimentin protein diluted 10-fold using column running buffer (8 M urea, 5 mM Tris-HCl (pH 7.5), 1 mM EDTA, 0.1 mM EGTA, 1 mM DTT) (Herrmann and Aebi, 2004). Proteins bound to the column were eluted using an elution buffer (EB) consisting of the column running buffer plus 0.3 M KCl. The concentration of KCl running through the column was increased in six incremental steps by increasing the percentage of EB (11.5%, 15%, 21%, 31%, 37% and 100% EB). A fraction collector was used to collect all eluent and SDS-PAGE was used to determine the fractions containing the recombinant vimentin protein. The samples containing the target protein were pooled and then further purified using a carboxy methyl (CM) sepharose column using the same running and elution buffers. Pooled samples were dialyzed back into running buffer before they were applied to the CM column with a three-step elution gradient (11.5%, 33% and 100% EB). SDS-PAGE was used to identify the fraction containing the target protein as well as establish the purity of the samples. The fractions containing the target protein were pooled and stored at -20°C with 10 mM methylammonium chloride (Herrmann et al., 2004).

Prior to filament assembly, the protein sample was thawed on ice and dialyzed (12–14 kDa MWCO)¹⁷ against a series of buffers with decreasing urea concentrations (6, 4, 2 M urea in 5 mM Tris-HCl (pH 8.4), 1 mM DTT) at room temperature for 1 h each, followed by an additional dialysis against fresh buffer (5 mM Tris-HCl (pH 8.4), 1 mM DTT), which did not contain any urea, overnight at 4°C . Aquacide II (EMD Millipore, Darmstadt, Germany) was used to concentrate the protein sample by removing about half of the initial volume of water. Changes in protein concentrations were measured using a Bradford assay and visualized using SDS-PAGE (Figure 2A).

Freeze-drying and solubilization in formic acid. Purified vimentin protein was dialyzed into dH_2O over three days with 3 dH_2O changes and lyophilized using a Virtis AdVantage freeze-dryer and stored at -80°C . Freeze-dried samples (10% (w/v) protein concentration) were dissolved in 98% formic acid (Acros Organics, Geel, Belgium) and stirred in a closed container at room temperature for 3 h. The resulting solution was centrifuged at 17,000 g for 20 min. The white, unsolubilized pellet was discarded and the supernatant used immediately for fiber production.¹⁰

Fiber formation with formic acid solubilized vimentin. One μL of formic acid solubilized vimentin was applied to the surface of a 200 mM MgCl_2 , 20 mM HEPES buffer (pH 7.5) solution.¹⁰ After 20 s, a fiber was formed by drawing the resultant film using forceps and draping it over a 1 cm gap in a square of Nylon mesh (Figure 3A-D). Such fibers are referred to as the formic acid solubilized vimentin single-drawn fibers (SV/S) (Figure 1). When a subset of the fibers were dry, they were submerged in an aqueous 50% methanol solution for 5 min and stretched to approximately double their original length (from approximately 2 to 4 cm). These fibers are referred to as the formic acid solubilized vimentin double-drawn fibers (SV/D) (Figure 1).

Vimentin Filament Assembly and Fiber Formation from Hydrogels. Filament assembly was initiated by adding 500 μL of purified recombinant vimentin to an equal volume of NaCl assembly buffer (NAB), which consisted of 40 mM Tris-HCl (pH 7.0) and 200 mM NaCl. Full-length filaments were assembled at 37°C for 1 h. Transmission electron microscopy (TEM) was used to visualize filaments during and immediately after assembly. For TEM, filament assembly was arrested with a buffer containing equal parts dialysis buffer (0 M urea) and NAB containing 0.2% glutaraldehyde (pH 7.5). TEM was carried out within 5 min of the addition of the 0.2% glutaraldehyde buffer.

For fiber formation, assembled vimentin filaments were centrifuged at 17000 g for 1 h to compact the hydrogel of entangled filaments, resulting in a visible gelatinous film on one side of the tube. Using a pipet tip, the edges of the film were lifted until it was possible to lift the whole film and pull it into a fiber. Fibers were air-dried overnight, and a subset of them was submerged in 50% aqueous methanol for 5 min and stretched between two pairs of forceps to an approximate strain of 50–100% and left to air-dry. Fibers made using this method are referred to as the filamentous vimentin single-drawn (FV/Na/S)

and double-drawn (FV/Na/D) fibers. Noncovalent cross-linking was carried out by assembling filaments in an assembly buffer containing 16 mM Mg^{2+} , which has been shown to stiffen vimentin hydrogels.¹⁹ Fibers made using this method are referred to as the filamentous vimentin Mg^{2+} single-drawn (FV/Mg/S) and double-drawn (FV/Mg/D) fibers (Figure 1).

A subset of the above double-drawn fibers was covalently cross-linked by exposing them to an aqueous 8% glutaraldehyde solution for 30 min, rinsing them with dH_2O , and allowing them to air-dry.² Fibers made using this method are referred to as FV/Na/D/G and FV/Mg/D/G fibers (Figure 1).

Material Properties of Vimentin Fibers. Fibers were mounted onto a cardstock paper frame and glued at both ends using Elmer's carpenter's wood glue. Fiber diameters and lengths were measured using a Nikon Eclipse 90i Epifluorescent microscope and NIS Elements AR v.6 software. Cross-sectional areas were calculated from diameters measured at 10 different locations evenly distributed along the length of the fiber. Tensile testing was performed using an Instron single column universal testing machine (model 3343; Instron, Norwood, Massachusetts, U.S.A.), with a 10 N load cell and a constant crosshead speed of 0.3 mm/min. Tests were performed at room temperature (23°C) and at a relative humidity of 22–26%. Breaking stress (or "strength") was calculated as the engineering stress at failure, and breaking strain was calculated as the strain ($\Delta L/L_0$) at failure. Young's modulus was calculated as the slope of the stress/strain curve at the elastic region of the curve prior to the yield point. Strain energy at failure (or "toughness") was calculated by measuring the area under the stress/strain curve.

Scanning Electron Microscopy (SEM). Fibers were mounted onto SEM stubs using carbon tape and sputter coated using a Cressington model 108 auto system (final gold thickness ~ 10 nm). SEM images of fibers were collected using an FEI Inspect S50 scanning electron microscope at an accelerating voltage of 20 kV with an aperture of 3.5 using an ETD secondary electron detector.

Transmission Electron Microscopy (TEM). IF assembly was confirmed by TEM using a LEO 912am TEM with a Cantega OSIS camera and iTEM software. Filament assembly was arrested with a buffer containing equal parts of dialysis buffer (0 M urea) in combination with NAB and 0.2% glutaraldehyde (pH 7.5), and visualization with TEM was carried out within 5 min of glutaraldehyde fixation. Negatively stained (2% uranyl acetate) whole mounts were placed on Formvar coated 200 mesh copper grids, and the TEM was operated at 100 kV.

X-ray Scattering. Two-dimensional X-ray diffraction patterns were recorded using the biological large angle diffraction experiment (BLADE) in the Laboratory for Membrane and Protein Dynamics at McMaster University. BLADE uses a 9 kW (45 kV, 200 mA) Cu $K\alpha$ Rigaku Smartlab rotating anode at a wavelength of 1.5418 Å. Focusing multilayer optics provides a high intensity parallel beam with monochromatic X-ray intensities up to 10^{10} counts/(s $\cdot\text{mm}^2$). A single fiber was selected and aligned parallel to the beam with typical slit settings of ~ 100 μm (the diameter of the fibers, as listed in Tables 1 and 2) \times 10 mm (along the fiber axis), and scattering signals in the equatorial plane and along the fiber axis were recorded.

Statistical Analysis. Statistical analyses were conducted using SigmaStat for Windows (v. 12.3). A two-way ANOVA was used to examine the main effects of draw-processing and assembly conditions, as well as the interaction between these two factors. Pairwise comparisons were done between treatments that differed in the level

Table 1. Summary of Mechanical Properties of SV Fibers^a

fiber type	diameter (μm)	break stress (MPa)	break strain ($\Delta L/L_0$)
SV/S (8)	227.4 \pm 18.0	3.4 \pm 0.6	1.54 \pm 0.1
SV/D (7)	65.4 \pm 6.1*	68.5 \pm 10.7*	0.4 \pm 0.1*

^aAsterisks (*) indicate significant differences between single and double drawn fibers according to a *t* test ($p < 0.05$). Sample sizes are indicated in parentheses. Values are mean \pm standard error.

Table 2. Summary of Mechanical Properties of FV Fibers Showing the Effects of Assembly Buffer (Na vs Mg), Draw Processing (S vs D), and Cross-Linking with Glutaraldehyde (G)^a

Fiber Type	Diameter (μm)	Break Stress (MPa)	Break Strain ($\Delta L/L_0$)	Young's Modulus (GPa)	Strain Energy (MJ/m^3)
FV/Na/S (13)	$130.0 \pm 10.6^{*\dagger}$	$50.5 \pm 7.3\§$	0.8 ± 0.2	2.1 ± 0.6	14.9 ± 2.9
FV/Mg/S (14)	$223.4 \pm 13.8^{*\ddagger}$	$41.6 \pm 4.8^\dagger$	$1.1 \pm 0.2^*$	1.6 ± 0.5	$18.9 \pm 3.6\§$
FV/Na/D (9)	$92.1 \pm 7.6\§^\dagger$	$95.5 \pm 12.2^{*\§}$	0.4 ± 0.1	2.2 ± 0.3	$26.6 \pm 6.1^*$
FV/Mg/D (11)	$156.7 \pm 14.7\§^\ddagger$	$173.2 \pm 15.4^{*\dagger}\bullet$	$0.6 \pm 0.1^*$	$3.4 \pm 0.3\bullet$	$89.5 \pm 18.8^{*\§}\bullet$
FV/Na/D/G (11)	105.5 ± 17.8	99.8 ± 9.8	0.4 ± 0.1	2.3 ± 0.3	31.9 ± 5.3
FV/Mg/D/G (12)	183.9 ± 18.0	$94.3 \pm 11.6\bullet$	0.4 ± 0.1	$2.3 \pm 0.2\bullet$	$31.8 \pm 5.6\bullet$

^aIn the top four rows, matching symbols (*, §, †, ‡) within the same column indicate significant differences from pairwise comparisons, which were made between treatments that differed in the level of one factor only (e.g., FV/Na/S vs FV/Na/D and FV/Na/S vs FV/Mg/S); treatments that differed in the level of two factors (e.g. FV/Na/S vs FV/Mg/D) were not compared. In the bottom four rows, solid circles (●) indicate a significant difference between the glutaraldehyde cross-linked fiber and its un-cross-linked control (e.g., FV/Na/D/G vs FV/Na/D) according to a *t* test ($p < 0.05$). Sample sizes are indicated in parentheses. Values are mean \pm standard error. A two-way ANOVA revealed significant main effects of assembly buffer ($p = 0.001$) and draw-processing ($p \ll 0.001$) on break stress

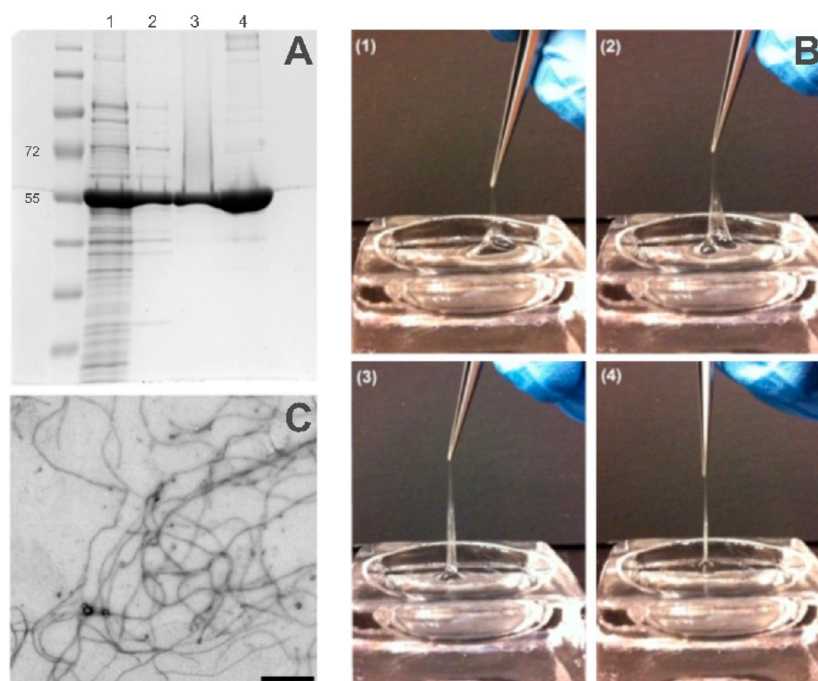


Figure 2. Vimentin purification and fiber and filament formation. (A) SDS-PAGE of proteins isolated from bacteria expressing recombinant vimentin. Left lane is mw ladder, (1) total protein, (2) after purification with FF DEAE column, (3) after purification with FF DEAE and CM sepharose columns, and (4) all purification steps plus Aquacide II to concentrate proteins. (B) SV fiber formation using the formic acid solubilized vimentin and methods from Negishi et al.¹⁰ (C) FV fibers were made from vimentin proteins that were first allowed to self-assemble into 10 nm high aspect ratio IFs. Scale bar is 500 nm.

of a single factor only; pairwise comparisons of treatments that differed in levels of both factors were not made. The effects of glutaraldehyde were assessed by comparing data for cross-linked fibers with their respective un-cross-linked controls using *t* tests. A multiple linear regression was conducted in R (2.14.2) to simultaneously test for the effects of fiber diameter and assembly buffer (Na vs Mg) on the breaking stress of double-drawn fibers.

RESULTS

Fibers from Formic Acid Solubilized Vimentin Protein.

Like solubilized hagfish slime thread proteins, formic acid solubilized vimentin formed a film on the surface of an electrolyte buffer, which could then be drawn into a fiber¹⁰

(Figure 2B). SV fibers were weak (breaking stress 3.4 ± 0.6 MPa) ($n = 8$), although draw processing led to considerable increases in strength (68.6 ± 19.7 MPa, $n = 7$, $p < 0.001$) and a decrease in extensibility ($p < 0.001$) (Figure 4, Table 2).

Fibers from Hydrogels of Assembled Vimentin IFs.

Vimentin filament assembly was temperature dependent, which is consistent with previous studies.¹⁷ Assembly at room temperature yielded only short unit length filaments, whereas assembly at 37 °C yielded high aspect ratio mature vimentin IFs (Figure 2C). We were able to pull fibers from hydrogels of assembled vimentin IFs that were spun in a centrifuge to concentrate the filaments (Figure 3A,B). Double-drawing these

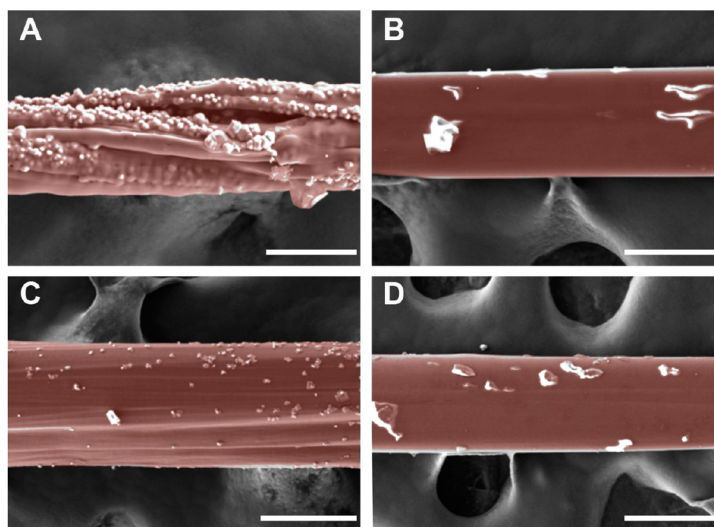


Figure 3. False color SEM images of FV fibers: (A) FV/Na/S fibers with salt crystals on surface; (B) FV/Na/D fibers; (C) FV/Mg/S fibers; (D) FV/Mg/D fibers. Top scale bars are 100 μm ; bottom are 200 μm .

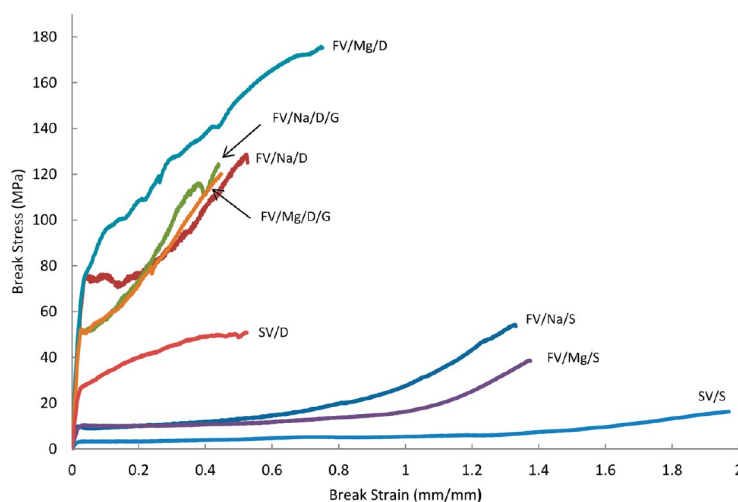


Figure 4. Representative stress–strain curves for fibers made using each of the eight vimentin assembly and processing conditions. SV/S fibers were the weakest; however draw processing led to large increases in stiffness and strength (SV/D). Draw processing of fibers made from vimentin IF hydrogels (FV/Na/S and FV/Mg/S) also led to large increases in stiffness and strength. Cross-linking with Mg^{2+} followed by draw-processing yielded the strongest and toughest fibers. Covalent cross-linking of draw-processed fibers did not improve fiber mechanics.

fibers in aqueous methanol and the inclusion of Mg^{2+} in the assembly buffer both resulted in fibers that were more uniform with a smoother surface (Figure 3C,D). Vimentin fibers made from filament hydrogels (FV) were stronger and stiffer than their single-drawn SV counterparts ($p = <0.001$). Assembly conditions (NaCl vs MgCl_2) and draw processing both had significant effects ($p = <0.001$) on FV fiber breaking strength, and the interaction between these two factors was also significant. The interactive effect was mainly a reflection of the relatively larger increase in break stress for fibers cross-linked with Mg^{2+} than those assembled and drawn in the absence of Mg^{2+} . FV/Mg/D fibers possessed the highest

Young's modulus (3.4 ± 0.3 GPa), breaking stress (173.2 ± 15.4 MPa), and strain energy (89.5 ± 18.8 MPa) of all fiber treatments tested (Table 2). Treatment of FV/Na/D and FV/Mg/D fibers with glutaraldehyde did not lead to improved material properties and in the case of FV/Mg/D fibers, it made them weaker (Table 2, Figure 4).

Structural Properties of Fibers. WAXS patterns for FV/S fibers resembled those for other structures containing aligned IFs such as mammalian hard α -keratins and native hagfish slime threads. The main features of this pattern are a 9.6 Å (Figure 5A) and 9.5 Å (Figure 5C) equatorial reflection corresponding to the spacing between adjacent coiled-coils and a 5.0 Å (Figure

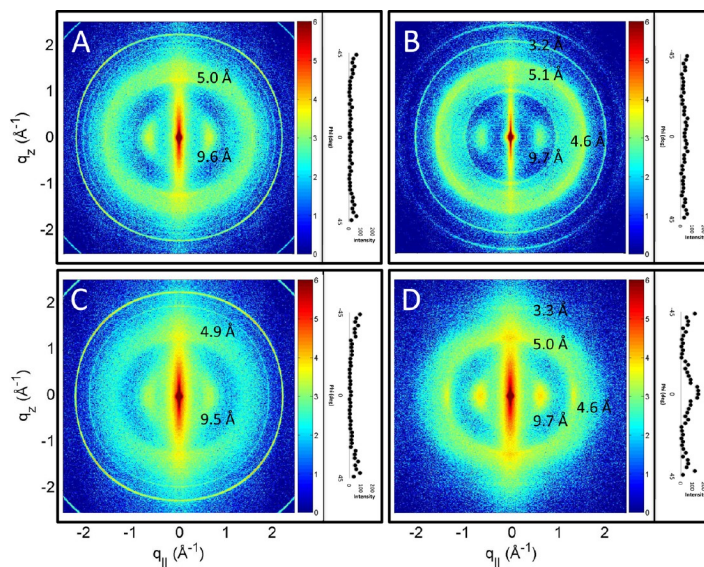


Figure 5. WAXS profiles for four kinds of FV fiber. (A) FV/Na/S and (C) FV/Mg/S fibers, which are both single-drawn, exhibited typical α -patterns, with equatorial peaks at 9.6 and 9.5 Å, respectively, and meridional peaks at 5.0 and 4.9 Å, respectively. Draw processed fibers, (B) FV/Na/D and (D) FV/Mg/D, had the same α -peaks as well as an equatorial peak at 4.6 Å, which corresponds to the spacing of protein chains within β -sheets. This peak was more prominent and well-defined in FV/Mg/D fibers than it was in FV/Na/D fibers. The insets show intensities along the azimuthal angle, ϕ , centered at the position of the 4.6 Å peak. No peak was observed in the single-drawn fibers in A and C.

SA) and 4.9 Å (Figure 5C) meridional reflection corresponding to the superhelical structure of α -helices twisting around each other within coiled-coils.²⁰ Draw processing of FV/Na/S fibers caused an increase in the sharpness of the aforementioned peaks in the resulting FV/Na/D fibers, indicating an increase in coiled-coil alignment and the subtle appearance of a 4.6 Å (Figure 5B) equatorial peak that likely denotes the spacing of protein chains within β -sheets (Figure 5). Draw processing of FV/Mg/S fibers resulted in the same coiled-coil pattern, plus a larger and sharper equatorial peak at 4.6 Å in the resulting FV/Mg/D fibers. These results suggest that it is possible to effect an α -to- β transition in macroscopic vimentin fibers, and that the process is more effective in the presence of a cross-linker such as Mg^{2+} .

DISCUSSION

Fibers from Formic Acid Solubilized Vimentin Protein. Negishi et al.¹⁰ describe a method for making films and fibers from formic acid solubilized hagfish slime thread proteins at an air–electrolyte buffer interface. Here we show that this method can be used with solubilized vimentin protein. Observing this behavior in a Type III IF suggests that it may be an attribute of all IF proteins. Draw processing of SV fibers led to a large increase in breaking stress and a decrease in extensibility, but SV/D fibers were quite weak, even after draw processing, compared with native hagfish slime threads.

Fibers from Hydrogels of Vimentin IFs. We hypothesized that SV fibers are weak because they lack the structure of the IF proteins within native slime threads and therefore are unable to form β -sheets and β -sheet crystals, which are critical to the high strength of spider silks and hagfish slime threads.^{12,21} Via centrifugation, we were able to concentrate vimentin IFs into a robust gel from which we could pull fibers.

Stress–strain curves for FV fibers had a similar three-region shape (stiff Hookean region, long plateau, strain stiffening region) to curves reported for dry hagfish slime threads,²² although the overall stresses were substantially lower (173 ± 15 MPa for FV/Mg/D fibers versus 530 ± 40 MPa for dry hagfish slime threads).²² This suggests that the different kinds of IFs have similar dry mechanics and supports the idea that hagfish slime threads are a good model for understanding IF mechanics in general. Similarly, stress–strain curves for FV/D fibers resembled curves for draw-processed native slime threads, although again, with lower overall stresses. FV/Mg/D fibers were the strongest of all eight treatments, with strength values exceeding those from the best fibers made with reconstituted hagfish slime thread protein.¹⁰

Structural Considerations. X-ray diffraction scans of fibers made from formic acid solubilized hagfish slime thread proteins revealed no WAXS peaks.¹⁰ In contrast FV/Na/S and FV/Mg/S fibers exhibited WAXS patterns similar to those seen in hard α -keratins like wool²³ and native slime threads.¹² These results demonstrate that we were able to achieve our goal of mimicking the secondary structure of proteins within hagfish slime threads. Furthermore, the improved mechanical performance of FV fibers is consistent with our hypothesis that protein structure is critical to the outstanding performance of hagfish slime threads. Draw processing of FV/Na/S and FV/Mg/S fibers led to an increase in the sharpness of WAXS peaks, indicating an increase in IF alignment, as well as the appearance of an equatorial peak at 4.6 Å, which corresponds to the spacing within β -sheets (Figure 5B,D). The mechanical stress-induced conversion of α -helices into β -sheets has been observed using WAXS in both keratin fibers^{23,24} and hagfish slime threads¹² but never in a Type III IF. Others have demonstrated using atomic force microscopy that single IFs (including vimentin) can be

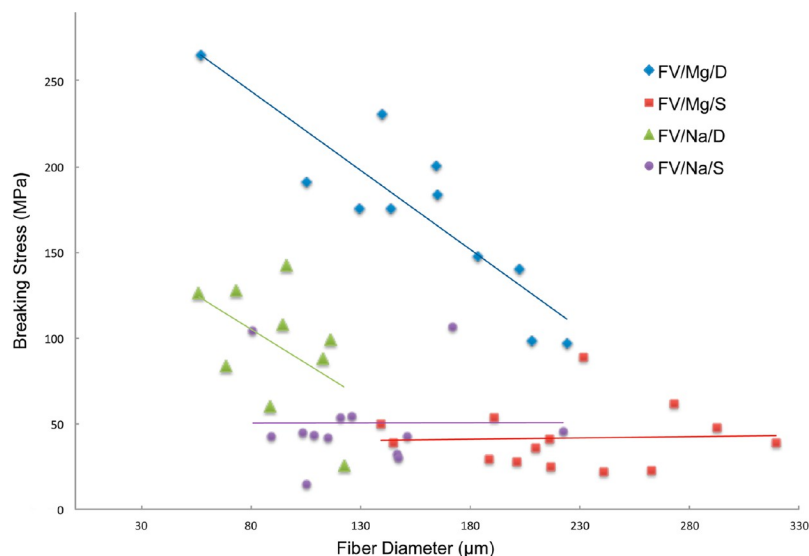


Figure 6. Fiber breaking stress plotted against diameter for four of the FV treatments. Strength was inversely proportional to diameter within FV/Na/D and FV/Mg/D fibers but had no effect on FV/Na/S and FV/Mg/S fibers. These data demonstrate that the superior mechanics of FV/Mg/D fibers are not driven by effects of Mg^{2+} on fiber diameter.

stretched to remarkable strains without breaking.^{25,26} These stretching events lead to an obvious narrowing of the IFs that likely corresponds to an α -to- β transition, although WAXS measurements were not part of these experiments. The WAXS data presented in the current study demonstrate for the first time an α -to- β transition in a Type III IF.

Negishi et al.¹⁰ found significant effects of various fiber spinning treatments on the mechanical properties of their fibers, but they also discovered that most of this variability could be understood as diameter effects. To test whether fiber diameter was the main driver of the treatment effects that we found (i.e., assembly conditions and draw processing), we plotted fiber strength against diameter for FV/Na/S, FV/Na/D, FV/Mg/S, and FV/Mg/D fibers (Figure 6). The data show that although diameter is a significant driver of mechanics within the double drawn fibers, the main effects of assembly conditions and draw processing are clearly not driven by effects of these variables on fiber diameter. This point is underscored by the fact that FV/Na/D fibers have smaller diameters than FV/Mg/D fibers ($p = 0.002$), and yet they are clearly weaker than the FV/Mg/D fibers. Fiber diameter is also important to consider when making comparisons with native hagfish slime threads. Extrapolation of the trend line for FV/Mg/D fiber strength vs diameter down to the size of native hagfish slime threads ($d \approx 1 \mu\text{m}$) yields a strength of about 317 MPa, which is almost half the strength of native threads (706 MPa).

Future Work. The data presented here demonstrate that it is possible to make robust fibers from IF hydrogels and that their mechanical properties are superior to fibers made from solubilized IF proteins. While the mechanical properties of these fibers are not yet outstanding, they are good enough to consider using them for biomedical applications such as artificial tendons (Table 3). Our data are consistent with the hypothesis that native slime threads owe their remarkable properties to the presence of β -sheets and β -sheet crystals, because vimentin fibers with the highest strength and toughness

Table 3. Summary of the Mechanical Properties of Various Protein-Based Fibers and Fibers Produced from Each of the Assembly Conditions Tested in This Study

material	break stress (MPa)	break strain (mm/mm)	Young's modulus (GPa)
amyloid protein nanofiber ²⁷	326		14
recombinant honeybee silk protein ²⁸	150	0.5	
native spider silk ²⁹	800–1400	0.2–0.3	
recombinant spider silk protein ³⁰	508	0.2	21
hagfish slime thread, dry ²	467	1.2	9
hagfish slime thread, stretched, dry ²	706	0.4	8
regenerated hagfish slime thread ¹⁰	150	0.2	4
human patellar tendon ³¹	65	0.14	0.66
FV/Na/S	51	0.8	2.1
FV/Na/D	96	0.4	2.2
FV/Na/D/G	100	0.4	2.3
FV/Mg/S	42	1.1	1.6
FV/Mg/D	173	0.6	3.4
FV/Mg/D/G	94	0.4	2.3
SV/S	3	1.5	
SV/D	69	0.4	

were also the ones with the highest β -sheet content. Despite the improvements in fiber mechanics that this study represents, there is still a substantial performance gap between artificial IF fibers and hagfish slime threads (Table 3). Future work will focus on three strategies for bridging this gap. The first is to make finer fibers, as we have shown that diameter is an important determinant of mechanics in double drawn fibers. Another strategy is to effect a more complete α -to- β transition. Draw-processed slime threads exhibit a much stronger 4.6 Å equatorial peak than FV/D fibers.¹² Creating more β -sheet

Biomacromolecules

Article

structure should further increase strength and stiffness. We will also look to the hagfish slime thread model as a source of inspiration for improving the mechanics of IF-based materials. In particular, we will continue to study the mechanisms of slime thread formation from IF proteins within the cytoplasm of hagfish gland thread cells.

CONCLUSION

In this study, we have developed a method for producing fibers made from self-assembled vimentin IFs. We have also shown for the first time that 10 nm filaments assembled *in vitro* undergo an $\alpha \rightarrow \beta$ transition when strained, suggesting that 10 nm IFs in cells could potentially undergo this same transition. From all of the assembly conditions, fibers that were cross-linked with Mg^{2+} exhibited the strongest mechanical properties. Overall, this study, using novel methods to produce fibers from hydrogels of 10 nm IFs, opens up new possibilities for the production of protein-based fibers. The production of high-performance protein polymers from such fibers has the potential to decrease our reliance on petroleum-based synthetics.

AUTHOR INFORMATION

Corresponding Authors

*Tel: 519-824-4120 (ext. 58786). Fax: 519-767-1656. E-mail: tgillis@uoguelph.ca.

*Tel: 519-824-4120 (ext. 56418). Fax: 519-767-1656. E-mail: dfudge@uoguelph.ca.

Author Contributions

§Co-senior authors.

Notes

The authors declare no competing financial interest.

ACKNOWLEDGMENTS

We thank Dr. Harald Herrmann for the pDSS plasmid and Laurent Kreplak for assistance with vimentin assembly. Thanks also to Bob Harris of the Electron Microscopy Unit at the University of Guelph and Jean-Luc Stiles for help with statistics. This work was supported by NSERC Discovery and Accelerator grants and Ontario Early Researcher Awards to DF, NSERC Discovery, Canadian Foundation for Innovation (CFI), Ontario Ministry of Economical Development and Innovation, and Ontario Early Researcher Awards to M.C.R., and NSERC Discovery and Research Tools and Instrumentation grants to T.G.

REFERENCES

- (1) Shao, Z.; Vollrath, F.; Yang, Y.; Thøgersen, H. C. *Macromolecules* **2003**, *36*, 1157–1161.
- (2) Fudge, D. S.; Hillis, S.; Levy, N.; Gosline, J. M. *Bioinspiration Biomimetics* **2010**, *5*, 1–8.
- (3) Newby, W. W. *J. Morphol.* **1946**, *78*, 397–409.
- (4) Fernholm, B. *Acta Zool.* **1981**, *62*, 137–145.
- (5) Spitzer, R. H.; Downing, S. W.; Koch, E. A.; Salo, W. L.; Saidel, L. *J. Cell Biol.* **1984**, *98*, 670–677.
- (6) Downing, S. W.; Spitzer, R. H.; Koch, E. A.; Salo, W. L. *J. Cell Biol.* **1984**, *98*, 653–669.
- (7) Fudge, D. S.; Levy, N.; Chiu, S.; Gosline, J. M. *J. Exp. Biol.* **2005**, *208*, 4613–4625.
- (8) Koch, E. A.; Spitzer, R. H.; Pithawalla, R. B.; Parry, D. A. *J. Cell Sci.* **1994**, *107*, 3133–3144.
- (9) Koch, E. A.; Spitzer, R. H.; Pithawalla, R. B.; Castillos, F. A., III; Parry, D. A. *Int. J. Biol. Macromol.* **1995**, *17*, 282–292.
- (10) Negishi, A.; Armstrong, C. L.; Kreplak, L.; Rheinstadter, M. C.; Lim, L. T.; Gillis, T. E.; Fudge, D. S. *Biomacromolecules* **2012**, *13*, 3475–3482.
- (11) Downing, S. W.; Spitzer, R. H.; Koch, E. A.; Salo, W. L. *J. Cell Biol.* **1984**, *98*, 653–669.
- (12) Fudge, D. S.; Gardner, K. H.; Forsyth, V. T.; Riekel, C.; Gosline, J. M. *Biophys. J.* **2003**, *85*, 2015–2027.
- (13) Spitzer, R. H.; Koch, E. A.; Downing, S. W. *Cell Motil. Cytoskeleton* **1988**, *11*, 31–45.
- (14) Qin, Z.; Kreplak, L.; Buehler, M. J. *PLoS One* **2009**, *4*, No. e7294.
- (15) Herrmann, H.; Häner, M.; Brettel, M.; Müller, S. A.; Goldie, K. N.; Fedtke, B.; Lustig, A.; Franke, W. W.; Aebi, U. *J. Mol. Biol.* **1996**, *264*, 933–953.
- (16) Bujard, H.; Gentz, R.; Lanzer, M.; Stueber, D.; Mueller, M.; Ibrahim, I.; Hauptle, M. T.; Dobberstein, B. *Methods Enzymol.* **1987**, *155*, 416–433.
- (17) Herrmann, H.; Kreplak, L.; Aebi, U. *Methods Cell Biol.* **2004**, *78*, 3–24.
- (18) Herrmann, H.; Aebi, U. *Annu. Rev. Biochem.* **2004**, *73*, 749–789.
- (19) Lin, Y.-C.; Broedersz, C. P.; Rowat, A. C.; Wedig, T.; Herrmann, H.; MacKintosh, F. C.; Weitz, D. A. *J. Mol. Biol.* **2010**, *399*, 637–644.
- (20) Crick, F. H. C. *Nature* **1952**, *170*, 882–883.
- (21) Gosline, J. M.; DeMont, M. E.; Denny, M. W. *Endeavour* **1986**, *10*, 37–43.
- (22) Fudge, D. S.; Gosline, J. M. *Proc. R. Soc. London, Ser. B* **2004**, *271*, 291–299.
- (23) Kreplak, L.; Doucet, J.; Dumas, P.; Briki, F. *Biophys. J.* **2004**, *87*, 640–647.
- (24) Kreplak, L.; Franbourg, A.; Briki, F.; Leroy, F.; Dalle, D.; Doucet, J. *Biophys. J.* **2002**, *82*, 2265–2274.
- (25) Guzmán, C.; Jeney, S.; Kreplak, L.; Kasas, S.; Kulik, A. J.; Aebi, U.; Forró, L. *J. Mol. Biol.* **2006**, *360*, 623–630.
- (26) Kreplak, L.; Herrmann, H.; Aebi, U. *Biophys. J.* **2008**, *94*, 2790–2799.
- (27) Meier, C.; Welland, M. E. *Biomacromolecules* **2011**, *12*, 3453–3459.
- (28) Weisman, S.; Haritos, V. S.; Church, J. S.; Huson, M. G.; Mudie, S. T.; Rodgers, A. J. W.; Dumsdat, G. J.; Sutherland, T. D. *Biomaterials* **2010**, *31*, 2695–2700.
- (29) Shao, Z.; Vollrath, F. *Polymer* **1999**, *40*, 1799–1806.
- (30) Xia, X. X.; Qian, Z. G.; Ki, C. S.; Park, Y. H.; Kaplan, D. L.; Lee, S. Y. *Proc. Natl. Acad. Sci. U.S.A.* **2010**, *107*, 14059–14063.
- (31) Johnson, G. A.; Tramaglino, D. M.; Levine, R. E.; Ohno, K.; Choi, N. Y.; Woo, S. L. *J. Orthop. Res.* **1994**, *12*, 796–803.

5.2 Paper II: Hierarchical, Self-Similar Structure in Native Squid Pen

Fei-Chi Yang, Robert D. Peters, Hannah Dies, Maikel C. Rheinstädter. “*Hierarchical, Self-Similar Structure in Native Squid Pen*”, *Soft Matter*, 2014, 10, 5541–5549

5.2.1 Preface to Paper II

One night as I was preparing my squid for dinner, the squid pen left on the chopping board caught my attention. Since the previous project, I have started to appreciate these wonderful biomaterials made by nature and thought that I should probably do a X-ray diffraction experiment just for fun. The X-ray data turned out to be a surprise because it had very strong and distinct signals and high order of anisotropy. That was the starting point of the project.

In this project, we developed the integration macro in Matlab and further polished the analysis technique when coping with natural samples that are inherently disordered. We optimized the intensity and the resolution by optimizing the slits. We combined microscopy, atomic force microscopy, and X-ray diffraction to investigate the hierarchical structures of squid pens. The α coiled-coil pattern was recognized from the previous project and the diffraction signals from the β -chitin was identified. It is worth noting that the faint yellow diagonal signal from the α -helices are present here because the same pattern was usually seen in the frozen DNA sample where the thermal fluctuations are suppressed.

Author Contributions

- *Experiment Design:* Maikel C. Rheinstädter and **Fei-Chi Yang**
- *Sample Preparation:* **Fei-Chi Yang** and Maikel C. Rheinstädter
- *Experiment Performing:* **Fei-Chi Yang**, Robert D. Peters, and Maikel C. Rheinstädter
- *Data Analysis:* **Fei-Chi Yang** and Hannah Dies
- *Manuscript Writing:* Maikel C. Rheinstädter, **Fei-Chi Yang**, Robert D. Peters, and Hannah Dies



Hierarchical, self-similar structure in native squid pen

Cite this: *Soft Matter*, 2014, 10, 5541Fei-Chi Yang,^a Robert D. Peters,^a Hannah Dies^a and Maikel C. Rheinstädter^{*ab}

The structure of native squid pen (gladius) was investigated in two different species on different length scales. By combining microscopy, atomic force microscopy (AFM), and X-ray diffraction, the experiments probed length scales from millimetres down to nanometres. The gladius showed a hierarchical, self-similar structure in the optical experiments with fibres of different size oriented along the long axis of the gladius. The fibre-like structure was reproduced at the nanoscale in AFM measurements and fibres with diameters of 500 μm , 100 μm , 10 μm , 2 μm and 0.2 μm were observed. Their molecular structure was determined using X-ray diffraction. In the squid gladius, the chitin molecules are known to form nanocrystallites of monoclinic lattice symmetry wrapped in a protein layer, resulting in β -chitin nano-fibrils. Signals corresponding to the α -coil protein phase and β -chitin crystallites were observed in the X-ray experiments and their orientation with respect to the fibre-axis was determined. The size of a nano-fibril was estimated from the X-ray experiments to be about 150 \times 300 \AA . About 100 of these nano-fibrils are needed to form a 0.2 μm thick micro-fibre. We found that the molecular structure is highly anisotropic with $\sim 90\%$ of the α -coils and β -chitin crystallites oriented along the fibre-axis, indicating a strong correlation between the macroscale structure and molecular orientation.

Received 7th February 2014
Accepted 16th May 2014

DOI: 10.1039/c4sm00301b

www.rsc.org/softmatter

1. Introduction

Chitin is a polymer of un-branched chains of β -(1-4)-linked 2-acetamido-2-deoxy-D-glucose (*N*-acetyl-D-glucosamine).¹⁻¹⁰ It is widely distributed in nature, especially in marine invertebrates, insects, fungi and yeast.^{11,12} Chitin occurs naturally in the crystalline state and X-ray diffraction studies of diverse supporting structures indicate three different types of crystallographic patterns among chitin.¹²⁻¹⁴ α -Chitin, whose chains are arranged in an antiparallel direction with strong intermolecular hydrogen bonding, is found in Crustacea.¹⁵ For γ -chitin, found in the thick cuticle of the stomach of squid genus *Loligo*, the central chain is arranged in an antiparallel direction between the two adjacent ones.^{13,16} In association with proteins, chitin from squid gladius forms β -chitin, a monoclinic structure where its chains are arranged in a parallel direction with relatively weak intermolecular interactions.¹⁷⁻¹⁹

The gladius is a feather-shaped internal structure that supports the squid's mantle and serves as a site for muscle attachment, as sketched in Fig. 1a. Upon examination, the gladius shows a corrugated, fibre-like structure with channels running along the long axis of the squid. In addition, smaller fibres are observed on the surface of the larger, primary fibres. We combined light microscopy, atomic force microscopy (AFM),

and X-ray diffraction to investigate the gladius' structure at different length scales, ranging from millimetres down to nanometres, as depicted in Fig. 1b. Hierarchical, self-similar

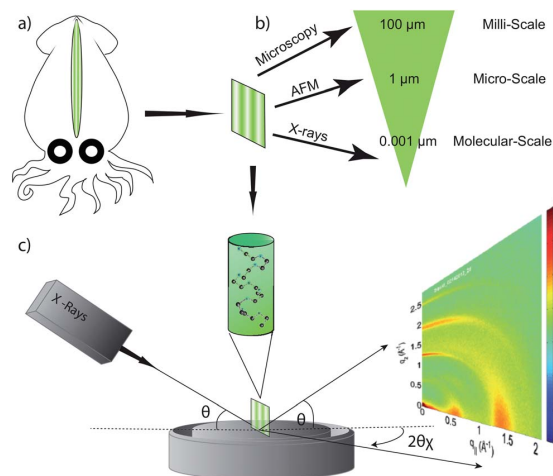


Fig. 1 (a) The pen (gladius) is a feather-shaped internal structure that supports the squid's mantle and serves as a site for muscle attachment. (b) The structure of the gladius was studied using three different techniques: light microscopy, atomic force microscopy, and X-ray diffraction, covering length scales from millimetres to the molecular level. (c) By aligning the gladius, the molecular structure along the fibres and perpendicular to the fibres was studied using X-ray diffraction.

^aDepartment of Physics and Astronomy, McMaster University, Hamilton, ON, Canada. E-mail: rheinstadter@mcmaster.ca

^bCanadian Neutron Beam Centre, Chalk River, ON, Canada

fibre-like structures were observed at all length scales down to the molecular level. We found that $\sim 90\%$ of the α -helical coils and monoclinic β -chitin crystallites were oriented parallel to the fibres, indicating a correlation between the structures observed at nano-, micro- and macro-scales, and molecular orientation.

2. Materials and methods

2.1. Sample preparation

Fresh squid gladii were obtained from the local fish market in Tainan, Taiwan, and in Toronto, Canada. The gladii were washed thoroughly with tap water to remove soluble organics and adherent protein, and dried at room temperature in a desiccator in a magnesium nitrate atmosphere ($\text{Mg}(\text{NO}_3)_2$) at 25°C at $52.9 \pm 0.22\%$ relative humidity (RH). The gladii were found to deform during the drying process. In order to obtain flat pieces, the gladius was dried between two aluminum sheets. The squid gladii were cut into $\sim 20\text{ mm} \times 10\text{ mm}$ pieces, and optimized for the microscopy, AFM and X-ray experiments. All samples were stored in a desiccator at $52.9 \pm 0.22\%$ RH. Details of the samples are listed in Table 1.

We note that the freshly cut gladius started to dry quickly in air, such that initial experiments did not give conclusive results as the structure kept changing during the time of the experiments. The gladii also changed when stored or investigated in ultrapure water, buffer or in salted ultrapure water due to the concentration differences. The gladii were, therefore, extracted and dried quickly in a $\text{Mg}(\text{NO}_3)_2$ atmosphere to best preserve their structure. The structure of the gladii, the surface structure as determined by AFM, and the bulk structure as determined by X-ray diffraction could then be stabilized over several days.

The reason for the low number of species ($N = 2$) is the availability of samples, and in particular, the identification of the correct species. Several squids were acquired for this project. However, the authentication of squid species is an

ongoing field of research (see ref. 20). The two specimens in our study were selected based on an unambiguous identification. We note that even specimens acquired through the same provider often belong to different families. We, therefore, limit the discussion to these two specimens.

2.2. Inverted light microscopy

Optical microscopy in this study was performed using an Olympus BX51 microscope. Samples were placed onto silicon wafers and imaged in dark-field reflection mode with a CCD camera (QIClick, QImaging), which provided high resolution images (1392×1040 pixels) for subsequent image analysis. In dark-field microscopy, the unscattered beam is excluded from the image by illuminating the sample with light that when reflected will not be collected by the objective lens. Using this technique results in increased contrast for the features in the squid gladius. A $50\times$ magnification objective (UMPlanFI, Olympus) was used to obtain images with a resolution of 130 nm per pixel. Additional images with lower resolution were taken using a Nikon P520 digital camera in high-resolution macro setting mode.

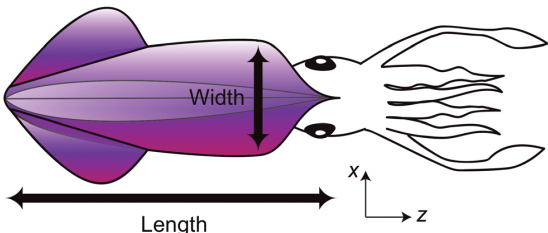
2.3. Atomic force microscopy

AFM was performed in constant amplitude tapping mode using a commercial AFM (Veeco Caliber, USA). The AFM was placed on an anti-vibration table on top of a granite block to provide isolation from background noise. Cantilevers with a spring constant of $\sim 48\text{ N m}^{-1}$ and a resonance frequency of 190 kHz were used for this study. Topography and tapping amplitude data were recorded simultaneously for samples mounted on Si wafers. Samples were measured at 25°C and at a relative humidity of $52.9 \pm 0.22\%$. The humidity was controlled by sealing the AFM heads in a container with a saturated salt solution of magnesium nitrate ($\text{Mg}(\text{NO}_3)_2$) at 25°C . Topography imaging provided a 2-dimensional map of film height in the region of interest. Similarly, tapping amplitude data offer the derivative of the topography, indicating where film height changes rapidly, clearly distinguishing the edges of squid gladius fibres.

2.4. X-ray diffraction experiment

X-ray diffraction data were obtained using the Biological Large Angle Diffraction Experiment (BLADE) in the Laboratory for Membrane and Protein Dynamics at McMaster University. BLADE uses a 9 kW (45 kV , 200 mA) $\text{CuK}\alpha$ Rigaku Smartlab rotating anode at a wavelength of 1.5418 \AA . Focussing multi-layer optics provides a high intensity parallel beam with monochromatic X-ray intensities up to 10^{10} counts per s per mm^2 . A sketch of the scattering geometry is shown in Fig. 1c. By aligning the gladius in the X-ray diffractometer, the molecular structure along the fibre direction and perpendicular to the fibres could be determined. We refer to these components of the total scattering vector, Q , as q_z and q_{\parallel} , respectively, in the following. The result of the X-ray experiment is a 2-dimensional intensity map of a large area of the reciprocal space of $-2.5\text{ \AA}^{-1} < q_z < 2.5\text{ \AA}^{-1}$ and $-2\text{ \AA}^{-1} < q_{\parallel} < 2\text{ \AA}^{-1}$. The corresponding

Table 1 Dimensions of the two squid specimens studied. The gladius was extracted and cut into $\sim 20\text{ mm} \times 10\text{ mm}$ pieces, and optimized for the microscopy, AFM and X-ray experiments. All samples were stored in a desiccator at $52.9 \pm 0.22\%$ RH and $T = 25^\circ\text{C}$



Sample	Species	Length \times width	Gladius
1	<i>Sepioteuthis lessoniana</i>	170 mm \times 150 mm	180 mm \times 20 mm
2	<i>Uroteuthis chinensis</i>	255 mm \times 60 mm	240 mm \times 40 mm

real-space length scales are determined by $d = 2\pi/|Q|$ and cover length scales from about 2.5 to 60 Å, incorporating typical molecular dimensions and distances. The squid gladius samples were kept in a temperature- and humidity-controlled chamber, the so-called humidity chamber, during the measurements. Data were collected at $T = 25 \text{ }^\circ\text{C}$ and $52.9 \pm 0.22\%$ relative humidity by exposing them to a saturated salt solution of magnesium nitrate.

3. Results

3.1. Topology from visual inspection, microscopy and atomic force microscopy

The gladii show a corrugated, rippled structure when examined by the eye, as depicted in Fig. 2a. The observed fibres were well oriented running along the long axis of the squid, denoted as the z -axis in Table 1. Smaller ripples were observed on the surface of the larger, primary ripples. The high resolution microscopy image in Fig. 2b shows a similar picture: large ripples running along the z -axis coexisting with smaller ripples. Parallel ripples and channels were also observed at sub-micrometre resolution in the AFM images in Fig. 2c and d.

The sizes of the different fibres, as determined from the images in Fig. 2, are listed in Table 2. The largest fibres in Fig. 2a have a diameter of 500 µm; smaller fibres with 100 µm were observed on the surface of the larger fibres. Fibres with diameters of 100 µm, 10 µm and 2 µm were observed in the dark-field microscopy images in Fig. 2b. 2 µm and 0.2 µm fibres were visible in the high-resolution AFM images in Fig. 2c and d.

The images in Fig. 2 cover three orders of magnitude at the length scale and show a hierarchical, self-similar topology of the squid gladius. With the help of X-ray diffraction measurements, we can extend the accessible length scale to the molecular scale.

3.2. Molecular structure from X-ray diffraction

Fig. 3 depicts 2-dimensional X-ray data of samples 1 and 2. The displayed range was determined to cover the length scales of the features of interest in preliminary experiments. The scattered intensity in a small rectangle located at $q_z \sim 2.25 \text{ \AA}^{-1}$ and $q_{||} \sim 2 \text{ \AA}^{-1}$, where no diffraction maxima occurred, was used as background and subtracted from the data. The data in Fig. 3a and b show a distinct non-isotropic distribution of the diffracted intensity with pronounced and well defined intensities along the q_z and $q_{||}$ axes. Sample 1 was found to diffract less well overall, as checked with several pieces from different parts of the gladius, however the diffraction patterns of samples 1 and 2 qualitatively agree very well and show the same features.

For a quantitative analysis, the 2-dimensional data were extracted and analyzed separately along the q_z and $q_{||}$ axis. The results are shown in Fig. 4a and b. To capture all diffracted intensity of a given peak, the 2-dimensional data were integrated radially over 25° from the equator of $q_{||}$ and over 25° from the meridian of q_z , as depicted in the insets of Fig. 4a and b. Several intensity maxima in the 1-dimensional data were observed along both the q_z and $q_{||}$ axis. Lorentzian peak profiles

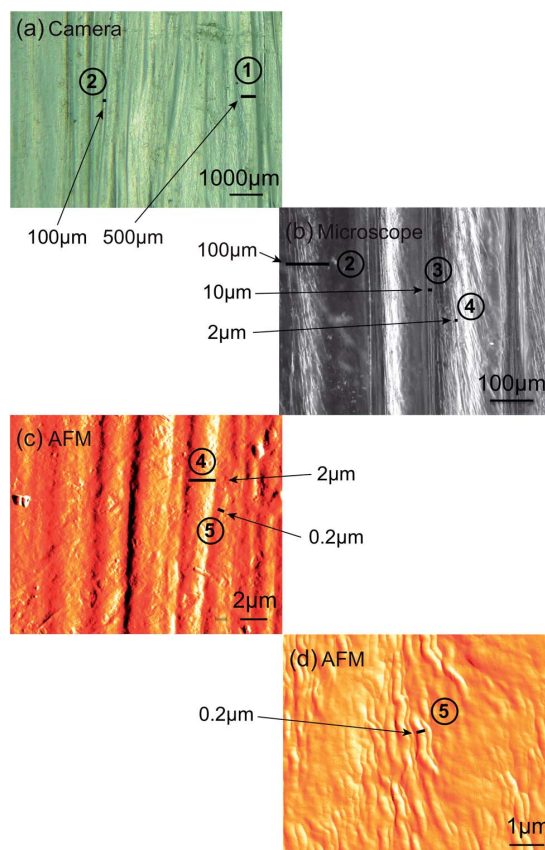


Fig. 2 The surface structure of the native squid gladius was studied using different techniques. (a) Using a high resolution digital camera. (b) A light microscope in dark-field reflection mode and (c) an AFM tapping amplitude image. (d) An AFM image of the layer inside the squid gladius. The images cover length scales from millimetres down to about 100 nanometres. Self-similar, fibre-like hierarchical structures can be observed at all length scales. The observed fibre sizes are listed in Table 2.

Table 2 Observed fibre sizes from the images in Fig. 2. Fibres from 500 µm (①) to 0.2 µm (⑤) were observed with a digital camera, a microscope, and an atomic force microscope

	Digital camera	Microscope	AFM	Observed fibre size
①	×			500 µm
②	×	×		100 µm
③		×		10 µm
④		×	×	2 µm
⑤			×	0.2 µm

were fitted to and the corresponding correlation peaks labeled $1_{||}$, $2_{||}$, $3_{||}$, $4_{||}$ and 1_z , 2_z , 3_z , 4_z , respectively.

The angular distribution of the diffracted intensities was determined by integrating over the azimuthal angle ϕ . The corresponding ϕ -profiles of the in-plane reflections $2_{||}$ and

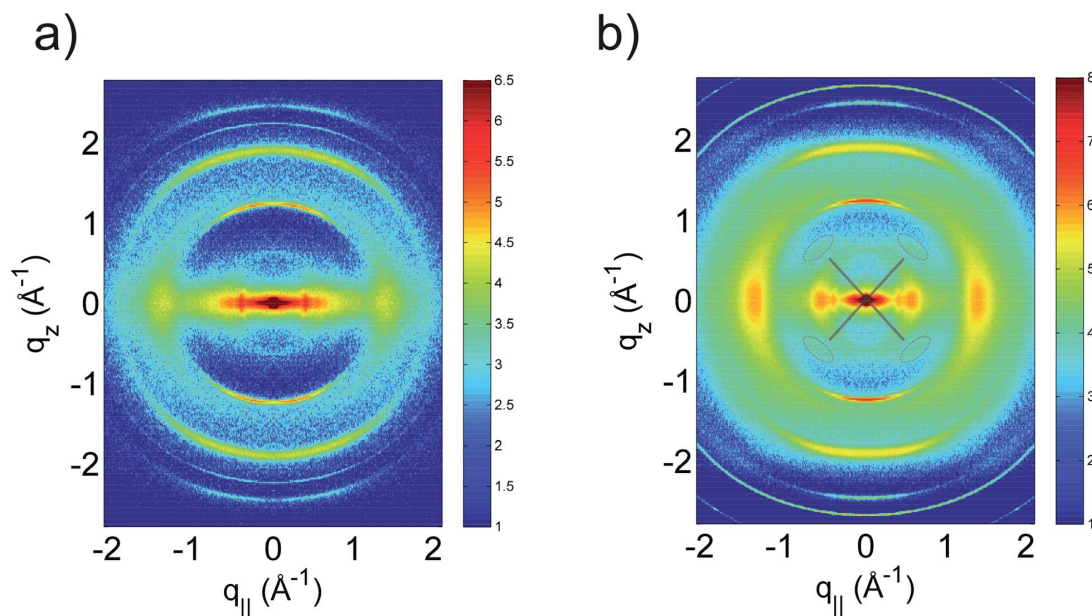


Fig. 3 Two-dimensional X-ray data with background subtracted for Samples 1 (a) and 2 (b). Pronounced diffraction peaks can be observed along both the q_z - and $q_{||}$ -axis. The fact that intensity maxima mainly occurred on one of the axes was indicative that the corresponding molecular structures are anisotropic and highly aligned with respect to z and x .

($3_{||} + 4_{||}$) are shown in Fig. 5a and b. The in-plane peaks showed a broad distribution, which was well fit by a single Lorentzian peak profile with a ϕ -width (HWHM) of $\sim 17^\circ$.

Because of this large angular distribution of the diffracted intensities around the equator and meridian, features could appear simultaneously in both directions in the data in Fig. 4a

and b. The peak patterns were, therefore, fitted simultaneously in q_z and $q_{||}$ using the following procedure: in the first round, the main peaks (marked as $1_{||}$, $2_{||}$, $3_{||}$, and $4_{||}$ in Fig. 4a) were fitted in $q_{||}$. The corresponding peaks were then included in the fitting of the q_z data in Fig. 4b. The position and width were kept fixed and only the amplitude was varied. The fitted out-of-plane

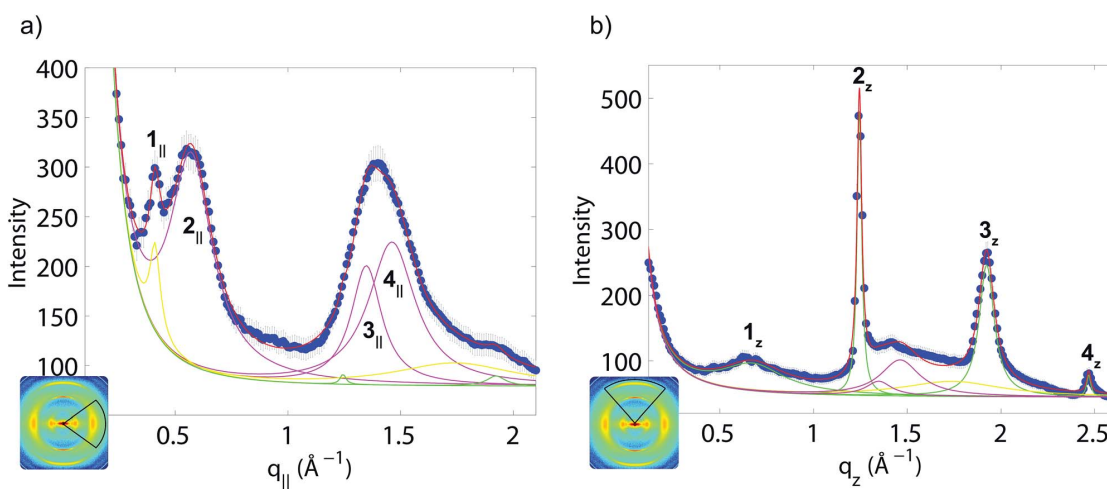


Fig. 4 The 2-dimensional data in Fig. 3 were cut along the $q_{||}$ (a) and q_z -axis (b). To capture all diffracted intensity, the 2-dimensional data were integrated radially over 25° from the equator for $q_{||}$ and over 25° from the meridian for q_z , as depicted in the insets. Solid lines are fits using Lorentzian peak profiles. In-plane peaks are plotted in magenta, and peaks along q_z in green. Both directions were fitted simultaneously. The fitted peak positions and widths (given as HWHM) are listed in Tables 3 and 4, and were assigned to an α -helical and a monoclinic structure.

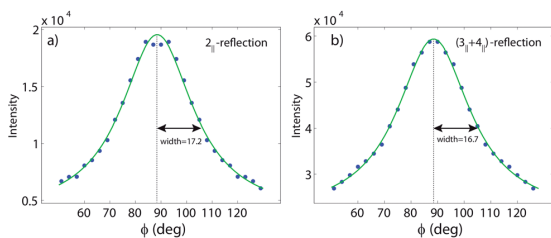


Fig. 5 The angular distributions of the diffracted intensity of the in-plane peaks (a): $2_{||}$ and (b): $(3_{||} + 4_{||})$ could be fitted by single Lorentzians with a HWHM of $\sim 17^\circ$.

Bragg peaks 1_z , 2_z , 3_z and 4_z were then included in fitting the $q_{||}$ -axis data. This cycle was repeated several times until good agreement between the fit and the data was obtained.

The peaks could be assigned to in-plane and out-of-plane features using this procedure, as listed in Tables 3 (in-plane) and 4 (along the fibre-axis). We can at this point not assign the yellow contribution in Fig. 4a and b, which had an identical intensity in both directions, indicative of an amorphous structure in the native gladius with a length scale of $\sim 3.8 \text{ \AA}$. Peak $1_{||}$ stems from the Kapton windows of the X-ray humidity chamber and was, therefore, not included in the structure determination. We note that the Kapton does not scatter isotropically, which would be observed as a powder ring in the 2-dimensional diffraction data. The Kapton foils used for the X-ray windows are rolled to a thickness of 13 \mu m . This process leads to a preferred orientation in the polyimide film and to the observed anisotropy. The peaks in Tables 3 and 4 can be assigned to α -helical and monoclinic structures, as will be explained in the next section.

3.3. Chitin and protein structures in the native squid gladius

β -Chitin has been found to form in the squid gladius in association with proteins.^{12,19,21,22} The chitin molecules were found to organize in chitin nano-crystals, which are wrapped in a protein layer to form nano-fibrils. These fibrils eventually organize into larger fibres. When extracting β -chitin from the squid gladius, yields between ~ 25 and 45% were reported.^{19,22} The protein component after chemical extraction is typically $\sim 75\%$. The X-ray experiments were sensitive to the corresponding protein and chitin structures, namely the α -helical protein phase and the monoclinic β -chitin crystallites.

3.4. Scattering from α -coils

The diffraction pattern of an ideal helix was first written down by Pauling and Corey.²³ The periodic structures of the helix along the diagonal directions are the well-known helix peaks, which typically appear as a cross in X-ray diffraction data from a crystalline, well-ordered specimen.^{24–26} The first order helix peak is observed as a weak feature in the 2-dimensional data in Fig. 3, as marked by the circle. Higher order peaks and side oscillations are usually observed in a crystalline specimen measured at liquid nitrogen temperature. They are, however, most likely suppressed by thermal positional fluctuations and the intrinsic disorder in native samples at elevated temperatures. The $q_{||}$ and q_z positions of the helical peak map to the distance of the pitch, P_h , of the helices and the radius, R_h , in real space by: $q_{||} = 5\pi/(8R_h)$ and $q_z = 2\pi/P_h$. The position of the (101) peak of the helices are found to be $q_{||} = 0.60 \text{ \AA}^{-1}$ and $q_z = 0.60 \text{ \AA}^{-1}$ for Sample 1, and $q_{||} = 0.53 \text{ \AA}^{-1}$ and $q_z = 0.80 \text{ \AA}^{-1}$ for Sample 2. The values for R_h and P_h for both samples were calculated using the above equations and are listed in Table 5.

The proteins in the squid gladius are known to organize into bundles of proteins, whose structure is dominated by α -helical

Table 3 Fitted peak positions and widths (as HWHM) for the parallel direction in Fig. 4a. Errors given are the fitting errors. The corresponding correlation peaks were assigned to α -helical and monoclinic structures, as explained in the text

Sample 1			Sample 2			α -Coil	Monoclinic
Amplitude (counts)	Position (\AA^{-1})	Width (\AA^{-1})	Amplitude (counts)	Position (\AA^{-1})	Width (\AA^{-1})	hkl	hkl
$1_{ }$	63 ± 3	0.409 ± 0.001	0.026 ± 0.002	215 ± 3	0.41 ± 0.002	0.03 ± 0.003	Kapton window
$2_{ }$	33 ± 2	0.58 ± 0.01	0.21 ± 0.02	215 ± 3	0.571 ± 0.002	0.115 ± 0.004	(100) —
$3_{ }$	15 ± 12	1.36 ± 0.02	0.09 ± 0.05	120 ± 37	1.348 ± 0.009	0.08 ± 0.02	— (020)
$4_{ }$	20 ± 10	1.48 ± 0.06	0.16 ± 0.05	144 ± 38	1.46 ± 0.02	0.13 ± 0.03	— (110)

Table 4 Fitted peak positions and widths (as HWHM) for the perpendicular direction in Fig. 4b. Errors given are the fitting errors. The corresponding correlation peaks were assigned to α -helical and monoclinic structures

Sample 1			Sample 2			α -Coil	Monoclinic
Amplitude (counts)	Position (\AA^{-1})	Width (\AA^{-1})	Amplitude (counts)	Position (\AA^{-1})	Width (\AA^{-1})	hkl	hkl
1_z	9.6 ± 0.6	0.619 ± 0.007	0.12 ± 0.01	42 ± 3	0.68 ± 0.01	0.21 ± 0.02	— (001)
2_z	122 ± 3	1.2439 ± 0.0004	0.0166 ± 0.0005	433 ± 18	1.2447 ± 0.0005	0.0149 ± 0.0007	(001) (002)
3_z	66 ± 1	1.9098 ± 0.0009	0.0550 ± 0.0001	200 ± 7	1.924 ± 0.002	0.049 ± 0.002	— (003)
4_z	165 ± 1	2.473 ± 0.002	0.044 ± 0.004	33 ± 8	2.469 ± 0.003	0.014 ± 0.005	— (004)

Table 5 Structural parameters of the α -helical coil and monoclinic β -chitin crystallites, as determined from the peak positions in Tables 3 and 4. The degree of orientation of the coils and crystallites with respect to the fibre-axis in Fig. 2 was determined by Herman's orientation function. The dimension of the two structures was estimated using Scherrer's equation. The diameter and length of the protein/chitin nano-fibrils were estimated from the protein layer thickness and the chitin crystallite size, as described in the text

Sample	α -Coils				Monoclinic β -chitin					Nano-fibril		
	R_h (Å)	P_h (Å)	Degree of orientation (f_z)	Protein layer thickness (Å)	a (Å)	b (Å)	c (Å)	γ (°)	Degree of orientation (f_b)	Crystallite size (Å)	Diameter (Å)	Length (Å)
1	3.70	7.85	92.0%	28	5.15	9.32	10.15	97.5	92.3%	65 × 163	122	219
2	3.27	10.47	86.9%	51	5.24	9.40	9.24	97.5	87.5%	74 × 222	176	324

coiled-coils. The main features of this pattern are a ~ 10 Å (corresponding to $q_{\parallel} \sim 0.6 \text{ \AA}^{-1}$) equatorial reflection corresponding to the spacing between adjacent coiled-coils and a ~ 5.0 Å meridional reflection (corresponding to $q_z \sim 1.25 \text{ \AA}^{-1}$) corresponding to the superhelical structure of α -helices twisted around each other within coiled-coils.^{27–29} Reflections 2_{\parallel} and 2_z in Tables 3 and 4 were, therefore, assigned to α -coils. We note that these peaks are related to generic α -helical coil structures of monomeric proteins, and not specific to a certain type of protein. Because helix and coiled-coil peaks were found in the diffraction data, we argue that these peaks belong to a protein phase rather than, for instance, α -chitin.

3.5. Scattering from β -chitin

Crystalline monoclinic β -chitin was reported to order in the monoclinic space group $P2_1$ with unit cell dimensions $a = 4.85$ Å, $b = 9.26$ Å, $c = 10.38$ Å, and $\beta = 97.5^\circ$ by Blackwell, Parker and Rudall.^{17,18} The corresponding q_{hkl} -positions for a monoclinic symmetry are given by:³⁰

$$q_{hkl}^2 = \frac{4\pi^2}{\sin^2 \gamma} \left(\frac{h^2}{a^2} + \frac{k^2}{b^2} + \frac{l^2 \sin^2 \gamma}{c^2} - \frac{2hk \cos \gamma}{ab} \right) \quad (1)$$

The positions of the (020), (110), (001), (002), (003), and (004) reflections agree well with the reported monoclinic β -chitin structure. One thing worth noting is that the (001) and (003) reflections, which should be systematically absent in this space group, were observed in the data. This effect has been frequently observed in soft materials and is a consequence of the inherent disorder in these systems.^{31,32} Extinction rules may be lifted when soft structures deviate from their nominal crystal structure to form a space filling pattern.

The lattice parameters were determined from the $q_{z/\parallel}$ -values in Tables 3 and 4. The monoclinic angle, γ , could not be determined from our measurements, as only powder averages were observed in the ab -plane (perpendicular to the fibre-axis). As a result, the value of $\gamma = 97.5^\circ$ was used from the original papers by Blackwell.^{17,18} The lattice parameter c was determined from the averaged positions of the (001) reflection:

$$q_{(001)}^2 = \left(\frac{4\pi^2 l^2}{c^2} \right) \quad (2)$$

to be $c = 10.15$ Å. Parameters a and b were determined from the positions of the (020) and (110) peaks along the q_{\parallel} -axis:

$$q_{(020)}^2 = \frac{4\pi^2}{\sin^2 \gamma} \left(\frac{2^2}{b^2} \right) \quad (3)$$

and

$$q_{(110)}^2 = \frac{4\pi^2}{\sin^2 \gamma} \left(\frac{1^2}{a^2} + \frac{1^2}{b^2} - \frac{2 \cos \gamma}{ab} \right) \quad (4)$$

to $a = 9.32$ Å and $b = 5.15$ Å. The monoclinic unit cell parameters for the two samples are listed in Table 4.

We note that the 2_z reflection in Fig. 4b is significantly stronger than the other reflections. Based on the models above, this peak has contributions from both the coiled-coils and the monoclinic lattice.

4. Discussion

A hierarchical chitin structure was found in crustacean exoskeleton,^{33,34} where fibres consisting of α -chitin crystals organize into a planar woven and periodically branched network in the so-called twisted plywood structure of high stiffness. Concerning β -chitin, a periodic structure in the gladius of the squid *Loligo vulgaris* was observed by Hunt and Sherief³⁵ using electron microscopy and was related to the formation of chitin-protein complexes. Corresponding protein-chitin structures were reported decades ago by Blackwell, Germinario and Weih,²¹ where the proteins formed a helical sheath around chitin fibrils. A lamellar structure has also been reported more recently by Lavall, Assis and Campana-Filho.²² De-proteinated, de-mineralized and de-acetylated gladii were used for these studies. We studied the molecular structure and organization in the native state of the gladius.

We observed a hierarchical, self-similar structure in the gladius of two different species. The surface of the gladii showed a fibre-like structure with fibres running along the long axis of the squid as observed by the eye, under the light microscope and the AFM. The diffracted intensities in the X-ray experiments could be assigned to an α -helical protein phase and monoclinic β -chitin crystallites. The corresponding lattice parameters in Table 5 are in good agreement with the parameters for crystalline β -chitin, as determined by Blackwell.^{17,18} The absolute values for the monoclinic parameters a , b and c deviate by $\sim 7\%$ from Blackwell's values. The largest deviation was observed in the lattice parameter a . Because it was not possible to determine the monoclinic angle, γ , independently from our X-ray measurements, this difference could also be the result of a slightly different γ -value. We note that the differences

in the lattice parameters between the two species, which were investigated in this study, were much smaller, namely less than 3%.

Herman's orientation function,

$$f = \frac{3 \langle \cos^2(\phi) \rangle - 1}{2}, \quad (5)$$

was used to determine the degree of orientation of the α -coils and monoclinic β -chitin crystallites with respect to the fibre-axis. The ϕ (azimuthal) profiles are plotted and fitted in Fig. 5a and b. The angular width of peak 2_{\parallel} in Fig. 5a was used to obtain the orientation of the α -coils. The reflections ($3_{\parallel} + 4_{\parallel}$) in Fig. 5b determined the orientation of the β -chitin crystallites. Using the above equation, 92% of the β -chitin crystallites and α -coils in Sample 2 were oriented along the fibre (z) axis of the squid gladius. The values are summarized in Table 5.

The results of the X-ray diffraction experiments indicate a high degree of molecular organization in the native squid gladius. These results strongly support the results of Blackwell,²¹ who suggested chitin fibrils wrapped in helical proteins as the elementary unit of organization. From the X-ray data in Fig. 3 and Table 5, these complexes were found to be highly aligned along the long axis of the gladius. The self-similar structures, which were observed at different length scales in Fig. 2, suggest

that these fibrils organize into larger and larger fibres, which eventually result in the corrugated macroscopic structure.

We note that while the distribution of the 2_{\parallel} reflection in Fig. 5a is well fitted by a Lorentzian peak profile, the top of the peak appears to be slightly split. A splitting of the 2_z peak can also be observed in the 2-dimensional data in Fig. 3a. Peaks 1_z , 2_z , 3_z and 4_z can be assigned to the monoclinic β -chitin phase. If the observed splitting was related to β -chitin, it should be more pronounced in the higher order reflections 3_z and 4_z . The absence of a splitting in these peaks is strong evidence that the observed effect is due to the (001) reflection of the α -coil phase. Following the same argument, the 2_{\parallel} reflection is part of the α -coil phase; peaks 3_{\parallel} and 4_{\parallel} are related to the β -chitin phase. The split is, therefore, indicative of a preferred tilt of $\sim 10^\circ$ of the α -coils in the coiled-coil phase with respect to the z -axis of the gladius.

The size of the β -chitin crystallites and the coiled-coil phase was estimated by applying Scherrer's equation:³⁶

$$L = \frac{0.94\lambda}{B(2\theta)\cos(\theta)}, \quad (6)$$

where λ is the wavelength of the X-ray beam, θ is the diffraction angle, and $B(2\theta)$ is the width of the correlation peak in radians. Using the parameters in Tables 3 and 4 for the 2_{\parallel} and

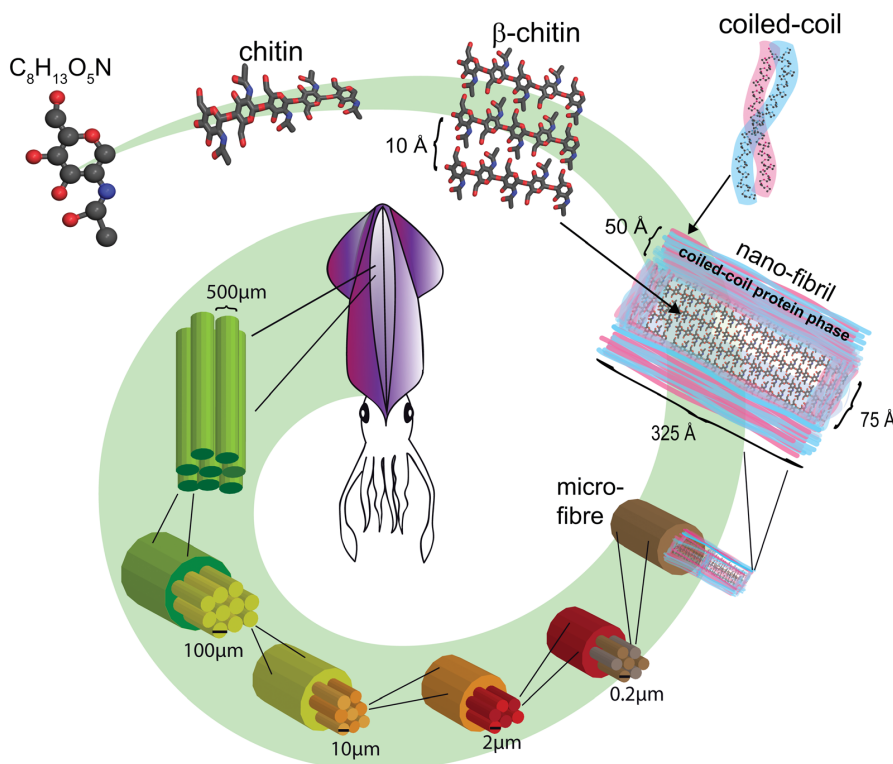


Fig. 6 Hierarchy of the main structural levels in the squid gladius: β -chitin crystallites wrapped in a protein layer form the so-called nano-fibrils, which are the building blocks of $0.2 \mu\text{m}$ sized micro-fibres. These fibres aggregate into $2 \mu\text{m}$, $10 \mu\text{m}$, $100 \mu\text{m}$ and $500 \mu\text{m}$ thick fibres, which eventually form the squid gladius.

3_{\parallel} -reflections for the coil phase and β -chitin, respectively, the size of the corresponding protein phase and the β -chitin crystallites can be calculated. The corresponding values are listed in Table 5.

A protein layer of 51 Å is calculated for Sample 2 and a crystallite size of ~ 74 Å. When assuming that a nano-fibril is composed of one crystallite wrapped in a protein layer, the diameter of such a nano-fibril can be estimated by the size of a crystallite and two layers of proteins to be ~ 176 Å. This value is in good agreement with Mulisch *et al.*,³⁷ who reported ~ 20 nm wide fibrils. From the width of the correlation peak in the z -direction, the length of a nano-fibril can be estimated to be 324 Å, based on a crystallite length of 222 Å and two protein layers. The findings are summarized in Fig. 6.

The smallest fibre (a micro-fibre) that could be resolved in the AFM experiments in Fig. 2 and Table 2 had a diameter of about 2000 Å (0.2 μm). Based on the spatial resolution of AFM and X-ray experiment we can at this point not exclude the existence of even smaller fibres whose size would be slightly too small to be resolved by the AFM, yet too large to be detected by wide-angle X-ray diffraction. However, when assuming that the nano-fibrils form a hexagonally close-packed structure, the total number of nano-fibrils in a micro-fibre can be estimated by the ratio between their areas multiplied by the packing density of close-packed cylinders of 0.91 to ~ 117 nano-fibrils.

One of the hallmarks of biological materials is their strictly hierarchical organization at different levels.^{12,33} This organization is often linked to superior mechanical properties, such as high tensile strength, toughness, and bending resistance.³⁸ The corresponding structures are typically assembled from the bottom up, rather than from the top down, and spontaneously self-assemble at the nanoscale. The fact that natural materials are grown (both the material and the whole organism grow at the same time) rather than being fabricated makes them more complex than synthetic materials.³⁹ Hierarchical self-assembly is often related to fractals because of their self-similarity, as recently reported for coiled-coil peptides⁴⁰ and in particular protein fibres.^{41,42} The process of self-assembly is the result of a complex interplay between free energy and entropy, where the order and organization eventually win over the second law of thermodynamics.⁴³

5. Conclusions

The squid gladius is an internal structure that supports the squid's mantle and serves as a site for muscle attachment. It is made of two main components, proteins and β -chitin. We find evidence for a hierarchical, self-similar structure in the native squid gladius from millimetres down to the molecular level. The extracted gladii showed an anisotropic, fibre-like structure as observed by the eye and under the microscope. A self-similar structure was observed at the nanoscale with AFM, and fibres with diameters from 500 μm down to 0.2 μm were observed. Using X-ray diffraction, the molecular structure of native squid gladii of the two different species was determined. Scattering signals corresponding to an α -helical protein phase and the monoclinic β -chitin crystallites were observed. The chitin lattice

parameters in the two species agreed well with parameters reported in the literature. About 90% of the α -coils and β -chitin crystallites were found to be oriented along the fibre axis. From the size of a β -chitin crystallite and the protein phase, the size of a nano-fibril was estimated to be ~ 150 Å \times 300 Å. About 100 nano-fibrils then form a micro-fibre, with a diameter of 0.2 μm . The experiments present evidence for a strong correlation between the macroscale structure and molecular orientation.

Acknowledgements

This research was funded by the Natural Sciences and Engineering Research Council (NSERC) of Canada, the National Research Council (NRC), the Canada Foundation for Innovation (CFI), and the Ontario Ministry of Economic Development and Innovation. H.D. is the recipient of NSERC Undergraduate Research Awards (USRA). M.C.R. is the recipient of an Early Researcher Award from the Province of Ontario.

References

- 1 A. G. Richards, *The Integument of Arthropods: the Chemical Components and Their Properties, the Anatomy and Development, and the Permeability*, University of Minnesota Press, 1951.
- 2 N. Runham, Investigations into the histochemistry of chitin, *J. Histochem. Cytochem.*, 1961, **9**, 87–92.
- 3 K. Rudall, The distribution of collagen and chitin in fibrous proteins and their biological significance, *Symp. Soc. Exp. Biol.*, 1955, **9**, 4971.
- 4 K. Rudall and W. Kenchington, The chitin system, *Biol. Rev.*, 1973, **48**, 597–636.
- 5 C. Brown, *Structural materials in animals*, London, Pitman, 1975.
- 6 L. R. Pont and L. Quesada-Allue, Chitin, *Methods Plant Biochem.*, 1990, **2**, 443–481.
- 7 M. Giraud-Guille, E. Belamie and G. Mosser, Organic and mineral networks in carapaces, bones and biomimetic materials, *Comptes Rendus Palevol*, 2004, **3**, 503–513.
- 8 K. Kurita, Chitin and chitosan: Functional biopolymers from marine crustaceans, *Mar. Biotechnol.*, 2006, **8**, 203–226.
- 9 R. Kumar, R. Muzzarelli, C. Muzzarelli, H. Sashiwa and A. Domb, Chitosan chemistry and pharmaceutical perspectives, *Chem. Rev.*, 2004, **104**, 6017–6084.
- 10 I. Aranaz, M. Mengibar, R. Harris, I. Paños, B. Miralles, *et al.* Functional characterization of chitin and chitosan, *Curr. Chem. Biol.*, 2009, **3**, 203–230.
- 11 P. Austin, C. Brine, J. Castle and J. Zikakis, Chitin: New facets of research, *Science*, 1981, **212**, 749–753.
- 12 R. A. Muzzarelli, *Chitin nanostructures in living organisms*, Chitin, Springer, Heidelberg, 2011, pp. 1–34.
- 13 K. Rudall, The chitin/protein complexes of insect cuticles, *Adv. Insect Physiol.*, 1963, **1**, 257–313.
- 14 F. Khoushab and M. Yamabhai, Chitin research revisited, *Mar. Drugs*, 2010, **8**, 1988–2012.
- 15 R. Minke and J. Blackwell, The structure of α -chitin, *J. Mol. Biol.*, 1978, **120**, 167–181.

5.3 Paper III: The Structure of People's Hair

Fei-Chi Yang, Yuchen Zhang, and Maikel C. Rheinstädter. “*The Structure of People's Hair*”. Accepted for publication in PeerJ in September 2014.

5.3.1 Preface to Paper III

The initial goal of this project was to examine the structural anomalies of hair using X-ray diffraction. If these abnormal structures could be related to a certain type of disease, then X-ray screening could act as an inexpensive, non-invasive diagnostic tool. However, we found that the structures of hair vary even between healthy subjects such that we have to understand the general features of hair first before further conclusions can be made.

Based on the X-ray two-dimensional data, we found the signals from the α -coiled coils, intermediate filaments, and the lipids. The standard deviation of the length scale corresponding to three structural components were calculated. Genetic similarity for the structure of hair was discussed.

Author Contributions

- *Experiment Design:* Maikel C. Rheinstädter
- *Sample Preparation:* **Fei-Chi Yang** and Yu-Chen Zhang
- *Experiment Performing:* **Fei-Chi Yang**, Yu-Chen Zhang, and Maikel C. Rheinstädter
- *Data Analysis:* **Fei-Chi Yang** and Yu-Chen Zhang

- *Manuscript Writing:* Maikel C. Rheinstädter, **Fei-Chi Yang** and Yu-Chen Zhang

The Structure of People's Hair

Fei-Chi Yang,¹ Yu-Chen Zhang,¹ and Maikel C. Rheinstädter^{1,*}

¹*Department of Physics and Astronomy, McMaster University, Hamilton, Ontario, Canada*

(Dated: September 23, 2014)

Hair is a filamentous biomaterial consisting mainly of proteins, in particular keratin. The structure of human hair is well known: the *medulla* is a loosely packed, disordered region near the centre of the hair surrounded by the *cortex*, which contains the major part of the fibre mass, mainly consisting of keratin proteins and structural lipids. The *cortex* is surrounded by the *cuticle*, a layer of dead, overlapping cells forming a protective layer around the hair. The corresponding structures have been studied extensively using a variety of different techniques, such as light, electron and atomic force microscopes, and also X-ray diffraction. We were interested in the question how much the molecular hair structure differs from person to person, between male and female hair, hair of different appearance, such as colour and waviness. We included hair from parent and child, identical and fraternal twins in the study to see if genetically similar hair would show similar structural features.

The molecular structure of the hair samples was studied using high-resolution X-ray diffraction, which covers length scales from molecules up to the organization of secondary structures. Signals due to the coiled-coil phase of α -helical keratin proteins, intermediate keratin filaments in the *cortex* and from the lipid layers in the cell membrane complex were observed in the specimen of all individuals, with very small deviations. Despite the relatively small number of individuals (12) included in this study, some conclusions can be drawn. While the general features were observed in all individuals and the corresponding molecular structures were almost identical, additional signals were observed in some specimen and assigned to different types of lipids in the cell membrane complex. Genetics seems to play a role in this composition as identical patterns were observed in hair from father and daughter and identical twins, however, not for fraternal twins. Identification and characterization of these features is an important step towards the detection of abnormalities in the molecular structure of hair as potential diagnostic tool for certain diseases.

1. INTRODUCTION

Human scalp hair is a bio-synthesized material that has a complex internal structure. The adult human hair is around 20-180 μm in width, and generally grows to a length of approximately 90 cm. It consists of many layers including the *cuticle*, the *cortex* and the *medulla*. These layers are bound together by the cell membrane complex¹.

The structure of human hair is well known and in particular X-ray diffraction revealed details of molecular structure and organization within hair²⁻¹⁹. In particular microbeam small angle X-ray scattering techniques enables to determine hair structure with a high spatial resolution^{4,7,10,20,21}. It is a long-standing question if changes in the molecular structure of nail or hair can be related to certain diseases and potentially be used as a diagnostic tool. Such a technique would in particular be interesting and relevant as simple, non-invasive screening method for cancer^{16,18,19}. Abnormal kinky hair is, for instance, characteristic of giant axonal neuropathy²².

The purpose of this study is to use X-ray diffraction to analyze the structure of human scalp hair for individuals with differing characteristics. The 12 individuals in this

study include hair from men and women, hair of different colour and appearance, such as straight, wavy and curly. In addition of appearance, the study also includes hair from father and daughter, a pair of identical and a pair of fraternal twins to include genetic similarities. All hair was collected from healthy individuals and care was taken that the hair was not permed or dyed before the experiments.

Signals due to the coiled-coil organization of α -helical keratin proteins and intermediate filaments in the *cortex*, and lipids in the cell membrane complex were observed in the hair of all individuals. While these general features occur independent of gender or appearance of the hair with a very small standard deviation in the underlying molecular dimensions, we find significant differences between individuals in the composition of the plasma membrane in the cell membrane complex. Genetics appear to be the most important factor that determines membrane composition, as no or little differences were observed in genetically related hair samples rather than external factor, such as nutrition or hair care products.

1.1. Properties of Human Hair

The *cuticle* is the outermost layer formed by flat overlapping cells in a scale-like formation¹. These cells are approximately 0.5 μm thick, 45-60 μm long and found at 6-7 μm intervals¹. The outermost layer of the *cuticle*, the epicuticle, is a lipo-protein membrane that is estimated to be 10-14 nm thick²³. Beneath that is the *A* layer with

* Department of Physics and Astronomy, McMaster University, ABB-241, 1280 Main Street West, Hamilton, Ontario L8S 4M1, Canada; Phone: +1-(905)-525-9140-23134, Fax: +1-(905)-546-1252, E-mail:rheinstadter@mcmaster.ca

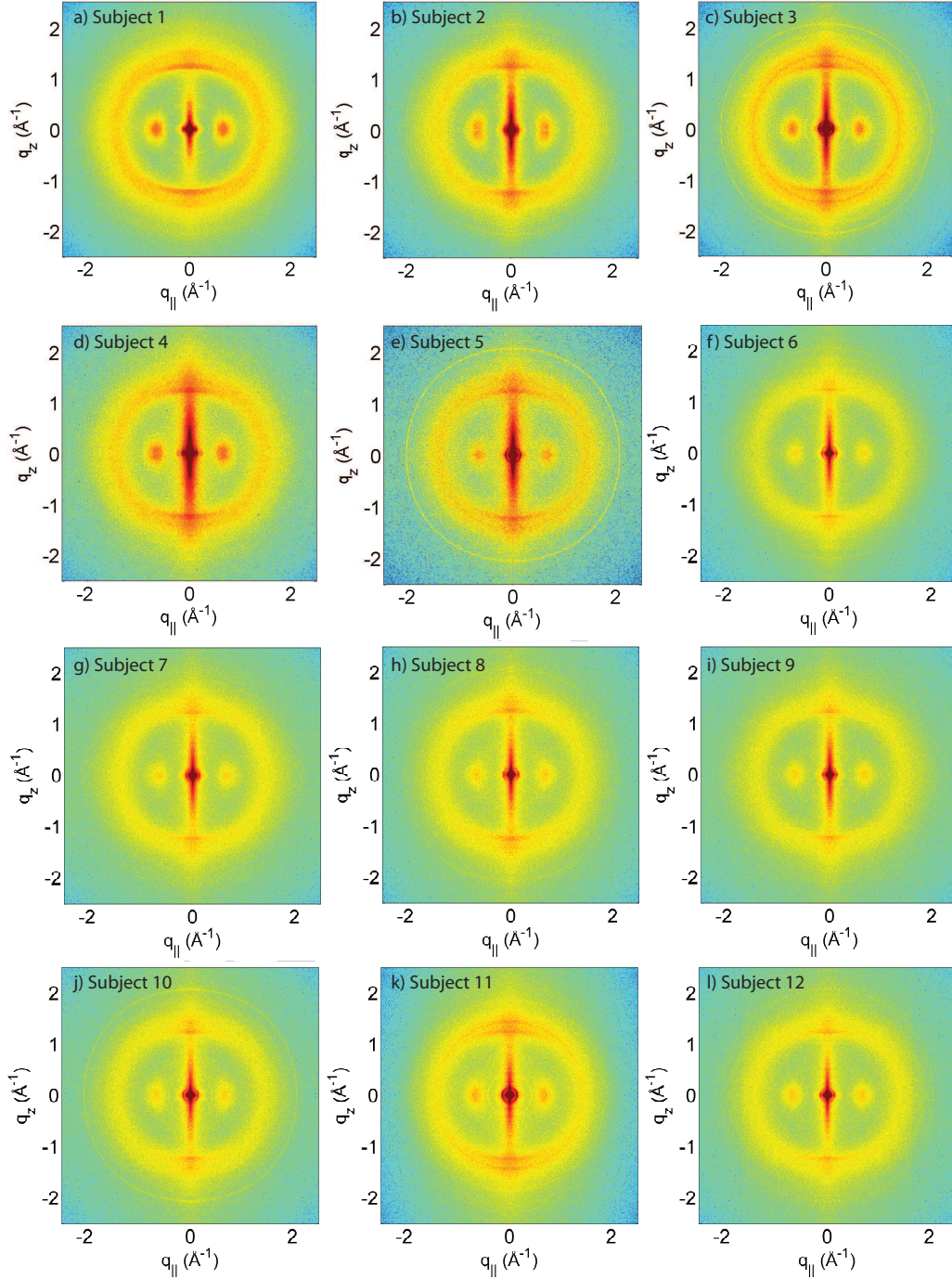


FIG. 1. Two-dimensional X-ray data of all 12 subjects. The hair strands were oriented with the long axis of the hair parallel to the vertical z -axis. The $(q_{||}, q_z)$ -range shown was determined in preliminary experiments to cover the features observable by X-ray diffraction. The measurements cover length scales from about 3-90 Å to study features from the coiled-coil α -keratin phase, keratin intermediate filaments in the *cortex*, and the membrane layer in the membrane complex. While common features can easily be identified in the 2D plots, subtle differences are visible, which are discussed in detail in the text.

56 a high cysteine content and a thickness of 50-100 nm,
 57 the exocuticle with again a high cysteine content and a
 58 highly variable thickness ranging from 50 to 300 nm, and
 59 the endocuticle with a low cysteine content and a thick-
 60 ness also ranging from 50 to 300 nm.

61 Majority of the hair fibre is the cortex, which contains
 62 spindle shaped cells that lie parallel along the fibre axis.
 63 These cortical cells were found to be approximately 1-
 64 6 μm in diameter and 50-100 μm in length²⁴. In wool
 65 fibres as well as human hair, the cortical cells were ob-
 66 served to be divided into different regions termed ortho-
 67 cortex, paracortex and mesocortex²⁵. The difference in
 68 distribution of these cell types is an important factor for
 69 determining the curvature of the hair fibre²¹. In particu-
 70 lar, straight hair tends to have symmetrical distribution
 71 of the ortho- and paracortices whereas curly hair tends
 72 to have a non-symmetrical distribution of these cortical
 73 cells²¹. Most of the cortical cells are composed of a pro-
 74 tein known as keratin¹.

75 At the molecular level, keratin is a helical protein²⁶.
 76 There are two types of keratin fibres that exist in hair,
 77 type I with acidic amino acid residues and type II with
 78 basic amino residues. One strand of type I fibre and
 79 one strand of type II fibre spiral together to form coiled-
 80 coil dimers. In turn, these dimers coil together in an
 81 antiparallel manner to form tetramers^{27,28}.

82 When tetramers are connected from head to tail,
 83 they are known as protofilaments¹. These tetramers
 84 or protofilaments are believed to interact together to
 85 form a single intermediate filament which is approxi-
 86 mately 75-90 \AA in diameter. The current model of an
 87 intermediate filament was proposed in the 1980's and
 88 it involves 7 protofilaments surrounding a single core
 89 protofilament^{1,28}. The intermediate filaments then ag-
 90 gregate together to form macro-filaments with a diameter
 91 of 1000 to 4000 \AA ^{1,5}. Between the intermediate filaments
 92 is a matrix consisting of keratin associated proteins which
 93 is irregular in structure. The macro-fibrils consisting of
 94 intermediate filaments and the surrounding matrix are
 95 the basic units of the cortical cell.

96 The cell membrane complex is the material that glues
 97 hair cells together. There exist various types of cell
 98 membrane complexes: *cuticle-cuticle*, *cuticle-cortex* and
 99 *cortex-cortex* depending on the location¹. The general
 100 membrane structure is one 15 nm proteinous delta layer
 101 sandwiched by two 5 nm lipid beta layers²⁹. Much spec-
 102 ulation still exist regarding the precise structure of the
 103 beta and delta layers. However, it has been determined
 104 that 18-methyl eicosanoic acid, a covalently bound fatty
 105 acid, exists in the upper beta layer in the *cuticle-cuticle*
 106 but not in cortex-cortex membranes³⁰. In fact, most
 107 of the fatty acids in beta layers of membranes in the
 108 *cuticle-cuticle* are covalently bound and most the fatty
 109 acids in the beta layers of *cortex-cortex* are non-covalently
 110 bound¹. Further evidence suggests that the fatty acids
 111 in *cuticle-cuticle* membranes is organized in a monolayer
 112 whereas the fatty acids in cortex-cortex cell membranes
 113 is a bilayer¹. The *cuticle-cortex* cell membrane complex

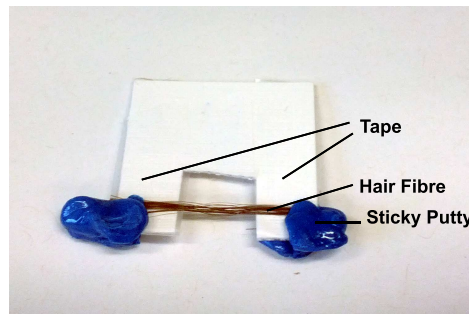


FIG. 2. The apparatus used to mount the hair strands in the experiment. The cardboard apparatus is then mounted vertically onto the loading plate of the Biological Large Angle Diffraction Experiment (BLADE) using sticky putty.

114 is then a mixture of the two, with the side facing the
 115 *cuticle* similar to *cuticle-cuticle* membranes and the side
 116 facing the cortex similar to cortex-cortex membranes¹.

117 2. MATERIALS & METHODS

118 2.1. Preparation of Hair Samples

119 This research was approved by the Hamilton Inte-
 120 grated Research Ethics Board (HIREB) under approval
 121 number 14-474-T. Written consent was obtained from all
 122 participating individuals. Scalp hair samples were gath-
 123 ered from 12 adults of various age, gender, ethnicities,
 124 hair colour and hair curvature. It is of interest to note
 125 that there are 3 pairs of study participants with genetic
 126 relations including father and daughter, fraternal twins
 127 and identical twins. Characteristics of the samples are
 128 listed in Table 1.

130 The hair samples gathered were cut into strands
 131 around 3 cm long. Care was taken to not stretch or
 132 deform the hair strands during this process. For each
 133 subject, around 10 strands were taped onto a flexible
 134 cardboard apparatus as shown in Figure 2. The cut-out
 135 at the middle of the apparatus is where scattering occurs
 136 on the hair sample. The cardboard apparatus is then
 137 mounted vertically onto the loading plate of the Biologi-
 138 cal Large Angle Diffraction Experiment (BLADE) using
 139 sticky putty as shown in Figure 2. All hair samples were
 141 measured at room temperature and humidity of 22°C and
 142 50% RH.

143 2.2. X-ray Diffraction Experiment

144 X-ray diffraction data was obtained using the Biologi-
 145 cal Large Angle Diffraction Experiment (BLADE) in the
 146 Laboratory for Membrane and Protein Dynamics at Mc-
 147 Master University. BLADE uses a 9 kW (45 kV, 200 mA)

Subject	gender	diameter(μm) \pm SD	color	appearance	special comment
1	F	30 ± 3	light blonde	straight	daughter
2	M	49 ± 5	brown/grey	curly	father
3	F	74 ± 7	black	wavy	—
4	M	50 ± 5	light Brown	curly	—
5	F	49 ± 5	blonde	curly	—
6	F	43 ± 4	light brown	straight	—
7	F	61 ± 6	light brown	wavy	—
8	F	49 ± 5	black	wavy	—
9	F	31 ± 3	blonde	wavy	identical twin
10	F	66 ± 7	black	straight	fraternal twin
11	F	69 ± 7	black	straight	fraternal twin
12	F	48 ± 5	blonde	curled	identical twin

TABLE 1. List of all hair samples in this study. The individuals include men and women, hair of different appearance, such as thickness, colour and waviness, and also genetically related hair samples from father and daughter, a pair of identical and a pair of fraternal twins. Labeling agrees with the data shown in Figure 1.

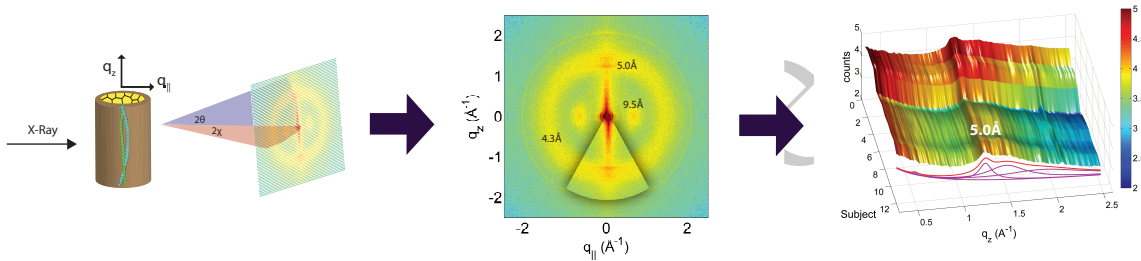


FIG. 3. Schematics of the X-ray setup and example X-ray data. The hair strands were oriented in the X-ray diffractometer with their long axis along q_z . Two-dimensional X-ray data were measured for each specimen covering distances from about 3-90 Å including signals from the coiled-coil α -keratin phase, the intermediate fibrils in the *cortex* and from the cell membrane complex. The 2-dimensional data were integrated and converted into line scans and fit for a quantitative analysis.

148 CuK α Rigaku Smartlab rotating anode at a wavelength
 149 of 1.5418 Å. Focusing multi-layer optics provided a high
 150 intensity parallel beam with monochromatic X-ray
 151 intensities up to 10^{10} counts/(s \times mm 2) at the sample
 152 position. In order to maximize the scattered intensity,
 153 the hair strands were aligned parallel to the parallel beam
 154 for maximum illumination. The slits were set such that
 155 about 15 mm of the hair strands were illuminated with
 156 a width of about 100 μm . The effect of this particu-
 157 lar beam geometry is seen in the 2-dimensional data in
 158 Figure 1: while it produces a high resolution along the
 159 equator, the main beam is significantly smeared out in
 160 the q_z -direction up to q_z -values of about 0.5 \AA^{-1} , limiting
 161 the maximum observable length scale to about 13 Å.

162 The diffracted intensity was collected using a point
 163 detector. Slits and collimators were installed between
 164 X-ray optics and sample, and between sample and de-
 165 tector, respectively. By aligning the hair strands in the
 166 X-ray diffractometer, the molecular structure along the
 167 fibre direction and perpendicular to the fibres could be
 168 determined. We refer to these components of the total
 169 scattering vector, \vec{Q} , as q_z and $q_{||}$, respectively, in
 170 the following. An illustration of q_z and $q_{||}$ orientations

171 is shown in Figure 3. The result of an X-ray experi-
 172 ment is a 2-dimensional intensity map of a large area of
 173 the reciprocal space of $-2.5 \text{ \AA}^{-1} < q_z < 2.5 \text{ \AA}^{-1}$ and
 174 $-2.5 \text{ \AA}^{-1} < q_{||} < 2.5 \text{ \AA}^{-1}$. The corresponding real-space
 175 length scales are determined by $d = 2\pi/|Q|$ and cover
 176 length scales from about 3 to 90 Å, incorporating typical
 177 molecular dimensions and distances for secondary protein
 178 and lipid structures.

179 Integration of the 2-dimensional data was performed
 180 using Matlab, MathWorks. By adding up the peak in-
 181 tensities along the q_z and the $q_{||}$ directions, 1-dimensional
 182 data along each of the two directions were produced. The
 183 q_z intensity was integrated azimuthally for an angle of
 184 25 degrees over the meridian. The $q_{||}$ intensity was in-
 185 tegrated azimuthally for an angle of 25 degrees over the
 186 equator.

187 The fitting process is performed on both the 1-
 188 dimensional q_z and the $q_{||}$ data produced from integra-
 189 tion. Distinguishable peaks were observed and fitted with
 190 the least numbers of Lorentzian peak functions with an
 191 exponential decay background of the form $(a \cdot q^b + c)$
 192 in the first run. Initial Parameters were chosen based on
 193 the observed positions for width and height of the peaks

194 and free to move through the entire q -range. The crite- 246
 195 rion for the final parameters was to minimize the mean 247
 196 square of the difference between data intensity and the 248
 197 fitted intensity. If the fitted intensity can not conform 249
 198 to the shape of the data intensity, more peaks will be 250
 199 added in the following runs until a good fit is acquired. 251
 200 This process was repeated for all 12 subjects and per- 252
 201 formed with little or no consultation of previous fittings 253
 202 to minimize bias. 254

203 As for the SAXS data, Gaussian functions are used 255
 204 instead. We note that the use of optical components 256
 205 in the beam path has an impact on the shape of the ob- 257
 206 served Bragg peaks: instead of Lorentzian or Bessel peak 258
 207 functions, Gaussian peak profiles were found to best de- 259
 208 scribe the SAXS peaks. The fitting process was the same 260
 209 as mentioned before: three Gaussians were fitted to the 261
 210 SAXS data using free-to-move parameters and an expo- 262
 211 nential decay background. However, for some subjects, 263
 212 the third peak was noisy and the least mean square loga- 264
 213 rithm could not reach a good fit and hence the data was 265
 214 fitted with two Gaussians, only.

215

3. RESULTS

216 A total of 12 adult subjects participated in this study. 271
 217 Details of gender and appearance of the hair strands are 272
 218 listed in Table 1. About 10 strands were cut from the 273
 219 scalp, glued onto a sample holder and aligned in the X-ray 274
 220 diffractometer. The resulting 2-dimensional X-ray inten- 275
 221 sity maps of the reciprocal space reveal exquisite details 276
 222 of the molecular structure of human scalp hair, as pre- 277
 223 sented in Figure 1. The hair strands were oriented with 278
 224 the long axis of the hair parallel to the vertical z -axis. 279
 225 The displayed ($q_z, q_{||}$)-range was determined to cover the 280
 226 length scales of the features of interest in preliminary 281
 227 experiments. 282

228 The data in Figures 1 show a distinct non-isotropic 283
 229 distribution of the diffracted intensity with pronounced 284
 230 and well defined intensities along the long axis of the hair 285
 231 and in the equatorial plane (the q_z and $q_{||}$ -axes, respec- 286
 232 tively), indicative of a high degree of molecular order in 287
 233 the hair strands. Some features were common in all spec- 288
 234 imens and assigned to certain molecular components, as 289
 235 explained in the next section.

236

3.1. Assignment of Common Scattering Signals

237 *a. Coiled-coil Protein Phase in the Cortex* The ker- 298
 238 atin proteins in the *cortex* are known to organize in bun- 299
 239 dles, whose structure is dominated by α -helical coiled- 300
 240 coils^{26,31,32}. The main features of this pattern is a $\sim 9.5 \text{ \AA}$
 241 (corresponding to $q_{||} \sim 0.6 \text{ \AA}^{-1}$) equatorial reflection cor-
 242 responding to the spacing between adjacent coiled-coils
 243 and a $\sim 5.0 \text{ \AA}$ meridional reflection (corresponding to
 244 $q_z \sim 1.25 \text{ \AA}^{-1}$) corresponding to the superhelical struc-
 245 ture of α -helices twisting around each other within coiled-

246 coils³³⁻³⁵. As displayed in Figure 4, these signals were
 247 observed in the X-ray data in all specimen and assigned
 248 to the coiled-coil protein phase. We note that these
 249 peaks are related to generic α -helical coil structures of
 250 monomeric proteins, and not specific to a certain type of
 251 protein.

252 *b. Lipids in the Cell Membrane Complex* The cell
 253 membrane complex mainly consists of lipid mono- and
 254 bilayers. The corresponding scattering features corre-
 255 spond to a lamellar periodicity of about 45 \AA , and rings
 256 at spacings of about 4.3 \AA , characteristic of the order
 257 within the layers⁴. Both these features are observed in
 258 the 2-dimensional X-ray data of all individuals in Fig-
 259 ure 1, as a ring-like scattering intensity at q -values of
 260 $\sim 0.1 \text{ \AA}^{-1}$ and a broad, ring-like scattering at $\sim 1.5 \text{ \AA}^{-1}$
 261 as a result of the lipid order within the membrane layers.
 262 The corresponding diffraction signal has a maximum on
 263 the q_z -axis, indicating a preferential orientation of the
 264 membrane plane parallel to the surface of the hair.

265 *c. Intermediate Filaments in the Cortex* The ker-
 266 atin coils organize into intermediate filaments, whose
 267 structure and packing in the plane of the hair result in
 268 additional scattering signals. The packing of these fibrils
 269 by bundling into macro-fibrils is characterized by X-ray
 270 diffraction pattern by three equatorial spots located at
 271 about $90, 45$ and 27 \AA . The corresponding signals are
 272 observed in the 2-dimensional data in Figure 1. The ex-
 273 act position of the features is, however, best determined
 274 in small angle diffraction experiments (SAXS), which of-
 275 fer a drastically improved resolution, and will be shown
 276 below. We note that the axial packing of coiled-coils
 277 within keratin filaments in hair gives rise to a number of
 278 fine arcs along the meridian (z). The typically observed
 279 signal on the meridian at 67 \AA , which arises from the
 280 axial stagger between molecules along the microfibril^{3,15},
 281 could not be observed in our experiments due to the re-
 282 lax resolution of the parallel beam in this direction.
 283 While the features observed in scattering experiments are
 284 well known, the molecular architecture of the interme-
 285 diate filaments is still discussed¹⁵. Supercoiled coiled-
 286 coils or models that involve straight dimers models with dif-
 287 ferent numbers of coils are being discussed.

288 The three features above are displayed in Figure 4 and
 289 observed in all individuals in Figure 1. The underlying
 290 molecular structures will be quantitative analyzed in the
 291 next Section (Section 3.2). We note that additional fea-
 292 tures are seen in some of the measurements in Figure 1,
 293 mainly in the broad membrane ring at around 1.5 \AA^{-1}
 294 which indicate a difference in molecular composition of
 295 the cell membrane complex between individuals. We will
 296 come back to these differences in the Discussion in Sec-
 297 tion 4.

3.2. Quantitative Analysis of Scattering Results

298 In order to quantitatively determine the position of the
 299 corresponding scattering features, the 2-dimensional data
 300

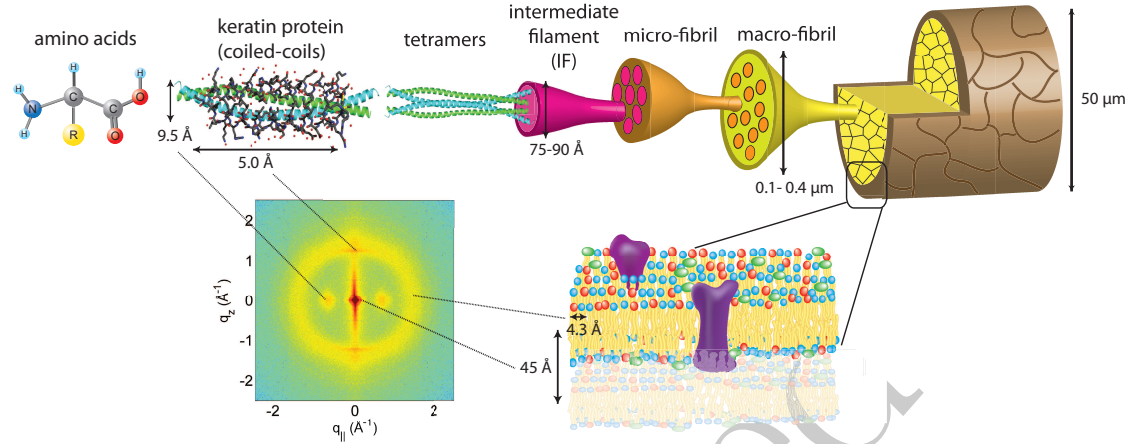


FIG. 4. The hierarchical structure of hair in the *cortex* and *cuticle*. The main component of the *cortex* is a keratin coiled-coil protein phase. The proteins form intermediate filaments, which then organize into larger and larger fibres. The hair is surrounded by the *cuticle*, a dead cell layer. The common features observed in the X-ray data of all specimens are signals related to the coiled-coil keratin phase and the formation of intermediate filaments in the *cortex*, and the cell membrane complex. Signal assignment and corresponding length scales are shown in the Figure.

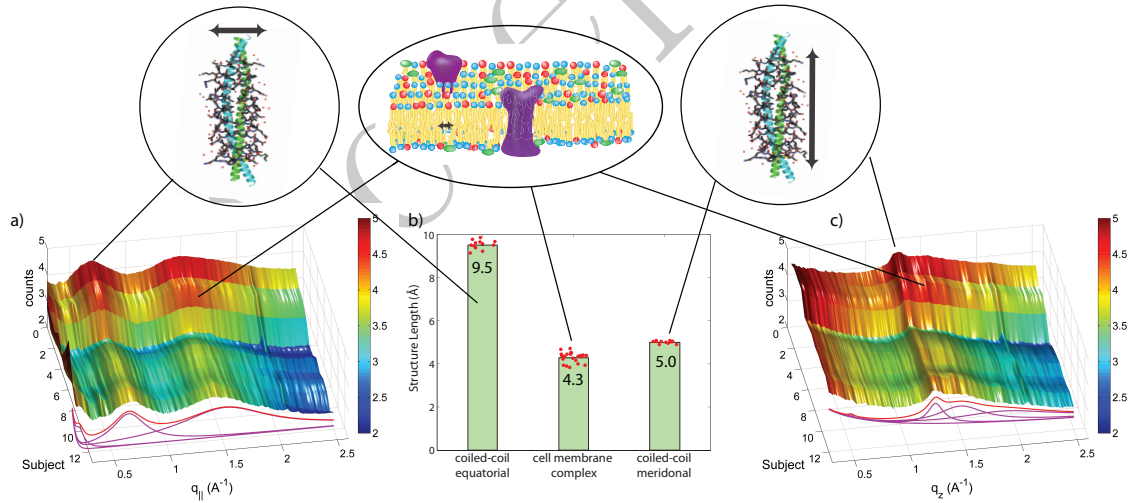


FIG. 5. Integration of the 2-dimensional scattering data. Integration of the 2-dimensional scattering data in Figure 1 in the equatorial plane ($q_{||}$) a), and along the axis of the hairs (q_z) c), respectively, for all Subjects. The two signals present in all individuals in the equatorial plane ($q_{||}$) correspond to the distance between two coiled-coils of 9.5 Å and between two lipid tails in the cell membrane cortex of 4.3 Å. The common meridional signal along the long axis of the hair (q_z) at 5 Å corresponds to the α -helices twisting around each other within coiled-coils. Average values and standard deviations are given in part b).

for all 12 individuals were integrated in the equatorial plane (q_{\parallel} -axis) of the hair fibres, and along the hair fibres (q_z -axis). The resulting plots are shown in Figure 5. In the direction along the hair fibre axis (q_z), there are two major peaks that were consistent among all subjects, one narrow peak around 5.0 Å and one broader peak around 4.3 Å.

In the direction perpendicular to the hair fibre axis (q_{\perp}), there are also two major peaks consistent among all subjects, one narrow peak around 9.5 Å and one broad peak around 4.3 Å. The total scattering profile was well fit by two Lorentzian peak profiles (and a background), whose positions is plotted in Figure 5. The signals at 5.0 Å and 9.5 Å are in excellent agreement with signals reported from coiled-coil keratin proteins²⁶, as depicted in the Figure. The broad signal at about 4.3 Å present in both direction is due to the ring-like scattering from the lipids in the membrane component. As plotted in Figure 5, there is a narrow distribution of the corresponding length scales with standard deviations of 9.51 ± 0.07 Å and 5.00 ± 0.02 Å for the keratin coiled-coils and 4.28 ± 0.08 Å for the membrane signal, indicative that the common features observed in all individuals are well defined with little spread in the corresponding molecular dimensions.

Due to the large length scales involved, the signals from intermediate filaments occur at small scattering vectors, shown in Figure 6. The Small Angle X-ray Scattering (SAXS) profile was well fit with three Gaussian peaks at 90 Å, 45 Å, and 27 Å. We note that the third peak was not observed in all hair samples. The corresponding peak positions and distributions are shown in the Figure. The 90 Å has been reported early in the literature as the distance between intermediate filaments human hair. As further elaborated by Rafik *et al.*¹⁵, these peaks correspond to the radial structures of the intermediate filaments and can be well-simulated by assuming parallel tetramers formed by 2 coiled-coils with a slight disorder in positions and orientations, as depicted in the Figure. Also here, the standard deviations of 90 ± 2 Å, 47 ± 2 Å, 27 ± 1 Å, as shown in the Figure, are small, indicative that the organization of the intermediate filaments on the nanoscale varies very little between different individuals.

4. DISCUSSION

All hair used in this study was in its native state, collected from healthy individuals and not chemically treated prior to the experiments. However, all individuals regularly used shampoos for cleaning and additional products such as conditioners, wax and gel. These products function primarily at or near the fiber surface to remove dirt from the hair surface, for instance, and do not seem to have an impact on the internal keratin structure, as will be discussed below.

An abnormal signal was previously reported by James

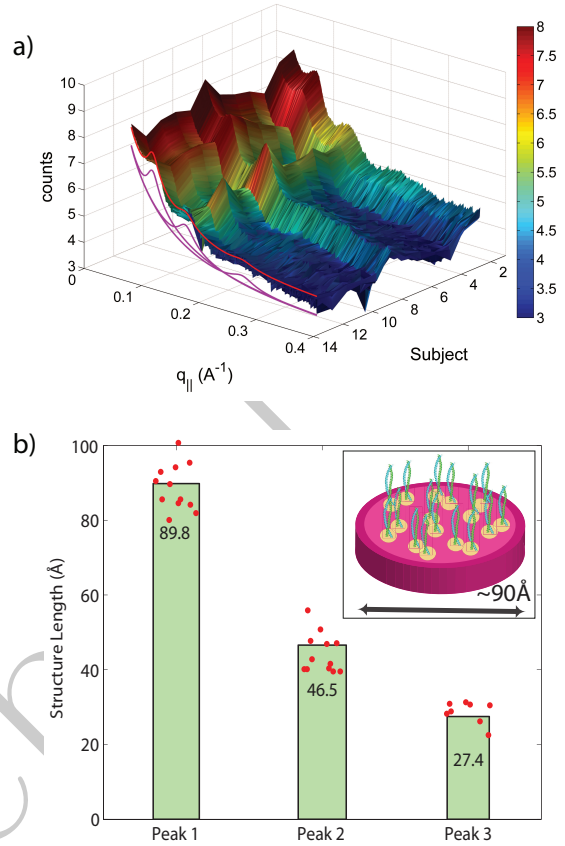


FIG. 6. Diffraction features at small scattering angles. The small q_{\parallel} -range is shown in magnification in a). The specimen of most individuals showed 3 distinct reflections at ~ 90 Å, 46.5 Å and 27 Å, related to the properties of intermediate keratin filaments (b).

*et al.*¹⁶ in hair samples of patients with breast cancer. Such an approach is quite intriguing, as scanning of hair samples could be used as easy, inexpensive and non-invasive screening techniques in the diagnosis of cancer. James *et al.* observed a ring-like signal at 44.4 Å, at the position of the lamellar plasma membrane signal, and assigned this signal to the presence of breast cancer. The analysis and assignment was questioned later on by Briki *et al.*¹⁸ and Howell *et al.*³⁶, who observed this feature in healthy and cancer patients in equal measure. The ring-like 45 Å signal is also present in the data for all individuals included in our study, such that a relation to breast cancer can most likely be excluded.

4.1. General Structural Features from the X-ray Experiments

From the 2-dimensional X-ray data in Figures 1 and 4, and the analysis in Figures 5 and 6, we identify three features present in all individuals. These signals are related to the coiled-coils arrangement of the keratin proteins in the *cortex*, the formation of intermediate filaments in the *cortex*, and lipids in the cell membrane complex of the hair. Statistical analysis of the corresponding molecular dimensions revealed a rather small distribution between different individuals. These general properties of human hair are observed in all hair independent of gender, colour or optical appearance of the hair (as listed in Table 1) within the number of individuals included in this study.

Differences in the X-ray data between individuals were observed in the wide angle region (WAXS) of the 2-dimensional data in Figure 1, related to properties of the membrane component. Figure 7 a) shows a comparison between individual 3 and 4 to illustrate the effect. For an easy comparison the original data were cut in half and recombined, such that the left half depicts individual 3, and the right half individual 4. While signals from the coiled-coil protein phase, the diffuse, ring-like intensity from lipids in the cell membrane complex and the small angle signals due to the formation of intermediate filaments are observed in both individuals, additional signals occur in Subject 3 around the position of the membrane-ring. Almost identical patterns are observed in Figure 7 b) and c), while differences are seen in part d); this will be discussed in detail below.

The additional signals observed between about 1.34 \AA^{-1} and 1.63 \AA^{-1} can be assigned to fatty acids located within the plasma membrane of the cell membrane complex. The position of these lipids inside the hair was determined by synchrotron infrared microspectroscopy³⁷ detecting the corresponding CH_2 and CH_3 bands. The lipid component of the cell membrane complex consists of three major classes of lipids: glycerolipids (mainly phospholipids), sterols and sphingolipids³⁸. The most abundant lipid species are referred to as structural lipids up to 80% of which are phosphocholine (PC) and phosphoethanolamine (PE) phospholipids.

The position and width of the broad, ring-like intensity observed in all specimen in Figure 1 agree well with lipid correlation peaks reported from single and multi-component phospholipid fluid lipid membranes³⁹⁻⁴⁷ and diffraction observed in plasma membranes^{48,49}. The broad correlation peak is the tell-tale sign of a fluid-like, disordered membrane structure. It is related to the packing of the lipid tails in the hydrophobic membrane core, where the lipid acyl chains form a densely packed structure with hexagonal symmetry (planar group $p6$)⁵⁰. The distance between two acyl tails is determined to be $a_T = 4\pi/(\sqrt{3}q_T)^{51-53}$, where q_T is the position of the membrane correlation peak. The average nearest-neighbour distance between two lipid tails is calculated from the peak position to 4.97 \AA . We note that the in-

tensity of the disordered membrane component is not distributed isotropically on a circle, which would be indicative of a non-oriented, isotropic membrane phase. The corresponding scattering signal has a maximum along the q_z -axis, indicative that most of the membranes are aligned parallel to the hair surface.

The additional narrow components in Figure 1 between about 1.34 \AA^{-1} and 1.63 \AA^{-1} , which are observed in some hair samples, agree with structural features reported in lipid membranes of different composition. A correlation peak at $\sim 1.5 \text{ \AA}^{-1}$ was found in the gel phase of saturated phospholipid membranes, such as DMPC (Dimyristoyl-sn-glycero-3-phosphocholine) and DPPC (Dipalmitoyl-sn-glycero-3-phosphocholine)^{42,54,55}. Unsaturated lipids were reported to order in a structure with slightly larger nearest neighbour tail distances, leading to an acyl-chain correlation peak at $\sim 1.3 \text{ \AA}^{-1}$, as reported for DOPC and POPC⁵⁶, for instance. Lipids, such as Dimyristoylphosphatidylethanolamine (DMPE) and the charged DMPS (Dimyristoyl-sn-glycero-3-phosphoserine) with smaller head groups were reported to order in more densely packed structures^{57,58}. The corresponding acyl chain correlation peaks were observed at Q values of $Q \sim 1.65 \text{ \AA}^{-1}$. The observed differences in the X-ray diffraction patterns between different individuals can, therefore, most likely be assigned to differences in the molecular composition of the plasma membrane in the cell membrane complex. Genetics plays an important role in this composition.

4.2. Genetic Similarity

Some subjects have genetic relations within the subject pool. In particular, Subject 1 and 2 are daughter and father, Subjects 10 and 11 are fraternal twins, and Subjects 9 and 12 are identical twins. The corresponding diffraction data are shown in Figure 7 b), c) and d). While in general, the diffraction patterns in the membrane region were found to be different (as demonstrated in part a)), the genetically similar hair of father and daughter and identical twins show identical patterns within the resolution of our experiment.

It is interesting to note that differences are observed for the fraternal twins in part d). This finding is in agreement with the expectation that individuals with similar genetics would share similar physical traits such as hair structure. Identical or monozygotic twins originate from one zygote during embryonic development, and they share 100% of their genetic material. Fraternal or dizygotic twins develop from the fertilization of two different eggs and they only share 50% of their DNA on average⁵⁹.

As expected, the identical twin pair show almost identical hair structures whereas the fraternal pair exhibit distinct differences. Offsprings receive half of their chromosomes from each parents, thus the genetic similarity between the parent and child pair is roughly the same as fraternal twins⁶⁰. It is, therefore, surprising that the father and daughter pair share significantly more simi-

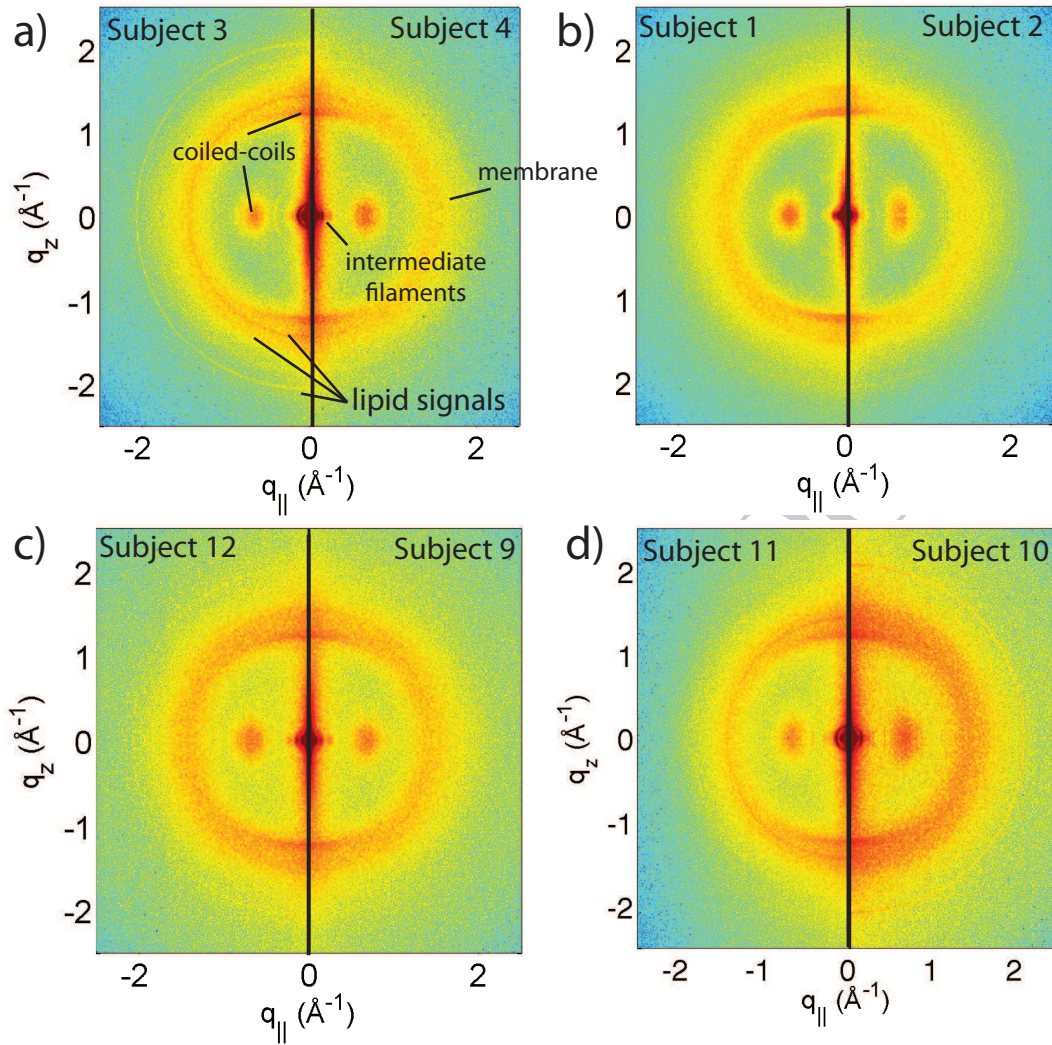


FIG. 7. Comparison between hair samples. a) shows a comparison between individuals 3 and 4. While the two specimen both show the general features, differences are observed in the region of signal from the cell membrane complex. b) Comparison between individuals 1 and 2, father and daughter. The data in c) (individuals 9 and 12) are from identical twins. Data in d) was taken from fraternal twins (individuals 10 and 11). While different individuals in general show different membrane patterns (a), features in b) and c) perfectly agree. Fraternal twins show slight differences in their pattern in d).

481 larities than the pair of fraternal twins. This can be at-
 482 tributed to the fact that the expression of a complex trait
 483 such as hair structure would depend on the inheritance
 484 pattern of many phenotype-determining genes, such as
 485 whether they are dominant or recessive traits. Genetic
 486 similarity does not guarantee identical hair structure and
 487 similarly, genetic variability does not guarantee differ-
 488 ences. While we can report this finding, the small number
 489 of related samples excludes a more detailed and quanti-

490 tative analysis of this effect at this time.

491 The comparison in Figure 7 b) between father and
 492 daughter also enables to study the effect of hair care
 493 products, such as shampoo and conditioner on the molec-
 494 ular structure of hair. While Subject 2 (father) uses soap
 495 and shower gel to clean scalp and hair, Subject 1 (daugh-
 496 ter) regularly uses shampoo and conditioner. The identi-
 497 cal X-ray signals are indicative that these products do
 498 not have an effect on the molecular structure of keratin

499 and membranes deep inside the hair (within the resolu-
500 tion of our experiment).

501 We note that in order to maximize the scattered sig-
502 nals, the entire hair strand was illuminated in our experi-
503 ments using a relatively large X-ray beam. Microbeam X-
504 ray diffraction on synchrotron sources, which uses small,
505 micrometre sized beams^{4,7,10,20,21}, gives a high spatial
506 resolution. By illuminating selective parts of the hair,
507 the occurrence of the signals that we observed can be de-
508 termined as function of their location within the hair in
509 future experiments.

510 5. CONCLUSIONS

511 We studied the molecular hair structure of several in-
512 dividuals using X-ray diffraction. Hair samples were col-
513 lected from 12 healthy individuals of various character-
514 istics, such as gender, optical appearance and genetic

515 relation. Signals corresponding to the coiled-coil phase
516 of the keratin molecules, the formation of intermediate
517 filaments in the *cortex* and from lipid molecules in the
518 cell membrane complex were observed in the experiment.
519 The corresponding signals were observed in all individ-
520 uals, independent of gender or appearance of the hair,
521 such as colour or waviness within the resolution of this
522 experiment. Given the small standard deviation of the
523 molecular dimensions of these general features, anom-
524 alies possibly related to certain diseases should be easy to
525 detect.

526 While all hair samples showed these general features,
527 differences between individuals were observed in the com-
528 position of the plasma membrane in the cell membrane
529 complex. Genetics seems to play an important role in
530 the properties of these membranes, as genetically simi-
531 lar hair samples from father and daughter and identical
532 twins showed identical patterns, however not hair from
533 fraternal twins.

-
- 534 ¹ Clarence R Robbins, *Chemical and Physical Behavior of*
535 *Human Hair*, 5th ed. (New York: Springer, New York,
536 2012).
- 537 ² RD Fraser, Thomas P MacRae, DA Parry, and Eikichi
538 Suzuki, "Intermediate filaments in alpha-keratins," Pro-
539 ceedings of the National Academy of Sciences **83**, 1179–
540 1183 (1986).
- 541 ³ F Briki, B Busson, L Kreplak, P Dumas, and J Doucet,
542 "Exploring a biological tissue from atomic to macroscopic
543 scale using synchrotron radiation: Example of hair," Cel-
544 lular and Molecular Biology **46**, 1005–1016 (2000).
- 545 ⁴ B Busson, P Engstrom, and J Doucet, "Existence of var-
546 ious structural zones in keratinous tissues revealed by x-
547 ray microdiffraction," Journal of Synchrotron Radiation **6**,
548 1021–1030 (1999).
- 549 ⁵ Rudolf Randebrock, "Neue erkenntnisse über den morphol-
550 ogischen aufbau des menschlichen haares," J. Soc. Cosmet.
551 Chem **15**, 691–706 (1964).
- 552 ⁶ RD Fraser, TP MacRae, and GE Rogers, "Molecular orga-
553 nization in alpha-keratin," Nature **193**, 1052–1055 (1962).
- 554 ⁷ L. Kreplak, C. Mérigoux, F. Briki, D. Flot, and J. Doucet,
555 "Investigation of human hair cuticle structure by microd-
556 iffraction: direct observation of cell membrane complex
557 swelling," Biochimica et Biophysica Acta (BBA) - Pro-
558 tein Structure and Molecular Enzymology **1547**, 268 – 274
559 (2001).
- 560 ⁸ Krystyna E Wilk, Veronica J James, and Yoshiyuki
561 Amemiya, "The intermediate filament structure of human
562 hair," Biochimica et Biophysica Acta (BBA)-General Sub-
563 jects **1245**, 392–396 (1995).
- 564 ⁹ Linus Pauling and Robert B Corey, "The structure of hair,
565 muscle, and related proteins," Proc Natl Acad Sci USA **37**,
566 261–271 (1951).
- 567 ¹⁰ Noboru Ohta, Toshihiko Oka, Katsuaki Inoue, Naoto Yagi,
568 Satoru Kato, and Ichiro Hatta, "Structural analysis of cell
569 membrane complex of a hair fibre by micro-beam x-ray
570 diffraction," Journal of applied crystallography **38**, 274–
571 279 (2005).
- 572 ¹¹ WT Astbury and A Street, "X-ray studies of the structure
573 of hair, wool, and related fibres. i. general," Philosophi-
574 cal Transactions of the Royal Society of London. Series A,
575 Containing Papers of a Mathematical or Physical Charac-
576 ter, 75–101 (1932).
- 577 ¹² WT Astbury and HJ Woods, "X-ray studies of the struc-
578 ture of hair, wool, and related fibres. ii. the molecular
579 structure and elastic properties of hair keratin," Philosoph-
580 ical Transactions of the Royal Society of London. Series A,
581 Containing Papers of a Mathematical or Physical Charac-
582 ter, 333–394 (1934).
- 583 ¹³ WT Astbury and Wayne A Sisson, "X-ray studies of the
584 structure of hair, wool, and related fibres. iii. the config-
585 uration of the keratin molecule and its orientation in the
586 biological cell," Proceedings of the Royal Society of Lon-
587 don. Series A, Mathematical and Physical Sciences **150**,
588 533–551 (1935).
- 589 ¹⁴ A Franbourg, P Hallegot, F Baltenneck, C Toutaina, and
590 F Leroy, "Current research on ethnic hair," Journal of the
591 American Academy of Dermatology **48**, S115–S119 (2003).
- 592 ¹⁵ Mériem Er Rafik, Jean Doucet, and Fatma Briki, "The
593 intermediate filament architecture as determined by x-ray
594 diffraction modeling of hard α -keratin," Biophysical Jour-
595 nal **86**, 3893 – 3904 (2004).
- 596 ¹⁶ Veronica James, John Kearsley, Tom Irving, Yoshiyuki
597 Amemiya, and David Cookson, "Using hair to screen for
598 breast cancer," Nature **398**, 33–34 (1999).
- 599 ¹⁷ Veronica J James and Yoshiyuki Amemiya, "Intermediate
600 filament packing in α -keratin of echidna quill," Textile re-
601 search journal **68**, 167–170 (1998).
- 602 ¹⁸ Fatma Briki, Bertrand Busson, Bruno Salicru, François
603 Estève, and Jean Doucet, "Breast-cancer diagnosis using
604 hair," Nature **400**, 226–226 (1999).
- 605 ¹⁹ Veronica James, "The importance of good images in us-
606 ing hair to screen for breast cancer," Journal of medical
607 genetics **38**, e16 (2001).
- 608 ²⁰ Atsuo Iida and Takashi Noma, "Synchrotron x-ray
609 muprobe and its application to human hair analysis," Nu-

- clear Instruments and Methods in Physics Research Section B: Beam Interactions with Materials and Atoms **82**, 129–138 (1993).
- ²¹ Yoshio Kajiuura, Shunichi Watanabe, Takashi Itou, Koichi Nakamura, Atsuo Iida, Katsuaki Inoue, Naoto Yagi, Yuya Shinohara, and Yoshiyuki Amemiya, “Structural analysis of human hair single fibres by scanning microbeam saxs,” *Journal of structural biology* **155**, 438–444 (2006).
- ²² Bruce O Berg, Sidney H Rosenberg, and Arthur K Asbury, “Giant axonal neuropathy,” *Pediatrics* **49**, 894–899 (1972).
- ²³ JA Swift and JR Smith, “Microscopical investigations on the epicuticle of mammalian keratin fibres,” *Journal of microscopy* **204**, 203–211 (2001).
- ²⁴ RJ Randebrook, “Neue erkenntnisse über den morphologischen aufbau des menschlichen haares,” *J. Soc. Cosmet. Chem* **15**, 691–706 (1964).
- ²⁵ EH Mercer, “The heterogeneity of the keratin fibers,” *Textile Research Journal* **23**, 388–397 (1953).
- ²⁶ Linus Pauling and Robert B Corey, “Two hydrogen-bonded spiral configurations of the polypeptide chain,” *Journal of the American Chemical Society* **72**, 5349–5349 (1950).
- ²⁷ WG Crewther, LM Dowling, PM Steinert, and DAD Parry, “Structure of intermediate filaments,” *International Journal of Biological Macromolecules* **5**, 267–274 (1983).
- ²⁸ RDB Fraser, Thomas P MacRae, Lindsay G Sparrow, and DAD Parry, “Disulphide bonding in α -keratin,” *International Journal of Biological Macromolecules* **10**, 106–112 (1988).
- ²⁹ GE Rogers, “Electron microscopy of wool,” *Journal of ultrastructure research* **2**, 309–330 (1959).
- ³⁰ Wilfred H Ward and Harold P Lundgren, “The formation, composition, and properties of the keratins,” *Advances in protein chemistry* **9**, 243–297 (1954).
- ³¹ Nicole Pinto, Fei-Chi Yang, Atsuko Negishi, Maikel C. Rheinstädter, Todd E. Gillis, and Douglas S. Fudge, “Self-assembly enhances the strength of fibers made from vimentin intermediate filament proteins,” *Biomacromolecules* **15**, 574–581 (2014).
- ³² Fei-Chi Yang, Robert D. Peters, Hannah Dies, and Maikel C. Rheinstädter, “Hierarchical, self-similar structure in native squid pen,” *Soft Matter* **10**, 5541–5549 (2014).
- ³³ FHC Crick, “Is α -keratin a coiled coil?” *Nature* **170**, 882–883 (1952).
- ³⁴ C Cohen and DA Parry, “Alpha-helical coiled coils: more facts and better predictions,” *Science* **263**, 488–489 (1994), <http://www.sciencemag.org/content/263/5146/488.full.pdf>.
- ³⁵ Andrei N Lupas and Markus Gruber, “The structure of α -helical coiled coils,” *Advances in protein chemistry* **70**, 37–38 (2005).
- ³⁶ Anthony Howell, J Günter Grossmann, Kan C Cheung, Lalji Kanbi, R Evans D Gareth, and S Samar Hasnain, “Can hair be used to screen for breast cancer?” *Journal of medical genetics* **37**, 297–298 (2000).
- ³⁷ L Kreplak, F Briki, Y Duvault, J Doucet, C Merigoux, F Leroy, JL Lévêque, L Miller, GL Carr, GP Williams, *et al.*, “Profiling lipids across caucasian and afro-american hair transverse cuts, using synchrotron infrared microspectrometry,” *International journal of cosmetic science* **23**, 369–374 (2001).
- ³⁸ Fabienne Furt, Françoise Simon-Plas, and Sébastien Mongrand, “The plant plasma membrane,” in *The Plant Plasma Membrane*, Plant Cell Monographs, Vol. 19 (Springer US, 2011) Chap. Lipids of the Plant Plasma Membrane, pp. 57–85.
- ³⁹ Norbert Kucerka, Yufeng Liu, Nanjun Chu, Horia I. Petrache, Stephanie Tristram-Nagle, and John F. Nagle, “Structure of fully hydrated fluid phase DMPC and DLPC lipid bilayers using x-ray scattering from oriented multilamellar arrays and from unilamellar vesicles,” *Biophys. J.* **88**, 2626–2637 (2005).
- ⁴⁰ Horia I. Petrache, Nikolai Gouliavov, Stephanie Tristram-Nagle, Ruitian Zhang, Robert M. Suter, and John F. Nagle, “Interbilayer interactions from high-resolution x-ray scattering,” *Phys. Rev. E* **57**, 7014–7024 (1998).
- ⁴¹ Norbert Kučerka, Stephanie Tristram-Nagle, and John F. Nagle, “Closer look at structure of fully hydrated fluid phase dppc bilayers,” *Biophysical Journal* **90**, L83–L85 (2006).
- ⁴² M. C. Rheinstädter, C. Ollinger, G. Fragneto, F. Demmel, and T. Salditt, “Collective dynamics of lipid membranes studied by inelastic neutron scattering,” *Phys. Rev. Lett.* **93**, 108107 (2004).
- ⁴³ Maikel C. Rheinstädter, Tilo Seydel, and Tim Salditt, “Nanosecond molecular relaxations in lipid bilayers studied by high energy resolution neutron scattering and in-situ diffraction,” *Phys. Rev. E* **75**, 011907 (2007).
- ⁴⁴ Maikel C. Rheinstädter, Jhuma Das, Elijah J. Flenner, Beate Brüning, Tilo Seydel, and Ioan Kosztin, “Motional coherence in fluid phospholipid membranes,” *Phys. Rev. Lett.* **101**, 248106 (2008).
- ⁴⁵ Jianjun Pan, Thalia T. Mills, Stephanie Tristram-Nagle, and John F. Nagle, “Cholesterol perturbs lipid bilayers nonuniversally,” *Phys. Rev. Lett.* **100**, 198103 (2008).
- ⁴⁶ Philipp Schneggenburger, Andr Beerlink, Britta Weinhäusen, Tim Salditt, and Ulf Diederichsen, “Peptide model helices in lipid membranes: insertion, positioning, and lipid response on aggregation studied by x-ray scattering,” *European Biophysics Journal* **40**, 417–436 (2011).
- ⁴⁷ Thad A. Harroun, William T. Heller, Thomas M. Weiss, Lin Yang, and Huey W. Huang, “Experimental evidence for hydrophobic matching and membranemediated interactions in lipid bilayers containing gramicidin,” *Biophysical Journal* **76**, 937945 (1999).
- ⁴⁸ R. Welti, D.A. Rintoul, F. Goodsaid-Zalduondo, S. Felder, and D.F. Silbert, “Gel-phase phospholipid in the plasma membrane of sterol-depleted mouse lm cells,” *The Journal of Biological Chemistry* **256**, 7528–7535 (1981).
- ⁴⁹ Danny Poinapen, Laura Toppozini, Hannah Dies, Daniel C. W. Brown, and Maikel C. Rheinstädter, “Static magnetic fields enhance lipid order in native plant plasma membrane,” *Soft Matter* **9**, 6804–6813 (2013).
- ⁵⁰ Clare L. Armstrong, Drew Marquardt, Hannah Dies, Norbert Kučerka, Zahra Yamani, Thad A. Harroun, John Katsaras, An-Chang Shi, and Maikel C. Rheinstädter, “The observation of highly ordered domains in membranes with cholesterol,” *PLOS ONE* **8**, e66162 (2013).
- ⁵¹ Thalia T. Mills, Gilman E. S. Toombes, Stephanie Tristram-Nagle, Detlef-M. Smilgies, Gerald W. Feigenson, and John F. Nagle, “Order parameters and areas in fluid-phase oriented lipid membranes using wide angle x-ray scattering,” *Biophysical Journal* **95**, 669–681 (2008).
- ⁵² Matthew A. Barrett, Songbo Zheng, Gohnaz Roshankar, Richard J. Alsop, Randy K.R. Belanger, Chris Huynh, Norbert Kučerka, and Maikel C. Rheinstädter, “Interaction of aspirin (acetylsalicylic acid) with lipid membranes,” *PLoS ONE* **7**, e34357 (2012).

- ⁷³⁸ ⁵³ M.A. Barrett, S. Zheng, L.A. Toppozini, R.J. Alsop, ⁷⁵⁴
⁷³⁹ H. Dies, A. Wang, N. Jago, M Moore, and M.C. Rhe- ⁷⁵⁵
⁷⁴⁰ instädter, "Solubility of cholesterol in lipid membranes and ⁷⁵⁶
⁷⁴¹ the formation of immiscible cholesterol plaques at high ⁷⁵⁷
⁷⁴² cholesterol concentrations," *Soft Matter* **9**, 9342 – 9351 ⁷⁵⁸
⁷⁴³ (2013). ⁷⁵⁹
- ⁷⁴⁴ ⁵⁴ Stephanie Tristram-Nagle, Yufeng Liu, Justin Legleiter, ⁷⁶⁰
⁷⁴⁵ and John F. Nagle, "Structure of gel phase dmpe determined by x-ray diffraction," *Biophysical Journal* **83**, 3324– ⁷⁶¹
⁷⁴⁶ 3335 (2002). ⁷⁶²
- ⁷⁴⁷ ⁵⁵ J. Katsaras, V. A. Raghunathan, E. J. Dufourc, and J. Du- ⁷⁶³
⁷⁴⁸ fourcq, "Evidence for a two-dimensional molecular lattice ⁷⁶⁴
⁷⁴⁹ in subgel phase dppc bilayers," *Biochemistry* **34**, 4684– ⁷⁶⁵
⁷⁵⁰ 4688 (1995). ⁷⁶⁶
- ⁷⁵¹ ⁵⁶ T.T. Mills, J. Huang, G.W. Feigenson, and J.F. Nagle, ⁷⁶⁷
⁷⁵² "Effects of cholesterol and unsaturated dopc lipid on chain ⁷⁶⁸
⁷⁵³ packing of saturated gel-phase dppc bilayers," *Gen Physiol* ⁷⁶⁹
Biophys. **28**, 126–139 (2009). ⁷⁷⁰
- ⁷⁷¹ ⁵⁷ Michael Rappolt and Gert Rapp, "Simultaneous small- and ⁷⁷²
⁷⁷³ wide-angle x-ray diffraction during the main transition of ⁷⁷⁴
⁷⁷⁵ dimyristoylphosphatidylethanolamine," *Biophysical Journal* **86**, 15741586 (2004). ⁷⁷⁶
- ⁷⁷⁷ ⁵⁸ Michael Rappolt and Gert Rapp, "Simultaneous small- ⁷⁷⁸
⁷⁷⁹ and wide-angle x-ray diffraction during the main transition ⁷⁸⁰
⁷⁸¹ of dimyristoylphosphatidylethanolamine," *Ber. Bunsenges.* ⁷⁸²
Phys. Chem. **7**, 1153–1162 (1996). ⁷⁸³
- ⁷⁸⁴ ⁵⁹ Robert Nussbaum, Roderick R McInnes, and Hunt- ⁷⁸⁵
⁷⁸⁶ ington F Willard, *Thompson & Thompson genetics in* ⁷⁸⁷
medicine (Elsevier Health Sciences, 2007). ⁷⁸⁸
- ⁷⁸⁹ ⁶⁰ Robert K, Robert Resnik, and Jay D Iams, eds., *Maternal-* ⁷⁹⁰
fetal medicine: principles and practice (WB Saunders, ⁷⁹¹
1984). ⁷⁹²

Chapter 6

Appendix

6.1 Paper IV: Probing the Internal Morphology of Injectable Poly(oligoethylene glycol methacrylate) Hydrogels by Light and Small-Angle Neutron Scattering

Niels M.B. Smeets, Emilia Bakaic, Francis M. Yavitt, Fei-Chi Yang, Maikel C. Rheinstädter and Todd Hoare. “*Probing the Internal Morphology of Injectable Poly(oligoethylene glycol methacrylate) Hydrogels by Light and Small-Angle Neutron Scattering*”, *Macromolecules*, 2014, 47 (17), 6017–6027

Author Contributions

- *Experiment Design*: Niels M.B., Todd Hoare, and Maikel C. Rheinstädter
- *Sample Fabrication*: Niels M.B., Emilia Bakaic and Francis M. Yavitt

-
- *Neutron Experiment Performing:* Emilia Bakaic, Francis M. Yavitt, and **Fei-Chi Yang**
 - *Light Scattering Experiment Performing:* **Fei-Chi Yang** and Maikel C. Rheinstädter
 - *Data Analysis:* Niels M.B. Smeets and **Fei-Chi Yang**
 - *Manuscript Writing:* Niels M.B. Smeets, Emilia Bakaic, Francis M. Yavitt, **Fei-Chi Yang**, Maikel C. Rheinstädter and Todd Hoare

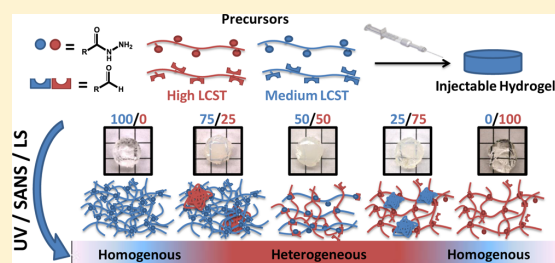
Probing the Internal Morphology of Injectable Poly(oligoethylene glycol methacrylate) Hydrogels by Light and Small-Angle Neutron Scattering

Niels M. B. Smeets,[†] Emilia Bakaic,[†] Francis M. Yavitt,[†] Fei-Chi Yang,[‡] Maikel C. Rheinstädter,[‡] and Todd Hoare^{*,†}

[†]Department of Chemical Engineering and [‡]Department of Physics and Astronomy, McMaster University, 1280 Main Street West, Hamilton, Ontario, Canada L8S 4L8

Supporting Information

ABSTRACT: While injectable, *in situ* gelling hydrogels have attracted increasing attention in the biomedical literature due to their minimally invasive administration potential, little is known about the internal morphology of these hydrogels and thus how to engineer precursor polymer compositions to achieve desired hydrogel properties. In this paper, the internal morphology of injectable *in situ* gelling hydrogels based on hydrazide and aldehyde-functionalized poly(oligoethylene glycol methacrylate) precursors with varying lower critical solution temperatures (LCSTs) is investigated using a combination of spectrophotometry, small-angle neutron scattering, and light scattering. If two precursor polymers with similar LCSTs are used to prepare the hydrogel, relatively homogeneous hydrogels are produced (analogous to conventional step-growth polymerized hydrogels); this result is observed provided that gelation is sufficiently slow for diffusional mixing to compensate for any incomplete mechanical mixing in the double-barrel syringe and the volume phase transition temperature (VPTT) of the hydrogel is sufficiently high that phase separation does not occur on the time scale of gelation. Hydrogels prepared from precursor polymers with different LCSTs (1 polymer/barrel) also retain transparency, although their internal morphology is significantly less homogeneous. However, if functionalized polymers with different LCSTs are mixed in each barrel (i.e., 2 polymers/barrel, such that a gelling pair of precursors with both low and high LCSTs is present), opaque hydrogels are produced that contain significant inhomogeneities that are enhanced as the temperature is increased; this suggests phase separation of the hydrogel into lower and higher LCST domains. Based on this work, the internal morphology of injectable hydrogels can be tuned by engineering the gelation time and the physical properties (i.e., miscibility) of the precursor polymers, insight that can be applied to improve the design of such hydrogels for biomedical applications.



INTRODUCTION

The success of hydrogels as soft synthetic materials for controlled release and cell scaffolding applications^{1–4} can be attributed to high water content, controllable porosity, and mechanical and (if desired) compositional similarity of hydrogels to native tissues.⁵ While various methods of gelation (e.g., physical, electrostatic, or chemical) exist for the fabrication of hydrogels, chemical (or covalent) cross-linking is generally preferred as it results in hydrogels with controllable stability under a variety of environmental conditions. The macroscopic properties of bulk hydrogels are largely governed by the homogeneity of the polymer network and can be significantly affected by cross-link inhomogeneities introduced during hydrogel formation. Depending on the target application, the presence of inhomogeneities in hydrogels may help (i.e., by providing domains of distinct compositions for loading and release applications) or hinder (i.e., by making hydrogels opaque or mechanically weaker) their ultimate use. A

fundamental understanding of network homogeneity is therefore very important to fully understand the relationship between the hydrogel nanostructure and the macroscopic properties.⁶

Scattering methods, such as light scattering (LS) and small-angle neutron scattering (SANS), have been widely applied to probe the micro- and nanostructure of polymeric systems, including hydrogels.⁷ In a hydrogel system, SANS allows for the determination of the mesh size (ξ) of the hydrogel network and characteristic size of inhomogeneities (Ξ) (or “blobs”) formed as a result of nonideal cross-linking. Covalently cross-linked hydrogels fabricated via chain growth gelation (e.g., UV photopolymerization of vinyl monomers) generally give inhomogeneous hydrogels,⁸ while chain growth polymerization

Received: June 7, 2014

Revised: August 4, 2014

Table 1. Composition of the Various POEGMA Hydrogels^a

	hydrazide barrel			aldehyde barrel		
	PO ₀ H ₃₀ [mg/mL]	PO ₁₀ H ₃₀ [mg/mL]	PO ₁₀₀ H ₃₀ [mg/mL]	PO ₀ A ₃₀ [mg/mL]	PO ₁₀ A ₃₀ [mg/mL]	PO ₁₀₀ A ₃₀ [mg/mL]
PO ₀	150.0			150.0		
PO ₁₀ = PO(100/0)		150.0			150.0	
PO(75/25)		112.5	37.5		112.5	37.5
PO(50/50)		75.0	75.0		75.0	75.0
PO(25/75)		37.5	112.5		37.5	112.5
PO ₁₀₀ = PO(0/100)			150.0			150.0
PO ₁₀ H ₃₀ + PO ₁₀₀ A ₃₀		150.0				150.0
PO ₁₀₀ H ₃₀ + PO ₁₀ A ₃₀			150.0		150.0	

^aAll precursor solutions are prepared at 150 mg/mL in 10 mM PBS prior to mixing.

(e.g., mixing of complementary reactive polymeric precursors) has been demonstrated to generally yield more homogeneous hydrogels with fewer structural defects.⁹ As a particularly relevant example of the latter, Matsunaga⁶ demonstrated that a step growth hydrogel prepared from amine and succinimidyl ester functionalized 4-arm poly(ethylene glycol) (PEG) resulted in an extremely uniform hydrogel network without any detectable defects due to cross-linking inhomogeneities. Gelation in the case of injectable, *in situ* gelling hydrogels, in which a hydrogel is rapidly formed following *in situ* mixing of reactive polymers with complementary functional groups,¹⁰ offers additional levels of complexity that may promote the formation of inhomogeneous domains in hydrogels. The rate and magnitude of polymer–polymer cross-linking in such systems are expected to be strongly dependent on not only the degree of functionalization of the pregel polymers but also the mixing and subsequent diffusion and/or phase separation of the reactive precursor polymers. The net effect of these competing processes has not been broadly investigated in the literature but is essential to understand to rationally engineer such *in situ* gelling hydrogels for biomedical applications.

We have recently reported the synthesis as well as physicochemical and biological properties of injectable poly-(oligoethylene glycol methacrylate) (POEGMA) hydrogels.^{11,12} Our approach is based on the rapid cross-linking of complementary reactive POEGMA precursors exploiting hydrazide–aldehyde chemistry.^{13–20} On a macroscopic scale, the gelation kinetics, swelling, and mechanical properties of these POEGMA hydrogels depend strongly on the lower critical solution temperature (LCST) of the precursors,¹¹ which can be precisely tuned according to the statistical copolymerization of oligo(ethylene glycol) methacrylate (OEGMA) monomers with different ethylene oxide side chain lengths ($n = 2$ and $n = 8, 9$).^{21,22} Substantial differences are observed in the physical properties of the hydrogels prepared with precursors with different LCST values despite the similarity in the theoretical cross-link density in each hydrogel, suggesting substantial differences in the structural homogeneity of the hydrogel network formed during gelation.

Herein, we aim to study in detail the nanostructure of injectable, thermoresponsive POEGMA hydrogels based on precursor polymers of different LCST values using SANS and LS. SANS and LS have been applied previously to characterize the structural changes in temperature responsive hydrogels based on (co)polymerization of *N*-isopropylacrylamide (PNIPAM)^{23,24} (i.e., chain growth), indicating formation of microphase separated domains prior to the macroscopic phase transition.^{23,24} However, to this point, there is no report investigating the microstructure of *in situ* gelling hydrogels from

polymeric precursors or, more specifically, thermoresponsive *in situ* gelling hydrogels, despite the clinical relevance of such materials. We specifically aim to investigate the range of hydrogel morphologies that can be generated using precursor polymers with similar LCST values and/or divergent LCST values; in the latter case, the potential for phase separation on the time scale of gelation has the potential to yield particularly useful and novel morphologies of potential relevance for drug delivery or tissue engineering applications.

EXPERIMENTAL SECTION

Materials. Di(ethylene glycol) methyl ether methacrylate (M(EO)₂MA, Sigma-Aldrich, 95%) and oligo(ethylene glycol) methyl ether methacrylate with an average number-average molecular weight of 475 g mol⁻¹ (OEGMA₄₇₅, Sigma-Aldrich, 95%) were purified by passing the monomers over a column of basic aluminum oxide (Sigma-Aldrich, type CG-20) to remove inhibitors. *N*-(2,2-Dimethoxyethyl)-methacrylamide (DMAEM) was synthesized according to a previously reported procedure.¹¹ Acrylic acid (AA, Sigma-Aldrich, 99%), adipic acid dihydrazide (ADH, Alfa Aesar, 98%), *N*'-ethyl-*N*-(3-(dimethylamino)propyl)carbodiimide (EDC, Carbosynth, Compton CA, commercial grade), thioglycolic acid (TGA, Sigma-Aldrich, 98%), and 2,2-azobisisobutyric acid dimethyl ester (AIBME, Wako Chemicals, 98.5%) were used as received. For all experiments, Milli-Q grade distilled deionized water (DIW) was used.

Synthesis of Hydrazide-Functionalized Precursors (POH). Hydrazide-functionalized POEGMA precursors were synthesized as described previously.¹¹ Briefly, AIBME, M(EO)₂MA, OEGMA₄₇₅, AA (0.36 g, 5.0 mmol), and TGA were dissolved in 1,4-dioxane. After purging for at least 30 min, the flask was sealed and submerged in a preheated oil bath at 75 °C for 4 h under magnetic stirring. The solvent was removed, and the polymer was modified with a large excess of adipic acid dihydrazide. The hydrazide functionalized polymer was purified by dialysis and lyophilized. The polymers were stored as 20% w/w solutions in PBS at 4 °C. The hydrazide-functionalized precursors are labeled as PO_{*x*}H_{*y*}, where *x* denotes the mole fraction of OEGMA₄₇₅ among the OEGMA monomers used (the remainder being M(EO)₂MA) and *y* denotes the overall mole fraction of AA (among all comonomers) in the synthesis recipe.

Synthesis of Aldehyde-Functionalized Precursors (POA). Aldehyde-functionalized POEGMA precursors were synthesized as described previously.¹¹ Briefly, AIBME, M(EO)₂MA, OEGMA₄₇₅, DMEMAm, and TGA were dissolved in 1,4-dioxane. After purging for at least 30 min, the flask was sealed and submerged in a preheated oil bath at 75 °C for 4 h under magnetic stirring. The solvent was then removed, and the acetal was cleaved in 0.5 M hydrochloric acid to generate the aldehyde group. The resulting aldehyde functionalized polymer was purified by dialysis and lyophilized. The polymers were stored as 20% w/w solutions in PBS at 4 °C. The aldehyde-functionalized precursors are labeled as PO_{*x*}A_{*y*}, where *x* denotes the mole fraction of OEGMA₄₇₅ among the OEGMA monomers used (the remainder being M(EO)₂MA) and *y* denotes the overall mole fraction of DMEMAm (among all comonomers) in the synthesis recipe.

Chemical Characterization. Aqueous size exclusion chromatography (SEC) was performed using a Waters 515 HPLC pump, a Waters 717 Plus autosampler, three Ultrahydrogel columns (30 cm \times 7.8 mm i.d.; exclusion limits: 0–3, 0–50, and 2–300 kDa), and a Waters 2414 refractive index detector. A mobile phase consisting of 0.3 M sodium nitrate and 0.05 M phosphate buffer (pH 7) at a flow rate of 0.8 mL/min was used for all polymers analyzed, and the system was calibrated with narrow-dispersed poly(ethylene glycol) standards ranging from 106 to 584×10^3 g/mol (Waters). ^1H NMR was performed using a Bruker AVANCE 600 MHz spectrometer and deuterated chloroform as the solvent. The acrylic acid content of the polymers was determined with conductometric titration (ManTech Associates), using 50 mg of polymer dissolved in 50 mL of 1 mM NaCl as the analysis sample and 0.1 M NaOH as the titrant. A Variant Cary Bio 100 UV–vis spectrophotometer was used to measure the LCST (defined as 95% transmittance) of the polymer precursor chains. The polymers were dissolved at a concentration of 1 mg/mL in PBS (pH = 7.4), and the absorbance of the polymer solution was recorded at 500 nm at every 0.5 $^\circ\text{C}$ over a temperature range of 10–80 $^\circ\text{C}$, with the temperature ramped at a rate of 1 $^\circ\text{C}/\text{min}$.

Hydrogel Preparation. Hydrogels were prepared by coextruding one or more hydrazide-functionalized precursor(s) (among PO_0H_{30} , $\text{PO}_{10}\text{H}_{30}$, and $\text{PO}_{100}\text{H}_{30}$) with one or more aldehyde-functionalized precursor(s) (among PO_0A_{30} , $\text{PO}_{10}\text{A}_{30}$, and $\text{PO}_{100}\text{A}_{30}$) using a double-barrel syringe (Medmix). Table 1 provides a complete summary of the hydrogel recipes evaluated.

Hydrogels were prepared by coextruding (i) precursors of similar LCST ($\text{PO}_0 = \text{PO}_0\text{H}_{30} + \text{PO}_0\text{A}_{30}$; $\text{PO}_{10} = \text{PO}_{10}\text{H}_{30} + \text{PO}_{10}\text{A}_{30}$; $\text{PO}_{100} = \text{PO}_{100}\text{H}_{30} + \text{PO}_{100}\text{A}_{30}$), (ii) precursors with different LCSTs in each barrel (i.e., $\text{PO}_{10}\text{H}_{30} + \text{PO}_{100}\text{A}_{30}$ and $\text{PO}_{100}\text{H}_{30} + \text{PO}_{10}\text{A}_{30}$), or (iii) mixed precursors of different LCSTs in different weight ratios ($\text{PO}(75/25)$, $\text{PO}(50/50)$, and $\text{PO}(25/75)$). This latter group of hydrogels was prepared in a similar manner as the PO_{10} and PO_{100} hydrogels; however, precursor solutions were prepared by mixing both high LCST and low LCST precursor polymers in both the hydrazide ($\text{PO}_{10}\text{H}_{30}$ and $\text{PO}_{100}\text{H}_{30}$) and aldehyde ($\text{PO}_{10}\text{A}_{30}$ and $\text{PO}_{100}\text{A}_{30}$) barrels of the double-barrel syringe at a total concentration of 150 mg/mL in the mass ratios indicated by the hydrogel sample codes. As such, each mixed precursor hydrogel is prepared with four precursor polymers (2 hydrazide-functionalized and 2 aldehyde-functionalized) while all other hydrogels studied are prepared by mixing only two precursor polymers (1 hydrazide-functionalized and 1 aldehyde-functionalized).

Gelation Kinetics. The transmittance of the hydrogels was tracked during the gelation process using a Cary 300 UV–vis spectrophotometer with the Kinetics Software (version 3.0). The polymer precursor solutions (500 μL at 150 mg/mL) were coextruded into a polystyrene cuvette, and the absorbance was tracked at a wavelength of 500 nm with an average sample time of 0.1 s and cycle time of 0.25 min. All experiments were performed with the Peltier unit set at 37 $^\circ\text{C}$ to maintain constant temperature mimicking physiological injection.

Phase Transition of the Hydrogels. The volume phase transition temperature of the hydrogels (300 μL) was determined gravimetrically. Hydrogel disks were prepared by extruding the reactive polymer precursors through the double-barrel syringe into cylindrical silicone rubber molds (diameter = 7 mm, volume = 300 μL). Hydrogels were placed inside scintillation vials filled with 12 mL of 10 mM PBS and submerged into a thermostated water bath. After a 12 h incubation period to ensure complete gelation, the hydrogels were gently dried using a Kimwipe to remove nonabsorbed PBS and weighed. A fresh aliquot of PBS was then added, the temperature of the water bath increased by 5 $^\circ\text{C}$, and the process was repeated. The mass loss of the hydrogels was calculated by comparing the mass of the hydrogel at any given temperature to the initial mass of the same hydrogel, as measured at 22.5 $^\circ\text{C}$ (room temperature). All experiments were performed in triplicate, with reported error bars representing the standard error of the repeat measurements.

Small-Angle Neutron Scattering (SANS). SANS experiments were conducted using the 30 m SANS NG3 at the NIST Center for Neutron Research (NCNR, Gaithersburg, MD). The sample-to-

detector distances were 1, 4, and 13 m (with and without lenses), using neutron wavelengths of 6 \AA for the first three configurations and 8.4 \AA for the 13 m lensed distance. The wavelength spread was 13%. All precursor polymers for SANS experiments were dissolved at a total concentration of 150 mg/mL in 10 mM phosphate buffered D_2O to facilitate neutron scattering contrast. Hydrogels were subsequently extruded from a double-barrel syringe into a demountable $4.32 \times 3.49 \times 2.16$ cm³ sample cell (titanium body and quartz windows) provided by NCNR and set to an internal gap thickness of 1 mm, requiring ~ 300 μL of hydrogel. Polymers extruded into sample cells were left to completely gel for 12 h before measurements were performed. The low q range data were acquired by counting for 15 min using the 13 m detection distance followed by 20 min using the 13 m distance with lens. The medium q range was collected using a 4 m detection distance counting for 5 min. The high q range was collected using a 1 m detection distance counting for 2 min. The four ranges of data collected were then merged using the DAVE on-site data reduction tool.

Light Scattering (LS). The light scattering experiment was conducted using a 5 mW laser diode operating at a wavelength of 532 ± 10 nm. Scattered light was detected using a Thorlabs DET10A Si biased detector sensitive to wavelengths from 200 to 1100 nm. Hydrogel precursors dissolved at 150 mg/mL in 10 mM PBS were extruded directly into standard 1 cm \times 1 cm quartz cuvettes to a total volume of 1.2 mL, yielding a typical beam size of 1.5 mm, sample thickness of 10 mm, and sample height of 2 mm. The detector was mounted on a motor-controlled Huber diffractometer with a laser-to-sample distance of 40 cm and sample-to-detector distance of 35 cm. Motor positions were controlled to precision of at least 0.01 $^\circ$. A detector angle (2θ) range of -60° to 60° was scanned, with the scattered light intensity recorded. This angular range was determined in test experiments to cover the experimental features, as will be shown below. A typical experimental run required approximately 160 min to collect data over the full angular range.

THEORY

The scattering intensity ($I(q)$) homogeneity of hydrogel networks has been described by eq 1, a summation of dynamic (or fluid-like) fluctuations represented by an Ornstein–Zernike function ($I_{\text{OZ}}(q)$, eq 2)²⁵ and static (or solid-like) fluctuations represented by a squared Lorentzian function ($I_{\text{SL}}(q)$, eq 3).^{7,24}

$$I(q) = \frac{\Delta\rho^2 RT\phi^2}{N_A M_{\text{OS}}} \left[\frac{I_{\text{OZ}}(0)}{1 + \xi^2 q^2} + \frac{I_{\text{SL}}(0)}{(1 + \Xi^2 q^2)^2} \right] \quad (1)$$

$$G(q) \sim I_{\text{OZ}}(q) = \frac{I_{\text{OZ}}(0)}{1 + \xi^2 q^2} \quad (\text{Ornstein–Zernike}) \quad (2)$$

$$C(q) \sim I_{\text{SL}}(q) = \frac{I_{\text{SL}}(0)}{(1 + \Xi^2 q^2)^2} \quad (\text{squared Lorentzian}) \quad (3)$$

In eqs 1–3, q is the scattering vector, $\Delta\rho^2$ the scattering length density difference squared, ϕ the volume fraction of the solute, N_A Avogadro's number, R the universal gas constant, T the temperature, M_{OS} the osmotic modulus, ξ the correlation length, and Ξ the characteristic size of inhomogeneities. The key parameters yielding insight into the hydrogel morphology are the ξ , the correlation length (or mesh size) of the network, and Ξ , the characteristic size of the inhomogeneities (or “blobs”) formed as a result of cross-linking. The latter can also be expressed in terms of a radius of gyration of the polymer rich/poor domains ($R_g = 3^{0.5}\Xi$). In the case of an ideal hydrogel network, $I(q)$ can be described by the dynamic fluctuations only, as was demonstrated experimentally for the 4-arm tetra-poly(ethylene glycol) hydrogel network discussed in the

Table 2. Chemical Characterization of Synthesized POEGMA Polymer Precursors

	M(EO) ₂ MA ^a [mol %]	OEGMA ₄₇₅ ^a [mol %]	functional monomer [mol %]	M _n ^c [10 ³ g mol ⁻¹]	D ^c	functional groups [no./chain]	LCST ^d [°C]
PO ₀ H ₃₀	77.1	0.0	22.9 ^b	16.2	2.41	24	51.0
PO ₁₀ H ₃₀	72.5	5.9	21.6 ^b	17.0	2.08	22	63.0
PO ₁₀₀ H ₃₀	0.00	72.8	27.2 ^b	19.4	2.35	16	>80
PO ₀ A ₃₀	80.6	0.0	19.4 ^a	16.9	2.49	17	40.1
PO ₁₀ A ₃₀	70.4	5.7	23.9 ^a	13.0	2.03	19	53.5
PO ₁₀₀ A ₃₀	0.00	71.9	28.1 ^a	18.3	2.43	16	>80

^aDetermined by ¹H NMR. ^bDetermined from conductometric titration. ^cMeasured using aqueous SEC using an acetate buffer. ^dDetermined at 95% transmittance at a concentration of 1 mg/mL in PBS. Synthesis data reproduced from ref 11.

Introduction.⁶ However, in most cases (and particularly in the case of the *in situ* gelling hydrogels prepared from precursors with different phase transitions described herein), chemical cross-linking is nonideal, and resulting inhomogeneities are observed as static fluctuations.

RESULTS

Synthesis of the Reactive Poly(oligoethylene glycol methacrylate) Precursors. Three sets of PO_xH_y and PO_xA_y precursors were synthesized with varying ratios of M(EO)₂MA and OEGMA₄₇₅ ($x = 0, 10, \text{ and } 100$ mol %, resulting in precursor polymers with various lower critical solution temperatures), similar degrees of hydrazide and aldehyde functionalization ($y = 30$ mol %), and similar number-average molecular weights (M_n). Given that the functional group density and the molecular weight of all polymers generated in this work are similar, each precursor has a similar average number of functional groups per chain (19 ± 3 , Table 2) but differs in terms of lower critical solution temperature (LCST).

Preparation of Poly(oligoethylene glycol methacrylate) Hydrogels. Single precursor POEGMA hydrogels were prepared such that (1) one PO_xH₃₀ and PO_xA₃₀ precursor are used and both precursors are similar in terms of their M(EO)₂MA:OEGMA₄₇₅ composition ($x = 0, 10, \text{ or } 100$ mol %) and (2) the PO_xH₃₀ and PO_xA₃₀ precursors are dissolved at equal concentrations (150 mg/mL in each barrel); by extension, based on the similar functional group densities among all precursors as shown in Table 2, a nearly 1:1 ratio of aldehyde:hydrazide functional groups is present within each hydrogel composition tested. The resulting hydrogels are labeled according to the corresponding mole fraction of OEGMA₄₇₅ used to prepare the precursors (x): PO₀ = PO₀H₃₀ + PO₀A₃₀, PO₁₀ = PO₁₀H₃₀ + PO₁₀A₃₀, and PO₁₀₀ = PO₁₀₀H₃₀ + PO₁₀₀A₃₀ (Table 1). As a result of the difference in OEGMA monomer composition (x), the thermoresponsive properties of the PO₀, PO₁₀, and PO₁₀₀ hydrogels differ substantially; the PO₁₀ hydrogel displayed a volume phase transition temperature (VPTT) at ~ 32 °C, compared to ~ 22 °C for PO₀ and >90 °C for PO₁₀₀.¹¹ The optical appearance of the PO₀, PO₁₀, and PO₁₀₀ hydrogels below and above their VPTT is shown in Figure 1A–F (note that given the high VPTT of the PO₁₀₀ hydrogels, both temperatures tested in Figure 1C,F were below the VPTT of those hydrogels).

The PO₁₀₀ hydrogel remains transparent and swollen upon heating from 22 to 37 °C, as anticipated for high transition temperature hydrogel. The PO₁₀ hydrogel undergoes a volume phase transition at ~ 32 °C, transitioning from transparent below the VPTT (Figure 1B) to translucent above the VPTT (Figure 1E). In contrast, the PO₀ hydrogel appears opaque both below (Figure 1A) and above (Figure 1D) the VPTT,

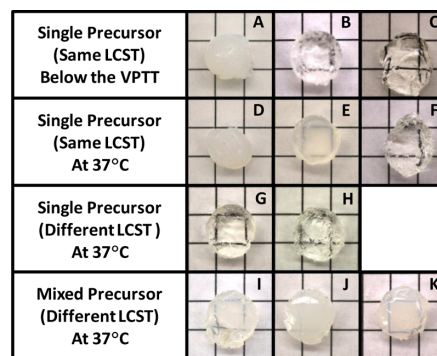


Figure 1. Optical appearance of the various POEGMA hydrogels prepared for the SANS study. Images of the single precursor PO₀ (A), PO₁₀ (B), and PO₁₀₀ (C) hydrogels below their VPTT (5 °C for PO₀ and 22 °C for PO₁₀ and PO₁₀₀). All other images were recorded at 37 °C: PO₀ (D), PO₁₀ (E), PO₁₀₀ (F), PO₁₀₀H₃₀ + PO₁₀A₃₀ (G), PO₁₀H₃₀ + PO₁₀₀A₃₀ (H), PO(25/75) (I), PO(50/50) (J), and PO(75/25) (K). All precursor solutions were filtered with a 0.45 μm PFTE filter to remove dust and other impurities that might otherwise impart the optical transparency of the resulting hydrogel.

suggesting that the opaque appearance of the PO₀ hydrogels is not solely a result of the phase transition behavior of the hydrogel (i.e., formation of internal inhomogeneities on the length scale of visible light is likely). Despite the similarity in the theoretical cross-link density ($y = 30$ mol %) between the different gels, significant differences in the macroscopic gelation time as well as the mechanical properties exist between the PO₀, PO₁₀, and PO₁₀₀ hydrogels.¹¹ The macroscopic gelation time ranges from <5 s for PO₀ to <10 s for PO₁₀ to 1200 s for PO₁₀₀, while the elastic storage modulus (G') and calculated cross-link density (ν) of PO₀ are roughly 1 order of magnitude higher than those of PO₁₀₀.¹¹ We postulated that these property differences may originate from the differing availabilities of the aldehyde and hydrazide functional groups for cross-linking reactions due to steric hindrance by the bulky ethylene oxide ($n = 8-9$) side chains of OEGMA₄₇₅.¹¹

Mixed precursor hydrogels were also produced, exploiting the facile modularity of our approach to injectable hydrogel formation^{13,14} in that multiple precursors with the same functionalization (hydrazide or aldehyde) can be mixed at varying ratios to form a hydrogel that exhibits the combined properties of the precursor mixture following simple coextrusion.^{26,27} Mixed precursor POEGMA hydrogels were prepared by mixing PO₁₀H₃₀, PO₁₀₀H₃₀, PO₁₀A₃₀, and PO₁₀₀A₃₀ precursors such that (1) an equal weight ratio of $x = 10$ and $x = 100$ precursors is added to both the hydrazide and

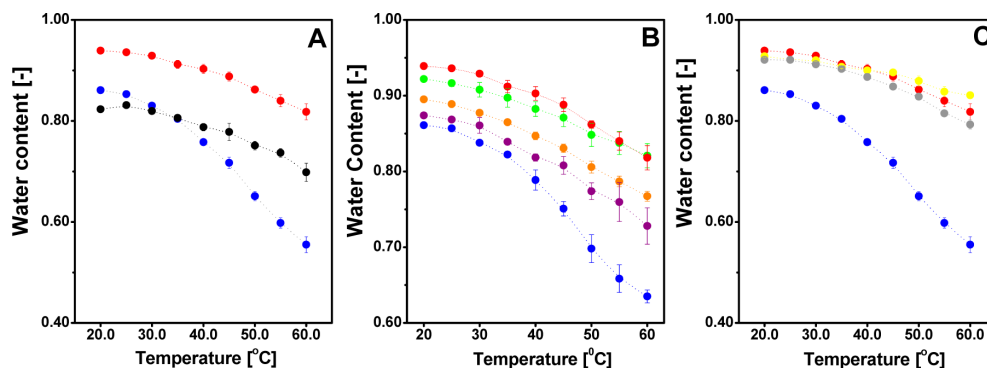


Figure 2. Equilibrium water content of the mixed precursor POEGMA hydrogels as a function of the temperature: PO₀ (black), PO₁₀ = PO(100/0) (blue), PO(75/25) (green), PO(50/50) (orange), PO(25/75) (purple), PO₁₀₀ (red), PO₁₀H₃₀ + PO₁₀₀A₃₀ (yellow), and PO₁₀₀H₃₀ + PO₁₀A₃₀ (gray). Data in (A) reproduced from ref 11.

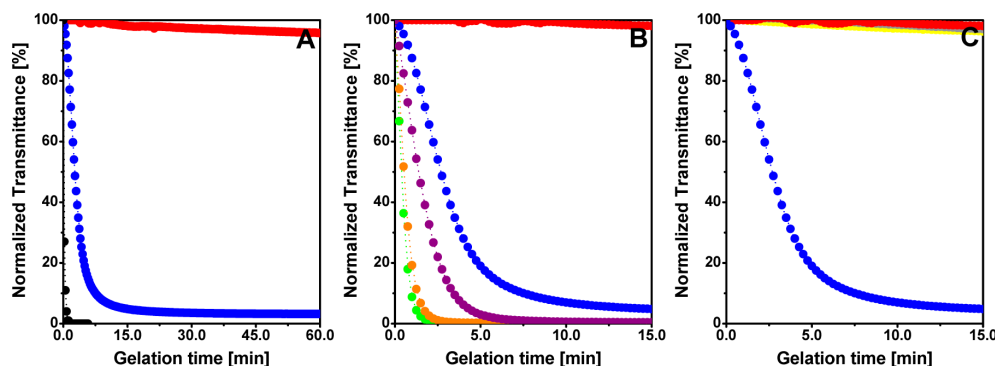


Figure 3. Evolution of the normalized transmittance during gelation of the single precursor (same LCST) (A), single precursor (different LCST) (B), and mixed precursor and (C) POEGMA hydrogels as measured by UV–vis spectrophotometry at 37 °C. PO₀ (black), PO₁₀ = PO(100/0) (blue), PO(75/25) (green), PO(50/50) (orange), PO(25/75) (purple), PO₁₀₀ (red), PO₁₀H₃₀ + PO₁₀₀A₃₀ (yellow), and PO₁₀₀H₃₀ + PO₁₀A₃₀ (gray).

aldehyde barrels of the double-barrel syringe and (2) the aldehyde (PO_xA₃₀) and the complementary hydrazide (PO_xH₃₀) precursor solutions are both prepared at a total concentration of 150 mg/mL, such that (based on the similar functional group densities among all precursors as shown in Table 2) a ~1:1 ratio of aldehyde:hydrazide functional groups is present within each hydrogel composition tested (Table 1). Note that in this case gelation can occur without significant cross-reaction of PO₁₀ and PO₁₀₀ precursors, as both hydrazide and aldehyde-functionalized prepolymers of each LCST are always present. Five hydrogels were prepared by mixing the precursors with $x = 10$ and $x = 100$ mol % in 100/0, 75/25, 50/50, 25/75, and 0/100 weight ratios (for example, the 25/75 wt % hydrogel was prepared by mixing 25% w/w PO₁₀H₃₀ with 75% w/w PO₁₀₀H₃₀ in the hydrazide barrel and 25% w/w PO₁₀A₃₀ and 75% w/w PO₁₀₀A₃₀ in the aldehyde barrel and coextruding the mixture through the mixing channel). The macroscopic gelation time of these hydrogels increases exponentially with increasing PO₁₀₀H₃₀ and PO₁₀₀A₃₀ content of the precursors from <10 s for PO(75/25) to 20 s for PO(50/50) and 230 s for PO(25/75).

Whereas the single-component PO₁₀ and PO₁₀₀ hydrogels are both transparent below the VPTT (Figure 1B,C), the mixed PO(75/25), PO(50/50), and PO(25/75) hydrogels all appear

translucent/opaque (Figure 1I–K). The VPTT of these mixed hydrogels was measured gravimetrically (Figure 2) and resembles that of the PO₁₀₀ hydrogels, as all hydrogels show a gradual decrease in the water content and no discrete volume phase transition as the temperature increases from 20 to 60 °C (although the absolute water content of the hydrogels scales directly with the fraction of the low LCST precursor included in the hydrogel, Figure 2). Even the PO(75/25) hydrogel, which consists of 75% w/w low LCST precursor, exhibits a broad and nondiscrete phase transition temperature, suggesting that introducing even small fractions of high LCST precursors effectively eliminates the discrete VPTT observed for the PO₁₀ hydrogel. The absence of a discrete VPTT up to 60 °C coupled with the observed opacity of the mixed precursor POEGMA hydrogels suggests that these hydrogels are less homogeneous than the corresponding single precursor POEGMA hydrogels.

For comparison, two additional single precursor hydrogels were prepared by coextruding one hydrazide-functionalized and one aldehyde-functionalized POEGMA precursor of different LCST. These hydrogels are prepared such that (1) one PO_xH₃₀ and PO_xA₃₀ precursor respectively are used of different M(EO)₂MA:OEGMA₄₇₅ composition ($x = 10$ or 100 mol %) and (2) the PO_xH₃₀ and PO_xA₃₀ precursors are dissolved at equal concentrations (150 mg/mL in each barrel); as before,

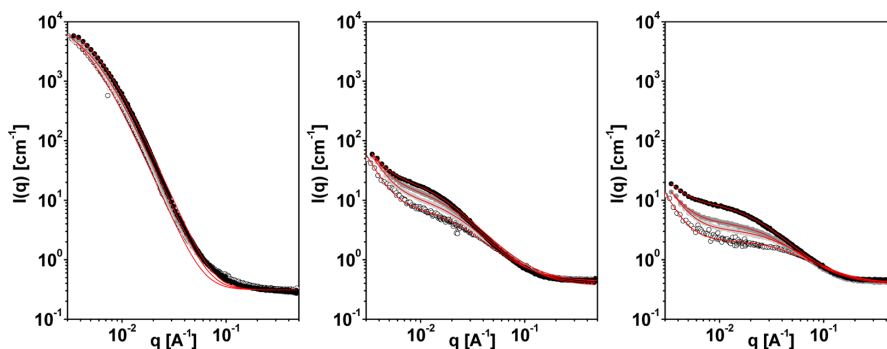


Figure 4. Scattering intensity of the PO₀ (A), PO₁₀ (B), and PO₁₀₀ (C) hydrogels as a function of temperature: (open circle) 22 °C, (light gray circle) 32 °C, (dark gray circle) 37 °C, and (black circle) 45 °C. The Ornstein–Zernike (OZ)–squared Lorentzian (SL) fits of the scattering intensities are shown as the red solid lines.

based on the similar functional group densities among all precursors as shown in Table 2, a reactive functional group ratio of $\sim 1:1$ is achieved. Contrary to the mixed precursor hydrogels that also consist of precursors of different LCSTs, the PO₁₀₀H₃₀ + PO₁₀A₃₀ (Figure 1G) and PO₁₀H₃₀ + PO₁₀₀A₃₀ (Figure 1H) hydrogels are transparent. Gelation of these hydrogels occurs after 20 s for PO₁₀H₃₀ + PO₁₀₀A₃₀ and 230 s for PO₁₀₀H₃₀ + PO₁₀A₃₀, a similar time scale range to the mixed precursor hydrogels that were opaque. Based on these observations, if gelation is forced between precursors with different LCSTs (single precursor/different LCST hydrogels), the resulting gels are transparent; if gelation can still occur without cross-reaction of precursors with different LCSTs (mixed precursor hydrogels), the hydrogels are translucent or opaque.

Kinetics of Structure Development. The optical transmittance during gelation of the single and mixed precursor POEGMA hydrogels was measured by coextruding the reactive precursors (at 22 °C) directly into a UV–vis cuvette incubated at 37 °C (Figure 3A–C and Supporting Information Figure S1).

Although the LCSTs of both PO₀ precursors are >37 °C (PO₀H₃₀ = 51.0 °C and PO₀A₃₀ = 40.1 °C, Table 2), PO₀ gels within seconds and, upon cross-linking, the VPTT quickly drops below 37 °C and the PO₀ hydrogel adopts a milky white appearance with 0% transmittance (Figure 3A). In comparison, the normalized transmittance of the PO₁₀ hydrogel decreases more slowly after coextrusion into the UV cuvette, reaching nearly 0% only after ~ 15 min (Figure 3A). Interestingly, while opacity changes are observed over several minutes, macroscopic gelation occurs much more quickly (<10 s); this result suggests that the observed decrease in transmittance has to be primarily accounted to a volume phase transition that occurs as the cold hydrogel formed quickly after extrusion (22 °C) is heated to 37 °C in the cuvette; this is analogous to the opacity change observed for the PO₁₀ hydrogel in Figure 1B,E upon heating. However, the evolution of inhomogeneities at higher cross-link densities cannot be dismissed as a possible mechanism for this higher opacity. The PO₁₀₀ hydrogel shows virtually no change in normalized transmittance up to 1 h postextrusion (i.e., past the point that bulk gelation has occurred), since the VPTT of the hydrogel at any degree of cross-linking achieved remains well above 37 °C.

Comparable to the PO₁₀ hydrogel, the mixed precursor PO(75/25), PO(50/50), and PO(25/75) hydrogels show a

decrease in the normalized transmittance over the initial 10 min of the experiment (Figure 3B). However, the evolution of transmittance changes faster for the mixed precursor hydrogels than for either constituent single precursor hydrogel; in particular, the PO(75/25) and PO(50/50) hydrogels turn completely opaque within 1 min, on a time scale similar to macroscopic gelation of these samples, while single component gels fabricated from PO₁₀ or PO₁₀₀ precursors took much longer to turn opaque (~ 15 min for PO₁₀) or did not turn opaque whatsoever (PO₁₀₀). This result seems to suggest that opaque appearance of the mixed precursor hydrogels is not caused by a phase change (Figure 3) but rather is a consequence of phase separation during the time scale of gelation. In comparison, single precursor hydrogels prepared by coextruding one PO₁₀ precursor and one PO₁₀₀ precursor (i.e., PO₁₀H₃₀ + PO₁₀₀A₃₀ and PO₁₀₀H₃₀ + PO₁₀A₃₀) were both highly transparent (Figure 1G,H) and demonstrated no significant measured decrease in the normalized transmittance over time (Figure 3C), consistent with the physical appearance of the hydrogels in Figure 1.

SANS of Single Precursor POEGMA Hydrogels. The neutron scattering intensity, $I(q)$, as a function of the scattering vector (q) was measured for PO₀, PO₁₀, and PO₁₀₀ at four different temperatures navigated around the VPTT of the PO₁₀ hydrogel (Figure 4A–C). The neutron scattering intensity curve for PO₀ shows a single-exponential decay, whereas the neutron scattering intensity curves of PO₁₀ and PO₁₀₀ show two decays. Furthermore, the $I(q)$ of the PO₀ hydrogel at low q (i.e., $q < 10^{-2}$ Å⁻¹) is roughly 2 orders of magnitude higher than the $I(q)$ s of the PO₁₀ and PO₁₀₀ hydrogels. These observations suggest that the PO₁₀ and the PO₁₀₀ hydrogels are more homogeneous than the PO₀ hydrogel on the length scale investigated here (roughly 1–200 nm). It should also be noted that the cross-link density of PO₀ was observed to be approximately 1 order of magnitude higher than that of PO₁₀₀,¹¹ which would also contribute to the higher scattering intensity observed for PO₀ even in the absence of heterogeneities. The scattering intensity curves were successfully fitted using eq 1, with generally good fits obtained ($R^2 > 0.99$). The fit parameters describing the network characteristics (ξ and Ξ) are plotted as a function of the temperature in Figure 5A,B.

The neutron scattering intensity curves obtained for PO₀ show a single-exponential decay (Figure 4A) and could be successfully described only accounting for the contribution of

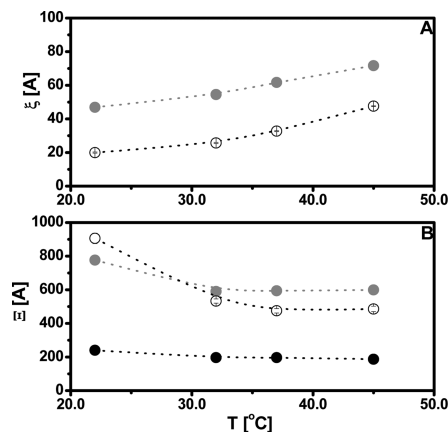


Figure 5. Correlation length of the hydrogel network ξ (A) and the characteristic size of inhomogeneities Ξ (B) for the single precursor PO_0 (black circle), PO_{10} (gray circle), and PO_{100} (open circle) hydrogels as a function of the measurement temperature from mathematical fits of the neutron scattering intensity curves using eq 1. Note: the correlation length for PO_0 hydrogel could not be determined due to the heterogeneity of the hydrogel (i.e., no fluid contribution was relevant).

the static fluctuations (Supporting Information Figure S2). Upon coextrusion the PO_0H_{30} and PO_0A_{30} precursors, macrogelation occurs virtually instantaneously and a heterogeneous hydrogel network is formed. We hypothesize this heterogeneity is derived from the incomplete mechanical mixing provided by the static mixer of the double barrel syringe, as gelation happens too fast and at too great an extent (owing to the highest cross-link density measured for this gel) for diffusional mixing to significantly change the mass distribution of the reactive polymers within the hydrogel phase. Existing concentration fluctuations (e.g., due to chain entanglement in solution) are frozen into the hydrogel network structure, as chain mobility is restricted by the fast cross-link formation. Consequently, no ordered hydrogel network is constructed, and no defined mesh size can be determined for this hydrogel. Rather, the SANS experiments suggest that this

hydrogel network consists of a densely cross-linked chaotic network of static inhomogeneities. The scattering intensity curves show no dependence on the measurement temperature (Figure 4A), and consequently, no temperature dependence of Ξ was observed (Figure 5B). This is consistent with the nearly constant water content measured as a function of the temperature in the gravimetric swelling experiments shown in Figure 2A. As the VPTT of the PO_0 hydrogel is approximately 22 °C, it can be expected that the hydrogel is in a dehydrated and collapsed state even at the lowest measurement temperature of 22 °C.

The PO_{10} and PO_{100} hydrogels (Figure 4B,C) are more homogeneous, and the $I(q)$ curves were successfully described only by considering a summation of dynamic and static fluctuations (Supporting Information Figures S3 and S4). The difference in network homogeneity between the PO_{10} and the PO_0 hydrogel is striking considering that macroscopic gelation of the $\text{PO}_{10}\text{H}_{30}$ and $\text{PO}_{10}\text{A}_{30}$ precursors (<5 s) occurs only marginally slower than for the PO_0H_{30} and PO_0A_{30} precursors. The somewhat slower gelation kinetics and lower ultimate cross-link density achieved for PO_{10} relative to PO_0 (~3-fold lower cross-link density based on mechanics calculations)¹¹ better facilitates spatial reorientation of the polymer chains during cross-linking and consequently locks the precursors in a more homogeneous hydrogel network. Homogeneity is also promoted by the lack of an ongoing phase transition as a function of cross-linking (i.e., the hydrogel phase transition temperature still lies above room temperature even after cross-link formation).

Slowing the gelation kinetics even more (macrogelation for the $\text{PO}_{100}\text{H}_{30}$ and $\text{PO}_{100}\text{A}_{30}$ precursors occurs in approximately 1200 s) reduces $I(q)$ to a lesser extent but does result in a significantly more homogeneous hydrogel network. Furthermore, parallel to the gelation kinetics, the cross-link density also decreases¹¹ which also attributes to lower scattering and the production of a more homogeneous hydrogel.^{28,29} In addition, for both PO_{10} and PO_{100} , unlike for PO_0 , temperature has a clear impact on the hydrogel mesh size (ξ) (positive correlation) and the size of inhomogeneities (Ξ) (negative correlation) observed (Figure 5A,B).

SANS of Mixed Precursor POEGMA Hydrogels. The neutron scattering intensity of the mixed precursor $\text{PO}(75/25)$,

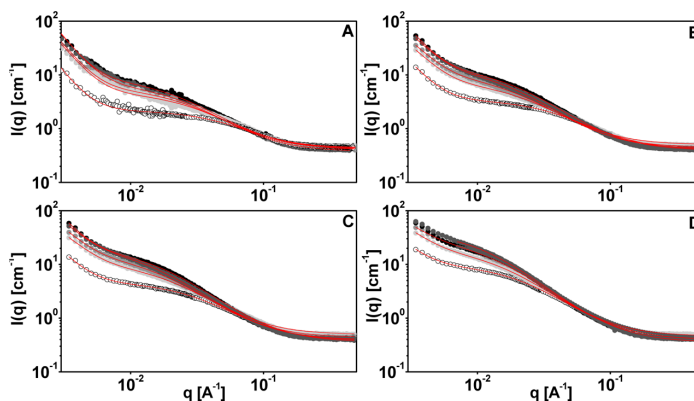


Figure 6. Scattering intensity of the mixed POEGMA hydrogels as 22 (A), 32 (B), 37 (C), and 45 °C (D) as a function of hydrogel composition: (open circle) $\text{PO}(0/100)$ (= PO_{100}), (light gray circle) $\text{PO}(25/75)$, (gray circle) $\text{PO}(50/50)$, (dark gray circle) $\text{PO}(75/25)$, and (black circle) $\text{PO}(100/0)$ (= PO_{10}). The Ornstein-Zernike (OZ)-squared Lorentzian (SL) fits of the scattering intensities are shown as the red solid lines.

PO(50/50), and PO(25/75) hydrogels was measured for each hydrogel at four different temperatures navigated around the VPTT of the PO(100/0) (= PO₁₀) hydrogel and compared to the single component PO(100/0) (= PO₁₀) and PO(0/100) (= PO₁₀₀) hydrogels (Figure 6A–D). Independent of the measurement temperature, the scattering intensity at low q ($<10^{-1}$ Å) increases with increasing weight fraction of the PO₁₀ precursors. There is only a marginal increase in the scattering intensity as the measurement temperature is increased from 22 to 45 °C for all the mixed precursor hydrogels tested (Figure 6). This suggest that none of these heterogeneous precursor hydrogels undergo a bulk phase transition up to 45 °C, in line with the SANS measurements shown in Figure 4B,C for the PO₁₀ and PO₁₀₀ hydrogels and the volumetric deswelling data shown in Figure 2. The scattering intensity curves of all the mixed precursor hydrogels were successfully fitted with eq 1 (Supporting Information Figures S5–S9), with the best-fit parameters describing the network characteristics (ξ and Ξ) plotted as a function of temperature in Figure 7A,B.

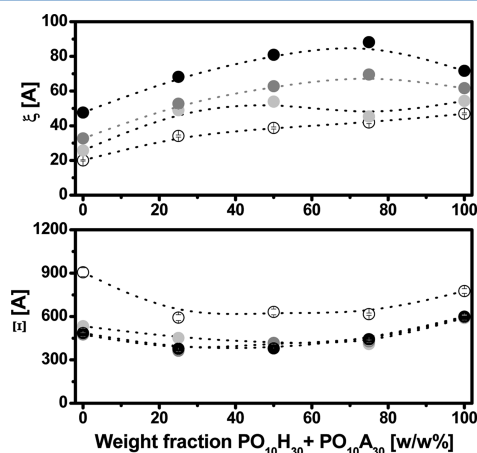


Figure 7. Correlation length (ξ) and the characteristic size of inhomogeneities (Ξ) as a function of the hydrogel composition at 22 °C (open circle), 32 °C (light gray circle), 37 °C (gray circle), and 45 °C (black circle).

From the results in Figure 6, it can be concluded that there is a clear effect of the measurement temperature on the nanostructure of the hydrogel. Similar to the PO₁₀ and PO₁₀₀ hydrogels, the increased measurement temperature increases the fluidity of the network (i.e., the ability of the network to self-diffuse), which results in an increase in ξ and a decrease in Ξ (Figure 7A,B). Despite the slower gelation kinetics and more homogeneous hydrogel network (concluded from the $I(q)$ results in Figure 4C) of PO₁₀₀, the mesh size of the PO₁₀₀ hydrogel is smaller than that of the PO₁₀ hydrogel. Furthermore, the results in Figure 7 show that the composition of the mixed precursor polymers used to prepare the hydrogel has a significant effect on the nanostructure of the hydrogel; as the temperature increases from 22 to 45 °C, the ξ of the mixed PO(75/25), PO(50/50), and PO(25/75) hydrogel networks show larger values for ξ and smaller values for Ξ relative to what would be predicted based on a simple linear combination of PO₁₀ and PO₁₀₀ single precursor gel results. This result suggests that these mixed precursor hydrogels have higher

heterogeneity than the single precursor hydrogels. In addition, given that the hydrogel indicators for heterogeneity deviate more significantly from the linear arithmetic average of the parameters for the two single precursor hydrogels as the temperature is increased, phase separation between the PO₁₀ precursors and the PO₁₀₀ precursors is likely to have occurred within the mixed precursor hydrogels, with the relative scattering intensities of these two domains changing differently as a function of temperature due to the different LCSTs of the polymer precursors.

SANS of Single Precursor POEGMA Hydrogels with Different LCSTs. The neutron scattering intensity, $I(q)$, as a function of the scattering vector (q) was also measured for the PO₁₀H₃₀ + PO₁₀₀A₃₀ and PO₁₀₀H₃₀ + PO₁₀A₃₀ hydrogels at 22 °C to compare the internal morphologies of these single precursor, different LCST gels relative to the single precursor, same LCST hydrogels which were also transparent (Figure 8 and Supporting Information Figure S9).

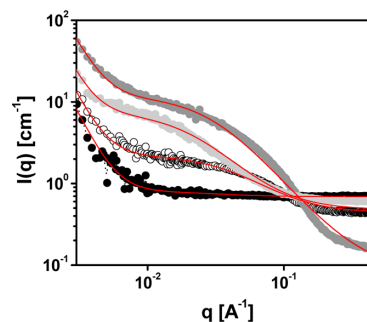


Figure 8. Scattering intensity at 22 °C of the single precursor hydrogels based on precursors with similar LCSTs (open circle) PO₁₀₀H₃₀ + PO₁₀₀A₃₀ and (light gray circle) PO₁₀H₃₀ + PO₁₀A₃₀ and precursors with different LCSTs (black circle) PO₁₀H₃₀ + PO₁₀₀A₃₀ and (gray circle) PO₁₀₀H₃₀ + PO₁₀A₃₀. The Ornstein–Zernike (OZ)–squared Lorentzian (SL) fits of the scattering intensities are shown as the red solid lines.

Compared to the neutron scattering intensity of the PO₁₀ and PO₁₀₀ hydrogels at low q ($q \leq 10^{-2}$ Å) the hydrogel prepared from PO₁₀H₃₀ + PO₁₀₀A₃₀ scatters more (i.e., more inhomogeneous), whereas the hydrogel prepared from PO₁₀₀H₃₀ + PO₁₀A₃₀ scatters less (i.e., more homogeneous) (Figure 8). The difference in gelation kinetics (PO₁₀H₃₀ and PO₁₀₀A₃₀ cross-link in 20 s, whereas PO₁₀₀H₃₀ and PO₁₀A₃₀ cross-link in 230 s), coupled with the SANS results in Figure 8, could suggest that the presence of the PO₁₀H₃₀ precursor results in fast gelation and consequently more heterogeneous hydrogels. Given that these hydrogels remain transparent, the SANS result implies that while the different LCSTs of the precursors drives a phase separation upon gelation, the magnitude of that phase separation is limited by the covalent cross-link formation occurring between the two precursors on the time scale of phase separation; as such, the size of domains formed is likely limited due to network stiffness and the hydrogels remain transparent. Interestingly, recent work by Saffer and co-workers^{30,31} have shown similar results for thionorborene cross-linked PEG hydrogels prepared with short PEG chain lengths (4K and 8K g mol⁻¹), in which the short PEG chain length could not sufficiently counteract the hydrophobic effect of the norbornene end groups and

heterogeneous hydrogels were produced. While we cannot definitively rule this phenomenon out as a possible explanation for the hydrogel opacities observed, the fact that hydrogels prepared with the exact same total OEGMA monomer balance (i.e., same overall end-group composition and same overall hydrophilic/hydrophobic balance) can be made transparent (if only 2 precursors of different LCSTs are used) or highly opaque (if 4 precursors, 2 of each LCST value, are used) suggests to us that microphase separation is the more likely explanation. The absence of any sort of highly hydrophobic entity such as the norbornene group in our hydrogels further supports our hypothesis.

Light Scattering of Single and Mixed Precursor POEGMA Hydrogels. One homogeneous precursor (PO₁₀₀, transparent, Figure 1D) and one heterogeneous precursor (PO(50/50), opaque, Figure 1H) POEGMA hydrogel were characterized by light scattering (LS). The intensity profile was plotted with respect to the scattering vector q following Bragg's law (eq 4)

$$q = \frac{4\pi \sin\left(\frac{2\theta}{2}\right)}{\lambda} \quad (4)$$

where the real space distance is calculated by $d = 2\pi/q$. The intensity profiles (corrected for the scattering from the cuvette) for PO₁₀₀ and PO(50/50) are shown in Figure 9. The signal was fitted using Gaussian distributions. Structural peaks at $d = 2.9 \mu\text{m}$ ($Q = \pm 2.19 \times 10^{-4} \text{ \AA}^{-1}$) were observed in the optically transparent PO₁₀₀ hydrogel together with a central peak indicative of longer length scales which cannot be resolved by the light scattering technique. For the opaque PO(50/50)

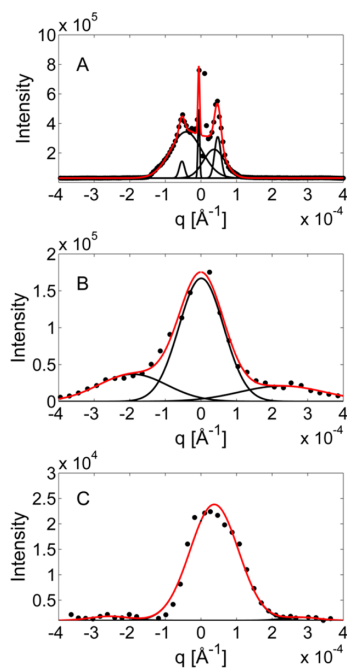


Figure 9. Light scattering intensity as measured for (A) the cuvette (= background), (B) the single precursor POEGMA hydrogel PO₁₀₀, and (C) the mixed precursor POEGMA hydrogel PO(50/50).

hydrogel, a similar length scale of structural peak at $d = 2.2 \mu\text{m}$ ($Q = \pm 2.84 \times 10^{-4} \text{ \AA}^{-1}$) was observed but at significantly lower intensity than those observed for PO₁₀₀. As such, scattering in PO(50/50) was mainly due to the central peak (i.e., due to larger features that cannot be resolved by LS). From the half-width at half-maximum of the central peak of $7.02 \times 10^{-5} \text{ \AA}^{-1}$, a lower bound for the size of the observed structures in the opaque PO(50/50) hydrogel can be estimated to be approximately $8 \mu\text{m}$, although structures significantly larger are also likely to also be present. No additional peaks were observed at higher scattering angles, which excludes the possibility of the presence of structures of smaller length scales (i.e., $>1 \mu\text{m}$). The data thus suggest that the scattering length scales in the opaque hydrogel samples are significantly longer than the transparent hydrogel sample.

DISCUSSION

The scattering intensity functions of the PO₁₀ and PO₁₀₀ single precursor hydrogels shown in Figure 4A,B can be represented by a summation of dynamic (OZ) and static (SL) fluctuations, typically used for the characterization of hydrogel systems;^{7,24} in contrast, the scattering intensity function of the PO₀ hydrogel could be fully fit by considering static (SL) fluctuations only. Consequently, it can be concluded that the PO₁₀ and the PO₁₀₀ hydrogels are more homogeneous and contain less "frozen" domains than the PO₀ hydrogel. This result is consistent with the observed opacity, the faster rate of gelation (limiting the potential degree of diffusional mixing of the two reactive precursor polymers), and the significantly lower phase transition temperature (facilitating temperature-induced phase separation into domains) of PO₀ relative to the other hydrogels assessed. In contrast, slower gelation kinetics and lower cross-link densities result in more homogeneous hydrogels that show a mesh size of 2–7 nm (depending on temperature) with inhomogeneities on a size range of 40–60 nm (i.e., inhomogeneities are present, but on a length scale that the optical transparency of the hydrogels is not affected) for the transparent PO₁₀ and the PO₁₀₀ hydrogels.

For the PO₁₀ and PO₁₀₀ hydrogels, temperature has a clear impact on the hydrogel mesh size (ξ) and the size of inhomogeneities (Ξ) observed within those hydrogel networks (Figure 5A,B). For both hydrogels, the mesh size increases with increasing temperature. Although this result is counterintuitive when compared to the macroscopic behavior of thermoresponsive hydrogels when heated to a temperature (T) close to the critical phase transition temperature (T_c) (i.e., hydrogel deswelling would be expected to reduce the mesh size), an increase in ξ has been similarly observed for thermoresponsive poly(*N*-isopropylacrylamide) (PNIPAAm) and dimethylacrylamide (DMAAm) hydrogels.^{23,24} The increase in ξ seems to diverge asymptotically as $T - T_c$ approaches 0, which has also been shown by Shibayama for conventional free radical-polymerized PNIPAAm hydrogels (and in fact holds true for any phase transition in materials).^{23,24} As the temperature increases, the fluidity (i.e., self-diffusion) of the polymer chains in the network increases, leading to increased dynamic fluctuations and consequently a larger ξ . As the network collapses at T_c , this fluidity is lost, and the hydrogel network can be described by static fluctuations only (as was observed experimentally for the PO₀ hydrogel, Figure 4A). It was expected based on the measured macroscopic phase transition of PO₁₀ that ξ would diverge (i.e., approach infinity) around the VPTT of 32–33 °C; however, this was not observed

experimentally. Furthermore, the relatively small but still significant decrease in Ξ as observed here for the PO₁₀ and PO₁₀₀ hydrogels is generally not observed for conventional thermoresponsive PNIPAAm hydrogels, for which Ξ remained relatively constant over the whole temperature range probed. We hypothesize that this difference is related not to the different gelation mechanisms but rather to the fundamental chemical differences between PNIPAAm and POEGMA. The phase transition in PNIPAAm polymers is characterized by a transition from hydrogen bonding with water at $T < \text{LCST}$ to intramolecular hydrogen bonding between the amide nitrogen and the amide carbonyl group at $T > \text{LCST}$.³² As POEGMA polymers lack a hydrogen bond donor, the phase transition in POEGMA hydrogels is instead characterized by continuous dehydration followed by chain aggregation. On this basis, we expect that the observed decrease in Ξ (related to the size of the inhomogeneous domains) is related to a collapse of these domains (40–60 nm in size) due to continuous dehydration at higher temperatures.

Contrary to the single precursor hydrogels, the mixed precursor hydrogels all appear translucent (Figure 1). The gelation experiments (Figure 3B) showed that this translucency did not originate from a volume phase transition but rather was induced during macroscopic gelation of the precursors (indeed, at times well before macroscopic gelation was observed). This suggests that opacity of the mixed PO(75/25), PO(50/50), and PO(25/75) hydrogels is due to the presence of larger inhomogeneities in the hydrogel network. SANS scattering intensity functions of these mixed precursor hydrogels could be successfully described by a combination of dynamic (OZ) and static (SL) fluctuations. As the hydrogel composition shifts from exclusively PO₁₀₀ precursors to exclusively PO₁₀ precursor, it can be expected that the cross-link density increases, which increases scattering (as observed). Similar results were obtained for PNIPAAm hydrogels cross-linked with *N,N*-methylenebis(acrylamide) (MBAAm), in which $I(q)$ increased with increasing mole fraction of MBAAm.³³ A difference in the network structure was also observed, as the mixed precursor hydrogels generally show larger mesh sizes and (surprisingly, given the opacity) smaller inhomogeneities than the single precursor hydrogels (Figure 7A,B). We anticipate that the larger domains that led to hydrogel opacity were at a larger length scale than could be probed by SANS (i.e., inhomogeneities occur at multiple length scales in these hydrogels). Consequently, complementary LS experiments were performed on one transparent single precursor hydrogel (PO₁₀₀) and one mixed precursor hydrogel (PO(50/50), the hydrogel with the fastest development of opacity upon gelation). The scattering intensity functions showed a clear shift from structures predominantly around 2.9 μm for the PO₁₀₀ hydrogel to structures that are significantly larger (>8 μm) for the PO(50/50) hydrogel (Figure 9). These results strongly suggest that the mixed precursor hydrogels contain significant concentrations of very large domains that cause scattering and thus impart an opaque appearance of these hydrogels.

From an application point of view, the knowledge gained through this study regarding the internal morphology of injectable POEGMA hydrogels provides significant insight into the design of such hydrogels for targeted applications. For example, hydrogels designed for ophthalmic applications (i.e., vitreous humor substitutes or prolonged drug delivery vehicles to the back of the eye) must be designed to strike a balance

between the cross-link density (which determines G' and, in our case, the degradation rate¹²) and the optical transparency. High cross-link densities can be achieved (using PO₀ precursors), but at the expense of optical clarity of the hydrogel. Conversely, highly transparent PO₁₀₀ hydrogels can be prepared, but the mechanical strength and degradation stability of those hydrogels are inherently limited. On the basis of the transparency of the hydrogel produced by mixing a one PO₁₀ precursor with one PO₁₀₀ precursor (one functionalized with hydrazides and the other with aldehydes, Figure 1), we anticipate that improved mechanics/degradation lifetimes while preserving transparency may be achievable by mixing precursors with different LCSTs. The difference in the network structure between the single and mixed precursor hydrogels also provides an interesting opportunity in terms of understanding and optimizing injectable POEGMA hydrogels for controlled release applications, given that drug release kinetics are directly governed by the internal morphology hydrogel network. A full evaluation of the macroscopic (physiochemical, biological, and drug release) properties of these mixed precursor POEGMA hydrogels in the context of biomedical applications will be discussed in a follow-up study.

■ CONCLUSIONS

Small-angle neutron scattering and light scattering have been applied to probe the internal morphology of injectable *in situ* gelling hydrogels based on hydrazide and aldehyde-functionalized POEGMA precursor polymers with varying lower critical solution temperatures. Transparent hydrogels are formed if two precursor polymers with similar or dissimilar LCST values were mixed, provided the LCST is not too low or the cross-linking potential of the precursors is not too high, although the internal homogeneity of the hydrogels prepared with different LCST precursors is significantly higher; in contrast, highly opaque hydrogels with very large inhomogeneous domains are formed if pairs of precursors with different LCST values are coextruded (i.e., in cases in which gelation can proceed even if phase separation occurs). Thus, by tuning the number and LCST values of polymer precursors used to prepare the injectable hydrogel, gel morphologies can be tuned over a broad range. This insight offers significant potential to rationally design POEGMA-based *in situ* gelling hydrogels for targeted biomedical applications, particularly in the context of controlled release of therapeutics with specific affinities to the inhomogeneous phase.

■ ASSOCIATED CONTENT

Supporting Information

UV–vis gelation experiments and curve-fitted data for all measured SANS profiles. This material is available free of charge via the Internet at <http://pubs.acs.org>.

■ AUTHOR INFORMATION

Corresponding Author

*E-mail hoaretr@mcmaster.ca (T.H.).

Notes

The authors declare no competing financial interest.

■ ACKNOWLEDGMENTS

Funding from 20/20: NSERC Ophthalmic Materials Research Network, the Ontario Ministry of Research and Innovation Postdoctoral Fellowship program (N.M.B.S.), and NSERC

CREATE-IDEM (Integrated Design of Extracellular Matrices) (E.B.) is gratefully acknowledged. This research was also funded by the Natural Sciences and Engineering Research Council of Canada (NSERC), the National Research Council Canada (NRC), the Canada Foundation for Innovation (CFI), and the Ontario Ministry of Economic Development and Innovation. M.C.R. is the recipient of an Early Researcher Award of the Province of Ontario. This work utilized facilities supported in part by the National Science Foundation under Agreement DMR-0944772. We acknowledge the support of Dr. Boualem Hammouda and the National Institute of Standards and Technology, U.S. Department of Commerce, in providing the neutron research facilities used in this work.

■ REFERENCES

- (1) Langer, R.; Tirrell, D. A. *Nature* **2004**, *428*, 487–492.
- (2) Slaughter, B. V.; Khurshid, S. S.; Fisher, O. Z.; Khademhosseini, A.; Peppas, N. A. *Adv. Mater.* **2009**, *21*, 3307–3329.
- (3) Hoare, T.; Kohane, D. S. *Polymer* **2008**, *49*, 1993–2007.
- (4) Hoffman, A. S. *Adv. Drug Delivery Rev.* **2002**, *54*, 3–12.
- (5) Tibbitt, M. W.; Anseth, K. S. *Biotechnol. Bioeng.* **2009**, *103*, 655–663.
- (6) Matsunaga, T.; Sakai, T.; Akagi, Y.; Chung, U.; Shibayama, M. *Macromolecules* **2009**, *42*, 1344–1351.
- (7) Shibayama, M. *Macromol. Chem. Phys.* **1998**, *199*, 1–30.
- (8) Metters, A. T.; Anseth, K. S.; Bowman, C. N. *J. Phys. Chem. B* **2001**, *105*, 8069–8076.
- (9) Malkoch, M.; Vestberg, R.; Gupta, N.; Mespouille, L.; Dubois, P.; Mason, A. F.; Hedrick, J. L.; Liao, Q.; Frank, C. W.; Kingsbury, K.; Hawker, C. J. *Chem. Commun.* **2006**, 2774–2776.
- (10) Patenaude, M.; Smeets, N. M. B.; Hoare, T. *Macromol. Rapid Commun.* **2014**, *35*, 598–617.
- (11) Smeets, N. M. B.; Bakaic, E.; Patenaude, M.; Hoare, T. *2014*.
- (12) Smeets, N. M. B.; Bakaic, E.; Patenaude, M.; Hoare, T. *Chem. Commun.* **2014**, *50*, 3306–3309.
- (13) Patenaude, M.; Hoare, T. *ACS Macro Lett.* **2012**, *1*, 409–413.
- (14) Patenaude, M.; Hoare, T. *Biomacromolecules* **2012**, *13*, 369–378.
- (15) Ito, T.; Yeo, Y.; Highley, C. B.; Bellas, E.; Kohane, D. S. *Biomaterials* **2007**, *28*, 3418–3426.
- (16) Alves, M.; Young, C. *Biomed. Mater.* **2012**, *7*, 024106.
- (17) Ossipov, D. A.; Hilborn, J. *Macromolecules* **2006**, *39*, 1709–1718.
- (18) Oommen, O. P.; Wang, S.; Kisiel, M.; Sloff, M.; Hilborn, J.; Varghese, O. P. *Adv. Funct. Mater.* **2013**, *23*, 1273–1280.
- (19) Hudson, S. P.; Langer, R.; Fink, G. R.; Kohane, D. S. *Biomaterials* **2010**, *31*, 1444–1452.
- (20) Lee, K. Y.; Bouhadir, K. H.; Mooney, D. J. *Macromolecules* **2000**, *33*, 97–101.
- (21) Lutz, J.-F. *J. Polym. Sci., Part A: Polym. Chem.* **2008**, *46*, 3459–3470.
- (22) Lutz, J.-F.; Weichenhan, K.; Akdemir, Ö.; Hoth, A. *Macromolecules* **2007**, *40*, 2503–2508.
- (23) Shibayama, M.; Morimoto, M.; Nomura, S. *Macromolecules* **1994**, *27*, 5060–5066.
- (24) Shibayama, M.; Isono, K.; Okabe, S.; Karino, T.; Nagao, M. *Macromolecules* **2004**, *37*, 2909–2918.
- (25) Ornstein, L. S.; Zernicke, F. *Proc. Acad. Sci. Amsterdam* **1914**, *17*, 793–806.
- (26) Sivakumaran, D.; Maitland, D.; Hoare, T. *Biomacromolecules* **2011**, *12*, 4112–4120.
- (27) Campbell, S. B.; Patenaude, M.; Hoare, T. *Biomacromolecules* **2013**, *14*, 644–653.
- (28) Mallam, S.; Horkay, F.; Hecht, A. M.; Geissler, E. *Macromolecules* **1989**, *22*, 3356–3361.
- (29) Shibayama, M.; Norisuye, T.; Nomura, S. *Macromolecules* **1996**, *29*, 8746–8750.
- (30) Saffer, E. M.; Lackey, M. A.; Griffin, D. M.; Kishore, S.; Tew, G. N.; Bhatia, S. R. *Soft Matter* **2014**, *10*, 1905–1916.
- (31) Cui, J.; Lackey, M. A.; Madkour, A. E.; Saffer, E. M.; Griffin, D. M.; Bhatia, S. R.; Crosby, A. J.; Tew, G. N. *Biomacromolecules* **2012**, *13*, 584–588.
- (32) Sun, S.; Wu, P. *Macromolecules* **2013**, *46*, 236–246.
- (33) Takata, S.; Norisuye, T.; Shibayama, M. *Macromolecules* **2002**, *35*, 4779–4784.

Bibliography

- [1] Huiskes R (2000) If bone is the answer, then what is the question? *Journal of Anatomy* 197: 145–156.
- [2] Arzt E (2006) Biological and artificial attachment devices: Lessons for materials scientists from flies and geckos. *Materials Science and Engineering: C* 26: 1245 - 1250.
- [3] Meyers MA, Chen PY, Lin AYM, Seki Y (2008) Biological materials: Structure and mechanical properties. *Progress in Materials Science* 53: 1 - 206.
- [4] Zintzen V, Roberts CD, Anderson MJ, Stewart AL, Struthers CD, et al. (2011) Hagfish predatory behaviour and slime defence mechanism. *Scientific reports* 1: 131.
- [5] Claycomb JR, Tran J (2010) *Introductory biophysics: Perspectives on the living state*. Jones & Bartlett Learning. ISBN: 978-0763779986.
- [6] Champe PC, Harvey RA, Ferrier DR (2005) *Biochemistry*. Lippincott Williams & Wilkins. ISBN: 978-0781722650.
- [7] Berg JM, Tymoczko JL, Stryer L (2006) *Biochemistry*. Freeman and Company: New York. ISBN: 978-0716787242.

- [8] Pauling L, Corey RB, Branson HR (1951) The structure of proteins: two hydrogen-bonded helical configurations of the polypeptide chain. *Proc Natl Acad Sci USA* 37: 205–211.
- [9] Pauling L, Corey RB (1951) The pleated sheet, a new layer configuration of polypeptide chains. *Proc Natl Acad Sci USA* 37: 251–256.
- [10] Jaenicke R (1995) Folding and association versus misfolding and aggregation of proteins. *Philosophical Transactions of the Royal Society of London Series B: Biological Sciences* 348: 97–105.
- [11] Uversky VN, Fink A (2007) Protein Misfolding, Aggregation and Conformational Diseases: Part A: Protein Aggregation and Conformational Diseases, volume 4. Springer. ISBN: 978-0387259192.
- [12] Voet D, Voet JG (2004) *Biochemistry*. John Wiley & Sons. ISBN: 978-0471193500.
- [13] Rho JY, Kuhn-Spearing L, Zioupos P (1998) Mechanical properties and the hierarchical structure of bone. *Medical engineering & physics* 20: 92–102.
- [14] Tombolato L, Novitskaya EE, Chen PY, Sheppard FA, McKittrick J (2010) Microstructure, elastic properties and deformation mechanisms of horn keratin. *Acta biomaterialia* 6: 319–330.
- [15] Raabe D, Sachs C, Romano P (2005) The crustacean exoskeleton as an example of a structurally and mechanically graded biological nanocomposite material. *Acta Materialia* 53: 4281–4292.

- [16] Bhushan B (2007) Adhesion of multi-level hierarchical attachment systems in gecko feet. *Journal of Adhesion Science and Technology* 21: 1213–1258.
- [17] Raabe D, Romano P, Sachs C, Al-Sawalmih A, Brokmeier HG, et al. (2005) Discovery of a honeycomb structure in the twisted plywood patterns of fibrous biological nanocomposite tissue. *Journal of Crystal Growth* 283: 1–7.
- [18] Vincent JF (1982) *Structural biomaterials*. Halsted Press. ISBN: 978-0333261255.
- [19] Förster S, Timmann A, Schellbach C, Frömsdorf A, Kornowski A, et al. (2007) Order causes secondary bragg peaks in soft materials. *Nature materials* 6: 888–893.
- [20] Herzog R, Jancke W (1921) *Festschrift der kaiser-wilhelm-gesellschaft*. Julius Springer, Berlin 120.
- [21] Astbury W, Woods H (1934) X-ray studies of the structure of hair, wool, and related fibres. ii. the molecular structure and elastic properties of hair keratin. *Philosophical Transactions of the Royal Society of London Series A, Containing Papers of a Mathematical or Physical Character* : 333–394.
- [22] Perutz M (1951) New x-ray evidence on the configuration of polypeptide chains: Polypeptide chains in poly-gamma-benzyl-l-glutamate, keratin and hæmoglobin. *Nature* 167: 1053–1054.
- [23] Pauling L, Corey RB (1951) The structure of hair, muscle, and related proteins. *Proc Natl Acad Sci USA* 37: 261–271.

-
- [24] Pauling L, Corey RB (1953) Compound helical configurations of polypeptide chains: structure of proteins of the α -keratin type. *Nature* 171: 59–61.
- [25] Crick FH (1953) The packing of-helices: simple coiled-coils. *Acta crystallographica* 6: 689–697.
- [26] Cochran W, Crick F, Vand V (1952) The structure of synthetic polypeptides. i. the transform of atoms on a helix. *Acta Crystallographica* 5: 581–586.
- [27] Sherwood D (1976) *Crystals, X-rays and Proteins*. Longman, London. ISBN: 978-0582460423.
- [28] Astbury W, Woods H (1930) The x-ray interpretation of the structure and elastic properties of hair keratin. *Nature* 126: 913.